LIÈGE université
Sciences Appliquées

INSTRUMENTED FLEXIBLE GLASS STRUCTURE
Design of Flexure Mechanisms for Resonators and Micro-Scale Monolithic Bragg Grating Sensors

A thesis submitted in partial fulfillment of the requirements
for the degree of Doctor of Philosophy (PhD) in Engineering Science

by

Loïc AMEZ-DROZ

Supervisor: Christophe COLLETTE

Joint PhD thesis supervisor: Pierre LAMBERT

DOCTORAL COLLEGE IN AEROSPACE AND MECHANICS

AUGUST 2024

INSTRUMENTED FLEXIBLE GLASS STRUCTURE

Design of Flexure Mechanisms for Resonators and Micro-Scale Monolithic Bragg Grating Sensors

Thèse disponible à l'adresse https://hdl.handle.net/2268/318479

présentée le 27 Août 2024
à l'Université de Liège

et retransmise en direct pour l'Université libre de Bruxelles et le public à distance

pour l'obtention du grade de Docteur en Sciences de l'Ingénieur et Technologie
par

Loïc Amez-Droz

soumise aux membres du jury:

Prof. Tristan Gilet, président du jury
Prof. Christophe Collette, promoteur ULiège et secrétaire
Prof. Pierre Lambert, promoteur ULB
Prof. Christophe Caucheteur, membre
Prof. Yves Bellouard, membre
Prof. Anne Mertens membre
Prof. Benoit Scheid, membre

Bruxelles, ULiège & ULB, Août 2024

True science teaches, above all,
to doubt and be ignorant.
— Miguel de Unamuno

To my parents, Geneviève & Patrick Amez-Droz

Remerciements

Je souhaite exprimer ma plus profonde gratitude au Professeur Christophe Collette et au Professeur Pierre Lambert, qui m'ont offert l'opportunité de réaliser ce travail au sein des services Aérospatiale & Mécanique de l'Université de Liège et Transferts Interfaces et Procédés de l'Université libre de Bruxelles.

Je tiens également à remercier les Professeurs Christophe Caucheteur, Tristan Gilet, Benoit Scheid et Philippe Venderbemden, membres de mon comité d'accompagnement, pour leurs précieux conseils tout au long de cette aventure. J'adresse aussi mes remerciements aux membres de mon jury pour l'examen attentif de ce travail.

Je suis profondément reconnaissant au Fonds National de la Recherche Scientifique pour le financement du projet de recherche INFuSE, sans lequel ce travail n'aurait pas été possible.

Un grand merci va aux équipes de développement de Grammarly et OpenAI, dont les outils m'ont été d'une aide précieuse pour corriger et améliorer mes textes, me faisant ainsi gagner un temps précieux.

Je remercie également mes collègues pour les moments agréables partagés, en particulier Monsieur Anthony Amorosi du Precision Mechatronics Laboratory, pour sa collaboration sur la conception de capteurs inertiels, ainsi que le Docteur Matéo Tunon de Lara, avec qui j'ai avancé sur le projet INFuSE, et le Docteur Adam Chafaï pour son aide précieuse au sein de la plateforme de fabrication Micro-milli.

Enfin, je souhaite exprimer ma gratitude la plus sincère à mes amis, ma famille, et à toutes les personnes rencontrées au fil de ce travail, qui m'ont soutenu et aidé à faire progresser ce projet.

Bruxelles, 27 Août 2024 L. A.-D.

Abstract

The INFuSE project, funded by an FNRS PDR grant, began in 2020 to develop resonators for inertial sensors and sensor arrays incorporating photonics for force/strain and biochemical sensing. This project harnesses the unique properties of glass along with advanced 3D machining technology. Glass's low loss factor, low thermal expansion rate, optical quality surface finish, and high elastic limit-to-Young's modulus ratio make it ideal for precision mechanics and resonators. The manufacturing of fused silica structures at scales below 1 mm presents challenges. To address these challenges, the project utilizes the FEMTOprint machine, a cutting-edge device that enables 3D machining with sub-micron precision. This technology uses femtosecond laser-assisted wet etching to create monolithic structures that can integrate fluidic, optical, and mechanical functionalities at nano- and micro-scale. This work's contributions include the successful fabrication of various flexible structures using the femtosecond laser-assisted wet etching process, achieving thicknesses as low as 10 μm. The bending strength for fused silica specimens is estimated, with a maximum estimated stress of 2.6 GPa and a recommended limit of 1 GPa for micro-scale flexure specimens conception. Additionally, ring-down experiments on fused silica-based resonators showed that the damping is influenced by the air pressure at 2×10^{-3} mbar, with a quality factor reaching 185,000. The project also saw the development and manufacturing of two different vertical inertial sensors, demonstrating the successful assembly of glass flexure joints with aluminium and stainless steel components. The open-loop transfer function of the first sensor showed good coherence with a reference sensor between 200 mHz and 100 Hz having its natural frequency at 2.8 Hz. Then, the main novelty of the thesis is the realisation of Bragg grating sensors inscribed in flexure specimens. Their sensitivity compares to the theoretical value of approximately 1.2 pm/με. A method for compensating for temperature gradients in Bragg grating sensors was proposed, pending further characterization. These contributions lay a strong foundation for future advancements in resonator technology and instruments with embedded photonics, enhancing applications in force/strain sensing.

Keywords: fused silica, precision manufacturing, compliant mechanisms, resonators, Bragg grating sensors

List of Publications

List of Scientific Production

Journal Papers

M. Tunon de Lara, **L. Amez-Droz**, K. Chah, P. Lambert, C. Collette, C. Caucheteur *Femtosecond pulse laser-engineered glass flexible structures instrumented with an in-built Bragg grating sensor.* Optics Express 31.18 (2023): 29730.

L. Amez-Droz, M. Tunon de Lara, C. Collette, C. Caucheteur, P. Lambert *Instrumented Flexible Glass Structure: A Bragg Grating Inscribed with Femtosecond Laser Used as a Bending Sensor.* Sensors 23.19 (2023): 8018.

M. Tunon de Lara, **L. Amez Droz**, K . Chah, P. Lambert, C. Collette, C. Caucheteur *Optical and spectral characterization methodologies of Bragg gratings engineered in silica planar substrates with femtosecond laser pulses.* Journal Optics & Laser Technology (2024): on review

Conference Proceedings

M. Tunon de Lara, K. Chah, **L. Amez-Droz**, P. Lambert, C. Collette, C. Caucheteur *Production of an Optical Waveguide in Planar Glass Substrate Fabricated with Femtoprint.* SPIE Photonics Europe - Strasbourg April 2022.

A. Amorosi, **L. Amez-Droz**, M. Teloi, M. H. Lakkis, B. Ding, J. Watchi, A. Sider, C. Di Fronzo, R. Jamshidi, P. Lambert, C. Collette *High resolution compact vertical inertial sensor for atomic quantum gravimeter hybridization.* Paper presented at the ISMA-USD Noise and Vibration Engineering Conference 2022.

M. Tunon de Lara Ramos, **L. Amez Droz**, K. Chah, P. Lambert, C. Collette, C. Caucheteur *Synthesis of an optical waveguide in bulk silica with a femtosecond laser inscription and wet etching treatment.* IEEE Photonics Society Benelux Chapter - Eindhoven November 2022.

M. Tunon de Lara, K. Chah, **L. Amez-Droz**, P. Lambert, C. Collette, C. Caucheteur *Bragg grating*

manufacturing in planar silica substrates. SPIE Optics + Electronics, Prague April 2023.

M. Tunon de Lara, K. Chah, **L. Amez-Droz**, P. Lambert, C. Collette, C. Caucheteur *Femtosecond Laser Micro/Nano-Machining of Silica Glass Planar Substrates for the Production of Bragg Gratings.* European Workshop on Optical Fibre Sensors - Mons May 2023.

M. Tunon de Lara, **L. Amez Droz**, K . Chah, P. Lambert, C. Collette, C. Caucheteur *Characterization of optical waveguides engraved in silica planar substrates with a femtosecond laser process.* IEEE Photonics Society Benelux Chapter - Gand November 2023.

M. Tunon de Lara, **L.Amez-Droz**, Amorosi, A., P.Lambert, C.Caucheteur, C.Collette *Fabrication of Bragg Gratings in Flat Silica Substrates Using the Femtoprint Device and Use for Sensing.* SPIE Photonic Europe - Strasbourg April 2024.

L.Amez-Droz, M. Tunon de Lara, A. Amorosi, P.Lambert, C.Collette, C.Caucheteur *Investigating Fused Silica Bending Strength and Damping Characteristics on Resonators Fabricated through Femtosecond Laser-Assisted Wet Etching: An Experimental Analysis* International Conference on Manipulation, Automation and Robotics at Small Scales - Delft July 2024.

Conference Presentation

Oral presentation

L.Amez-Droz, M. Tunon de Lara, C.Collette, C.Caucheteur, P.Lambert *A Monolithic Glass micro-Scale Structure Including a Bragg Grating Sensor Inscribed with a Femtosecond Laser* International Conference on Manipulation, Automation and Robotics at Small Scales - Abu Dhabi October 2023.

L.Amez-Droz, M. Tunon de Lara, A. Amorosi, P.Lambert, C.Collette, C.Caucheteur *Investigating Fused Silica Bending Strength and Damping Characteristics on Resonators Fabricated through Femtosecond Laser-Assisted Wet Etching: An Experimental Analysis* International Conference on Manipulation, Automation and Robotics at Small Scales - Delft July 2024.

Posters

A. Amorosi, **L. Amez-Droz**, B. Ding, J. Watchi, Z. Guoying, P. Lambert, A. Deraemaeker, C. Collette *Low-frequency high-resolution optical inertial sensors* Gravitational Wave Advanced Detector Workshop - Online 2021.

A. Amorosi, **L. Amez-Droz**, C. Collette *Low-frequency high-resolution optical inertial sensors* Gravitational Wave Advanced Detector Workshop - Online 2022.

L.Amez-Droz, M. Tunon de Lara, C.Collette, C.Caucheteur, P.Lambert *Instrumented Flexible Glass Structure: A Bragg Grating Inscribed with Femtosecond Laser Used as a Bending Sensor* Ècole thématique du CNRS Surfaces Interfaces de Verre - Ile d'Oléron October 2023.

Contents

List of Figures

List of Tables

List of Abbreviations

AQG Atomic Quantum Gravimeter
BG Bragg Grating
DAQ Data Acquisition System
DoF Degree of Freedom
EMR Euregio Meuse-Rhin
ETEST Einstein Telescope EMR Site & Technology
E-VINS ETEST Vertical Inertial Sensor
FBG Fibre Bragg Grating
FDM Fused Deposition Molding
FNRS Fond National de la Recherche Scientifique
HINS Horizontal Inertial Sensor
INFuSE Instrument Flexible Glass Structure
IR Infrared Radiation
ISMA International Conference on Noise and Vibration Engineering
MARSS Annual International Conference on Manipulation, Automation and Robotics at Small Scales
MEMS Microelectromechanical systems
NA Numerical Aperture
NI National Instruments
NOSE Non-magnetic Optical inertial SEnsor
OSA Optical Spectrum Analyzer
PD Photodiode
PDR Projet de Recherche
PML Precision Mechatronics Laboratory
SPIE International Society for Optics and Photonics
TED Thermoelastic Damping
TIPs Transfers, Interfaces & Processes
ULB Université libre de Bruxelles
ULiège Université de Liège
UV Ultraviolet

VCA Voice-Coil Actuator
VINS Vertical Inertial Sensor
µVINS micro Vertical Inertial Sensor

1 Introduction

1.1 INFuSE Project

The INFuSE project is financed by an FNRS PDR grant. It started in 2020 with two PhD students, myself and Matéo Tunon de Lara, and three Professors, Christophe Collette of the University of Liège and Université libre de Bruxelles, Pierre Lambert of the Université libre de Bruxelles and Christophe Caucheteur of the University of Mons. This project started with the aim of developing resonators for inertial sensors and sensor arrays that incorporate photonics for force/strain and biochemical sensing. It brings together two crucial components to achieve this goal. The first component is the unique characteristics of glass, which makes it an ideal material for resonators and precision mechanics. Glass has a low loss factor, making it excellent for resonators, and a low thermal expansion rate, perfect for precision applications. It also has an optical quality surface finish and optical properties that can allow measuring deformation through photoelasticity or Bragg gratings. Additionally, glass has a high elastic limit-to-Young's modulus ratio, which is beneficial for force sensors that require both high resolution and a wide measurement range. However, working with glass at scales smaller than 1 mm is challenging. The second key component that addresses this challenge is the recently acquired FEMTOprint machine. This innovative equipment allows for 3D printing of micro-devices from glass and other transparent materials with sub-micron precision. This capability enables the integration of fluidic, optical, and mechanical functions into single monolithic structures at nano- and micro-scale. The technology uses a two-step process: direct laser writing followed by chemical wet etching. This technique has a wide range of applications, including precision mechanics with flexure hinges, microfluidics, micromolding, and micro-optics. It can create microlenses, diffractive optical elements, nanogratings, waveguides, lab-on-fibre structures, and integrated optical monitoring and sensing systems. The latter application is the primary focus of this project.

1.2 Context and Motivations

Flexure Mechanisms Flexure mechanisms, also known as compliant mechanisms, rely on the elastic deformation of materials to achieve motion or force transmission without traditional joints. They are used in applications where smooth, precise, and repeatable motion is required.

Material Selection for Flexure Mechanisms The choice of material for designing flexure mechanisms is crucial because it influences the mechanism's performance, durability, and manufacturing feasibility. The material should have high elasticity, to allow reversible deformation under stress without enduring permanent deformation. It should also resist fatigue to maintain its mechanical properties during its operational life, especially for resonator applications. The material should have high yield strength to maximize its operating range and sustain high loads. It should also be ductile so it can endure shocks without cracking or breaking. Especially for resonators, to keep consistent performance over time, the material should have a low level of energy loss during deformation. Finally, depending on the application, it should have good corrosion resistance and temperature change resistance, especially for mechanisms exposed to harsh conditions.
Considering these characteristics, here is a list of common materials used for flexure mechanism design:

- Stainless steel: it has high strength, good elasticity, corrosion resistance and fatigue resistance.
- Titanium alloys: they are known for their high strength-to-weight ratio, excellent corrosion resistance, and fatigue resistance.
- Spring steels: they are known for their high elasticity and fatigue resistance.
- Copper-Berylium alloys: after heat treatment, they are known for their high yield strength and can be used for high-load applications. they also have good fatigue resistance and corrosion resistance.
- Silicon: it is the most used material for micro-scale flexure mechanisms. thanks to its semiconductor properties and high elasticity and thermal stability, it is the base material for microelectromechanical systems (MEMS).

The main properties criteria are compared in figure 1.1 and listed in table 1. The main point is to compare them to fused silica glass.

Interest for Fused Silica Glass is one of the keys to this research project. Nowadays, the good properties of glass have not been extensively used for compliant mechanisms. As glass is a brittle material, it cannot endure short and intense shocks. And then, it is not adapted for a hostile environment. Glass is also difficult to manufacture. There is no such method as electro-discharge machining of metals for glass. However, a new process developed during the "Femtoprint Project" [7] allows the manufacturing of 3D shapes out of glass material. The left

diagram of figure 1.1 compares the elastic range and the stiffness of usual materials for flexure hinges. The elastic range is quantified as a coefficient proportional to the largest bending angle of a cantilever beam. The geometry is limited by the manufacturing process. The yield strength and Young's modulus depend on the material. Glass has one of the largest elastic ranges. It is also softer than the best other material options which makes it an exceptional candidate for compliant mechanism design. Other material properties are also important depending on the application. For low-frequency inertial sensors (< 1 Hz), the resolution is usually limited by the thermal noise [72]. The part of the thermal noise which depends on the material comes from the internal damping in the flexure hinges. It is quantified as the mechanical loss factor. The precision sensors need also the lowest sensitivity to temperature gradient possible. The right diagram of figure 1.1 shows that glass has both the lowest loss factor and thermal expansion coefficient. Fused silica is then a material of choice for resonator design.

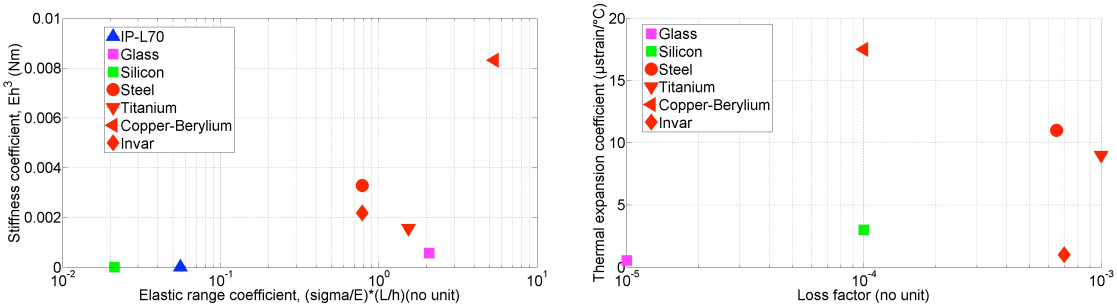

Figure 1.1: On the left, stiffness as a function of elastic range for usual materials for flexure hinges (Source: Ashby diagrams). On the right, the thermal expansion coefficient and mechanical loss factor for those materials.

Material Selection for Optical Structures The material should have the appropriate refractive index and high transparency across the desired wavelength range. It should also have good mechanical and thermal stability to prevent warping or deformation. Finally, it should be suitable for precision machining and coating processes.
The most used material for optics is fused silica. It has a high transparency and low dispersion and it has good mechanical and temperature stability. For specific applications, transparent plastics such as Polycarbonate or PMMA can be used. They are lightweight and easier to mould than glass. Ceramics such as Zerodur are also used but are useful mainly for high-precision large-scale optics such as telescopes. It has a very high temperature and mechanical stability but is difficult to machine, especially for small-scale structures.

Fused Silica Manufacturing A FEMTOprint machine is available at the laboratory in Brussels. It allows to manufacture the micro and macro-scale structures through femtosecond laser-assisted wet etching [7]. It is a two-step process. First, a femtosecond laser is used to illuminate the shape of the designed part in a fused silica substrate. Then, the substrate is bathed in a

glass etchant such as KOH or HF. So, the illuminated volume of the substrate is etched faster than the non-illuminated volume. It allows to manufacture the high aspect ratio structures such as flexure mechanisms. Another technique can also be used to manufacture fused silica structures. It is an additive manufacturing process of fused silica [82]. A photopolymer-silica nanocomposite is illuminated tomographically. Then, the substrate is sintered to result in a fused silica part. The minimum feature size is 20 µm with a surface roughness of 6 nm.
Concerning the optical sensor structures, the femtosecond laser of the FEMTOprint machine can also be used to design optical elements.
Bragg gratings (BG) engraved in a glass substrate can then be merged with flexure manufacturing. It is possible to engrave directly the BG inside the flexure. This allows us to directly measure strain in the flexure itself. In this work, different methods are applied to characterize this sensor technology and their application opportunities will be discussed.

1.3 Objectives

The objectives of this work revolve around exploring the implementation and impact of femtosecond laser-assisted wet etching on flexure specimens and fused silica structures at the micro-scale. Key goals include understanding the limitations of this process and evaluating the mechanical properties, such as bending strength and thermoelastic damping, of structures created with this technique.
Another focus is to assess the feasibility of assembling fused silica monolithic structures with metallic parts, investigating whether this integration improves the mechanics of inertial sensors and identifying critical design aspects for vertical inertial sensor mechanisms.
Additionally, the work aims to determine if Bragg gratings can be inscribed within flexible structures during manufacturing and whether they are suitable for monitoring deformation, as well as their limitations.
Finally, the study seeks to address various factors crucial for practical applications, including how flexible glass structures behave in water, the effects of temperature gradients on measurements, and potential compensation methods. These objectives are designed to broaden the understanding and application of advanced materials and sensor technologies.
The overview of the work plan of the INFuSE is detailed in figure 1.2. My work follows the left side of this plan. First, I study glass flexure manufacturing through femtosecond laser-assisted wet etching. From this study, on one side, the mechanical properties of the structures can be studied. On the other side, they can be used to design and characterize Bragg grating sensors. For this step, the optical inscription such as waveguide and Bragg gratings needs to be defined. Then, those Bragg grating sensors can be specified for their use in flexible structures. Finally, applications benefiting from this work are discussed. Inertial sensors can benefit from glass flexure manufacturing and assembly. Instruments can be designed in a monolithic structure benefiting from the studied Bragg grating sensor technology. For example, the force applied by a surgical instrument could be monitored.

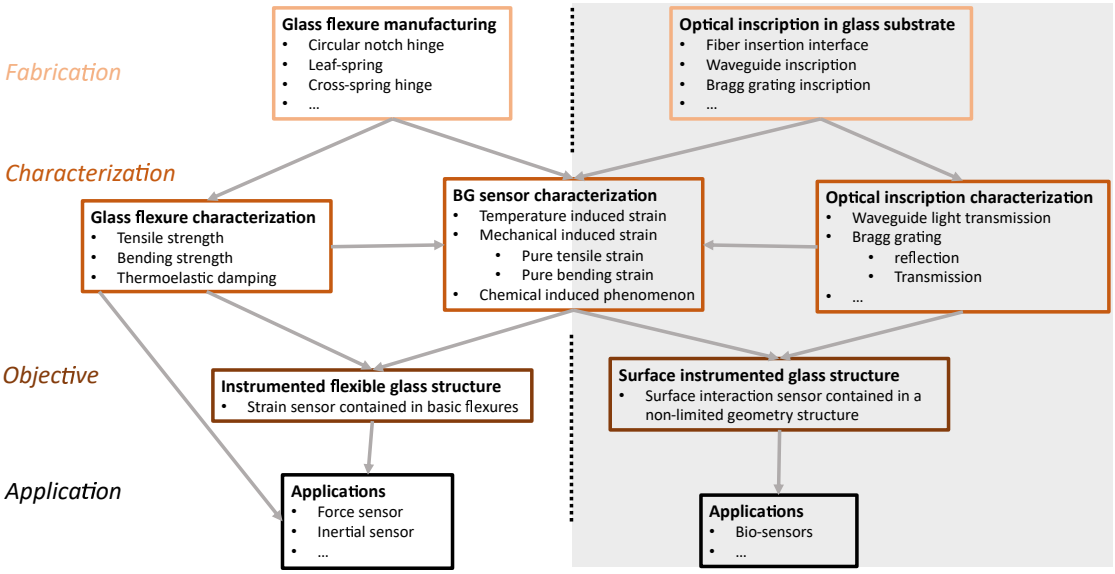

Figure 1.2: Overview of the INFuSE project. The left part describes the mechanical research and the left part describes the optical research.

Questions Addressed in this Thesis

- How can we implement the femtosecond laser-assisted wet etching process to manufacture flexure specimens? What are the limitations of this process?
- What are the mechanical properties of fused silica structures at the micro-scale manufactured through femtosecond laser-assisted wet etching? What is the bending strength of this material? Can its thermoelastic damping be quantified?
- Can fused silica monolithic structures be assembled with metallic parts? Does it improve the mechanics of an inertial sensor? What are the critical aspects of the design of a vertical inertial sensor mechanism?
- Can Bragg gratings be inscribed inside flexible structures during manufacturing and can they be used to monitor their deformation? What are the limitations?
- What does need to be assessed to open perspectives for applications of instrumented flexible glass structures? Mainly, how do they behave in water? How do temperature gradients affect the measurement? Can it be compensated?

1.4 Contributions

The major scientific contributions of my work are listed in this section. They are then detailed in the manuscript.

- The new glass structure manufacturing technique available at our laboratory, called femtosecond laser-assisted wet etching, is used to obtain various flexible structures. Three-dimensional monolithic structures are obtained. Their smallest thickness can be

as low as 10 µm. This contribution is detailed in 3.1.1.

- The annealing of glass structures is performed. The status of this work does not show any improvement. However, the importance and the cleaning procedure of the parts before annealing is demonstrated. Acids such as acetic acid must be used to clean the parts before annealing. This contribution is detailed in 3.1.2.
- An estimation of the bending strength of fused silica specimens is performed. The maximum estimated stress obtained is 2.6 GPa. The maximum bending stress to be considered for flexure specimens at the micro-scale is 1 GPa. This contribution is detailed in 3.2.
- Ring-down experiments are performed on resonators based on fused silica flexure joints. It is performed to assess the internal damping of structures knowing that fused silica is known for its low-damping behaviour. Two experiments are performed. The first studies a micro-scale monolithic resonator. It showed that the quality factor is limited by the air pressure obtained in the vacuum tank. A quality factor is estimated: $Q \approx$ 185'000 obtained at a pressure $p = 2 \times 10^{-3}$ mbar. The second experiment studies an aluminium pendulum hanging on a fused silica flexure joint. The quality factor is limited to $Q = 25'000$ below a pressure $p = 1$ mbar. This contribution is detailed in 3.2.
- The mechanism of two different vertical inertial sensors is defined and manufactured. The first one fits in a $10 \times 10 \times 10$ cm^3 box. The second is larger and features orientation tuning of its readout. It is also easier to mount and some parts can be detached from the rest without dismounting everything. It shows that glass flexure joints can be assembled into aluminium and stainless steel parts. However, their assembly is difficult. So, other flexure parts are proposed manufactured in different materials such as Copper-Beryllium or Titanium. An optimization experiment is performed to define the dimensions of such flexure joints. The open-loop transfer function of the first sensor is compared to a reference sensor Guralp GS13. It shows a good coherence between 200 mHz to 100 Hz. The astatic leaf-spring suspension used for hanging the proof mass is optimized experimentally. It shows that considering a fixed inertia of a proof mass and a fixed length of leaf-spring suspension, the placement of its clamping points influences the natural resonance frequency of the mechanism. To minimize this resonance, the clamping points shall be as low as possible from the hinge of the proof mass. This contribution is detailed in 4.
- Bragg grating sensors are inscribed in flexure specimens. Tensile and bending experiments characterize their sensitivity. It compares to the theory with a sensitivity of $\frac{\Delta\lambda}{\epsilon} \approx 1.2$ pm/µε with a standard deviation of about 10 pm which is limited by the optical spectrum analyzer. The Bragg grating wavelength is obtained by extracting the centroid of the reflected spectrum. This contribution is detailed in 5.
- A method to compensate for the temperature gradient of Bragg grating sensors is proposed. The test bench is not ready to perform a characterization yet though. This contribution is detailed in 6.

1.5 Structure of the Thesis

Chapter 2 presents a State of the Art of the different aspects studied in this work. First, it details the properties of fused silica and how a femtosecond laser can modify its structure. Then, different examples of mechanisms obtained using the femtosecond laser-assisted wet etching process are presented. And then, a small review of inertial sensor designs is presented.
Chapter 3 describes the manufacturing of flexible structures through femtosecond laser-assisted wet etching. It also proposes an annealing process. Then, it explains how the bending strength of the manufactured specimen is assessed. It also describes two experiments to measure the damping characteristics of resonators based on fused silica flexure joints.
Chapter 4 presents the design process of flexure mechanisms used for two vertical inertial sensors. It starts with the study of an inertial sensor designed for integration in an atomic quantum gravimeter. It then follows with a suspension mechanism experimental study for the design of a second vertical sensor. This one is used to isolate a mirror from ground vibrations used in a gravitational wave detector.
Chapter 5 describes how a Bragg grating sensor is designed to be manufactured by femtosecond laser-assisted wet etching. It explains how a glass structure is instrumented. Then, the axial strain sensitivity of the Bragg grating sensor is characterized through a tensile test and three different bending tests. It includes a bending test of a Bragg grating sensor inscribed in a flexure hinge joint. It also proposes an experiment to analyze a Bragg grating sensor in a structure in torsion.
Chapter 6 presents experiments to assess the Bragg grating sensor for future application perspectives. First, it verifies that the sensor behaviour is not altered by the liquid water environment. Then, it proposes a method to compensate the sensor measurement for temperature gradients. It also introduces the opportunity to manufacture an instrument flexible structure at the end of an optical fibre.

Reading suggestions This manuscript contains topics that are related to the flexure mechanism design and the interest in fused silica. For readers interested in inertial sensor mechanics or resonators, the reading suggestion is to begin with the reading of Chapter 3 and continue with Chapter 4. For the readers interested in Bragg grating sensors, the reading suggestion is to start with the reading of Chapter 3 and continue with Chapters 5 and 6.

2 State of the Art

This chapter presents the previous studies establishing the groundwork of INFuSE. Section 2.1 describes the material properties of fused silica. Then, studies exploring the modelling of the glass properties using a femtosecond laser are listed in 2.2, notably introducing Bragg gratings. The different machining processes for flexure mechanism manufacturing are introduced in 2.3. Section 2.4 presents examples of glass flexure mechanisms manufactured by femtosecond laser-assisted wet etching. Finally, some previous works on the challenges of vertical inertial sensor mechanical design are described in 2.5.

2.1 Fused Silica

Fused silica glass has one of the largest elastic ranges ($\sigma_Y/E \approx 0.02$ with σ_Y, its bending elastic limit or yield strength and E, its Young's modulus), making it an exceptional candidate for compliant mechanism design (the typical σ_Y/E of Steel and TiAl6V4 are respectively 0.004 and 0.007).

2.1.1 Mechanical Strength

Fused silica is a brittle material, its mechanical strength depends mainly on its surface quality, and thus, on its manufacturing process. As the intrinsic strength of the Si-O bond is in the order of 21 GPa, approaching this limit can be an opportunity to design highly elastic flexure mechanisms.

Mechanical Testing

The bending strength of fused silica flexures fabricated by femtosecond laser has been reported [8], it can attain 2.7 GPa. The simplified stress model can be used and has been confirmed by photoelasticity stress measurements inside the flexures. Also, glass manufacturing by femtosecond laser-assisted etching is suitable for high-demanding technologies such as

optofluidics, optomechanics, marking and photonics [7]. Later, a monolithic structure was designed to perform tensile tests on a fused silica sample without the necessity to interact with the specimen mechanically [3]. A novel passive actuation structure, called stressors, is used to load the specimen using the femtosecond laser. Laser-affected zones exhibit a net volume expansion and thus stress. They reached stress levels up to 2.4 GPa.

Defects

Brittle-fracture statistics of fused silica under femtosecond laser exposure have been studied [5]. The Weibull statistics were extracted by following the apparition of chaotic patterns along exposed lines where periodic nano-gratings are expected. This defect can result from different phenomena such as plasma dynamic relaxation, the excitons dynamics, the crack nucleation rate of pulses as well as the scanning velocity. Also, the volume expansion in the laser-affected zone causing high-stress concentration at the end of the nano-planes of the nano-gratings can be a source of cracks.

Annealing

Concerning the possible enhancement of fused silica part mechanical strength, it has been demonstrated that their strength can be increased by annealing [89]. Annealing the part at 1200 °C resulted in a mechanical strength increase from 8 GPa to 10 GPa due to the reduction of surface stress concentration. These tests were performed by applying compressive stress on the specimens.

2.1.2 Temperature Stability

Fused silica has strong temperature stability in terms of dilatation (~ 0.5 ppm/°C). However, for precision mechanisms, its temperature coefficient of elasticity is not negligible (~ 220 ppm/°C). Irradiating amorphous silica with a femtosecond laser can decrease its temperature coefficient of elasticity beyond 50% [86].

2.1.3 Low Damping Quality Factor

For low-frequency inertial sensors (< 1 Hz), the resolution is usually limited by the thermal noise [72]. The part of the thermal noise which depends on the material comes from the internal damping in the flexure joints. It is quantified as the mechanical loss factor (down to 10^{-5} for fused silica). The precision sensors also require the lowest coefficient of expansion (5.2×10^{-5} K^{-1} for fused silica).

2.2 Fused Silica Optical Properties Modeling Using a Femtosecond Laser

Femtosecond pulse lasers are powerful tools used in a variety of industrial applications [53]. A prominent example remains the processing of glass using femtosecond pulse laser [87]. This process involves the use of a tightly focused high-powered laser beam to create precise cuts, holes, and patterns within the glass and on its surface. The laser beam can be focused to a very small spot size, such that the non-linear modification can happen in a confined volume that can be smaller than the focal volume. This level of precision is not possible with traditional mechanical or chemical methods. Moreover, the short pulses allow for precise control of the amount of energy delivered to the glass, minimizing heat damage and ensuring high-quality cuts. Depending on the desired outcome, the focused laser beam is usually moved across the glass structure in a predetermined pattern, or focused at specific points to create holes or channels. The process can be controlled using computer software to ensure precise and repeatable results. Complex 3D structures can also therefore be generated by using multiple laser beams focused at different depths [31]. This technique is known as femtosecond laser-assisted chemical etching and has a wide range of potential applications, such as creating microfluidic channels or optical components [10]. The mechanism of the material modification under a focused femtosecond pulse laser has been the subject of intense research [11, 8, 10]. In glass, it has been demonstrated that three types of material modification can be generated depending on the properties of the used femtosecond pulse laser [11, 38, 80, 43], i.e. pulse energy and duration [11, 38], repetition rate and scanning speed and scanning speed and direction as well as polarization [45]. Hence, with increasing energy density levels the silica glass undergoes different structural changes:

1. Densification [21, 96], which induces a local and isotropic modification of the refractive index at the focal point and can lead to the creation of optical waveguides [92, 18]. Most recently, localized permanent densification has been obtained between non-overlapping simultaneous femtosecond laser-affected zones while preserving the integrity of the material [66]. This method can be used for non-contact laser-induced high-pressure studies (a few tens of GPa).
2. Nano-grating corresponding to a structural change of the material that usually takes the form of an alternation of fused silica nanoplanes and nanochannels perpendicular to the incident polarization of the laser beam [38]. Femtosecond laser to fabricate birefringent surface elements in fused silica [30]. Written nanogratings exhibit up to a three-fold increase after polishing and 25 h of KOH etching at room temperature. This led to achromatic behaviour over the entire visible spectral range enabling opportunities for micro-optics applications. Induced form birefringence in fused silica using a femtosecond laser can be used to obtain circular-polarization beam splitters [12]. The birefringence results from the spontaneous formation of subwavelength periodic structures oriented perpendicular to the writing beam polarization in the focal volume. Studying the formation of nanogratings in fused silica using a femtosecond laser, it has

been demonstrated that they can resist extremely large temperatures up to 1150°C [68]. Also, formed birefringence can be tuned precisely to manufacture phase elements such as quarter- and half-wave plates.

3. Direct ablation is the scenario where the energy of the pulse is amplified to a significant degree, resulting in void creation within the exposed material sample [31, 52].

2.2.1 Bragg Gratings

Modification of the Material For the grating inscription, unlike the standard writing methods with ultra-violet continuous or nanosecond pulse laser, the advent of tight focusing of femtosecond pulse laser has allowed, through nonlinear absorption and tight focusing, to produce gratings in different materials including pure silica [44]. Typically, each pulse of the femtosecond laser engraves permanently one period of the grating through a nonlinear absorption process. In optical fibres, Bragg gratings are usually produced by the point-by-point [55], line-by-line [21] or plane-by-plane [77] manufacturing processes and show unprecedented resistance among the photonic sensing devices to high temperature and harsh environment [48]. Temperature sensing up to 1050 °C has been successfully reported [58]. Driven by the need and advances in technology, numerous companies developed femtosecond pulse laser-induced FBGs nowadays. Besides, the planar glass substrates processing by femtosecond laser has attracted the attention of researchers thanks to the many possibilities they offer for device integration [53, 87]. Efforts have been made to optimize pulse laser parameters [80, 38], beam shaping [75], waveguide design[71], to produce low-loss waveguides [76], waveguide and Bragg grating within, [48, 78] and many other optical components.

Bragg Grating Sensors FBG can be placed on or in a structure to measure axial strain along with the fibre. A review of this technology and its applications are presented in [17]. This technology can be applied on a macro scale up to a very large scale. The minimum scale is limited by the fact that an optical fibre has to be merged with the specimen. Zhang et al. [95] demonstrated a method to integrate strain-optic and thermo-optic Bragg grating sensors in bulk fused silica using an ultrafast laser. Their Bragg grating sensors are thermally stable to 500°C. Also, BG strain sensors made in bulk materials are presented in [69] and [70] in polymers and [95] in fused silica. The reported sensibilities to strain are respectively 2.95 pm/με and 1.10 pm/μεfor the polymer sensors and 1.38 pm/με, -1.27 pm/με for the fused silica sensors. The last one was obtained by bending a fused silica plate composed of waveguide BG. Polymer BG strain sensors give strong sensibility to strain due to their low elastic modulus compared to fused silica. This material is not suitable for high-precision sensors due to its lack of stability to temperature, thermoelastic damping and usually low yield strength.

The axial strain is defined as $\epsilon = \frac{\Delta\Lambda}{\Lambda}$ with Λ, the refractive index modulation period. It can be obtained from the Bragg wavelength shift $\Delta\lambda_{\text{Bragg}}$. This shift is coupled with the temperature

effect $\frac{\Delta\lambda_{\text{Bragg}}}{\Delta T}$ and the mechanical strain effect $\frac{\Delta\lambda_{\text{Bragg}}}{\Delta\epsilon}$. The complete development can be found in [20].

$$\Delta\lambda_{\text{Bragg}} = 2\left(\Lambda\frac{\mathrm{d}n_{\text{eff}}}{\mathrm{d}T} + n_{\text{eff}}\frac{\mathrm{d}\Lambda}{\mathrm{d}T}\right)\Delta T + 2\left(\Lambda\frac{\mathrm{d}n_{\text{eff}}}{\mathrm{d}\epsilon} + n_{\text{eff}}\frac{\mathrm{d}\Lambda}{\mathrm{d}\epsilon}\right)\Delta\epsilon \tag{2.1}$$

Using the definition of the Bragg wavelength the strain dependant term in Equation (2.1) can be rewritten as

$$\frac{\Delta\lambda_{\text{Bragg}}}{\Delta\epsilon} = \frac{\lambda_{\text{Bragg}}}{\Lambda}\frac{\mathrm{d}\Lambda}{\mathrm{d}\epsilon} + \frac{\lambda_{\text{Bragg}}}{n_{\text{eff}}}\frac{\mathrm{d}n_{\text{eff}}}{\mathrm{d}\epsilon} \tag{2.2}$$

$$\frac{\Delta\lambda_{\text{Bragg}}}{\Delta\epsilon} = \lambda_{\text{Bragg}}\left(1 + \frac{1}{n_{\text{eff}}}\frac{\mathrm{d}n_{\text{eff}}}{\mathrm{d}\epsilon}\right) \tag{2.3}$$

$$\frac{\Delta\lambda_{\text{Bragg}}}{\Delta\epsilon} = \lambda_{\text{Bragg}}(1 - p_{\text{e}}) \tag{2.4}$$

For silica glass, which is an isotropic material, the strain-optic constant p_{e} can be obtained from [20] as

$$p_{\text{e}} = \frac{n_{\text{eff}}^2}{2}[p_{12} - \nu(p_{11} + p_{12})] \tag{2.5}$$

The elasto-optic independent coefficients for bulk silica are listed in [93] ($p_{11} = 0.121$ and $p_{12} = 0.270$). The Poisson's ratio and the effective refractive index are estimated as respectively $\nu = 0.16$ and $n_{\text{eff}} = 1.45$.
For FBG, as described in [20], these parameters are different as the core of the fibre is Ge-dopped silica ($p_{11} = 0.113$, $p_{12} = 0.252$, $\nu = 0.16$ and $n_{\text{eff}} = 1.482$). It gives sensitivity to axial strain at 1550 nm of around 1.2 pm/με.

2.3 Fused Silica Machining Process

2.3.1 Femtosecond Laser-Assisted Wet Etching

Manufacturing three-dimensional parts in fused silica with a micrometric resolution is now a reality. The process is performed in two parts. First, a femtosecond laser exposure is applied on the glass substrate following the shape of the designed part. Then, the substrate is placed in a chemical bath for wet etching. Bellouard *et al.* [7] have shown that this method can fabricate microstructures with high aspect ratios. This aspect ratio (100:1 with Thorlabs 10x laser objective and using KOH as etchant) allows the fabrication of monolithic flexible joints even in thick substrates (2 mm and 5 mm). With the commonly used Thorlabs 20x laser objective and a pulse energy of 240 nJ, the material in the laser-affected zone undergoes a

volume expansion by the introduction of pores or nano-gratings [19]. Local densification appears at the interface of regular patterns in the laser affected zone [10]. The enhancement of the etching rate may be explained by the Si-O-Si bond angle deformation induced by the local stress in the proximity of the compacted regions and by the presence of lower order ring structures in the laser affected zone [10, 67]. The optimal energy deposition value to maximize HF's fused silica etching rate has been studied [67]. The femtosecond laser-assisted etching process has been optimized by tuning the energy dose and the use of various etchants [19]. They even demonstrated that using NaOH, a less dangerous etchant, enables a higher etching rate than currently used HF and KOH resulting in higher aspect ratio manufacturing.

2.3.2 Fused Deposition Modeling and Sintering

Femtosecond laser-assisted etching is not the only method to manufacture micro-scale glass structures. Toombs et al. [82] presented an additive manufacturing process of fused silica. A photopolymer-silica nano-composite is illuminated tomographically. Then, the substrate is sintered to result in a fused silica part. The minimum feature size is 20 μm with a surface roughness of 6 nm.

2.4 Fused Silica Flexure Mechanisms

Fused silica flexure mechanisms have been designed for various applications. Bellouard et al. [9] presented a monolithic optomechanical micro-displacement sensor (50 nm resolution). The sensitive element is translational guidance containing an integrated linear encoder. The displacement is measured optically through an integrated waveguide in the sensor frame that is opened facing the linear encoder perpendicularly. It is one of the first instrumented flexible glass structures manufactured by femtosecond laser-assisted wet etching. Lenssen and Bellouard [50] demonstrated a transparent glass monolithic micro-actuator. The actuation is performed by capacitive comb-array. A transparent conductive material (indium-tin-oxide layer) is deposed on the structure. The comb array is guided in translation by a flexure mechanism. It demonstrates that a coating can be deposed on a flexure mechanism to add an actuation function to the structure. Nazir and Bellouard [62] proposed a laser-to-fibre coupling mechanism contained in a monolithic fused silica tunable flexure mechanism (sub-nm resolution positioning over tens of micrometres range of motion). Nazir et al. [60] also used their concept of stressors to load a micro-tensile tester to perform long static stress measurements under normal atmospheric conditions. These works introduce glass flexible structures as a choice for high-precision positioning mechanisms. Zanaty et al. [94] presented a multistable glass monolithic mechanism to perform safe surgical puncturing. The force and stroke applied by the needle at the output of the mechanism are decoupled from the operator input and are tunable (5-20° stroke with a force exceeding 8 mN). Tissot-Daguette et al. [81] presented a constant-force surgical tool based on a monolithic glass flexure mechanism (1 gf with a 0.1 gf maximum variation over a displacement range of 870 μm). A microscope is used

as a visual feedback of the output displacement. These two works support investing in flexible glass structures for surgical applications.

2.5 Inertial Sensor Design

Inertial sensors based on interferometric readout currently offer better performance than conventional seismometers with electromagnetic readout. Sub-picometer resolutions have been achieved using Michelson interferometric readings of the proof-mass motion of inertial sensors [98, 28, 35, 24]. The sensors (VINS and HINS) designed by B. Ding [29] improve the concept of the STS-1 sensor [91]. The VINS has a resolution of 2×10^{-13} m/$\sqrt{\text{Hz}}$ at 1 Hz and has a principal resonance frequency at 260 mHz.
The Precision Mechatronics Laboratory (PML) has been active in the conception of low-frequency inertial sensors for more than a decade. Here is a list of the previous vertical inertial sensors developed at PML:

- The NOSE (figure 2.1) offers a high-resolution inertial sensor for low cost [27]. It is based on CuBe leaf-spring joints and its readout consists of a Michelson interferometer. it has a resolution of 3 pm/$\sqrt{\text{Hz}}$ above 4 Hz. It is characterized by an inertial mass $M = 55$ g, a principal resonance frequency $f_0 = 6$ Hz and spurious resonances above 100 Hz.

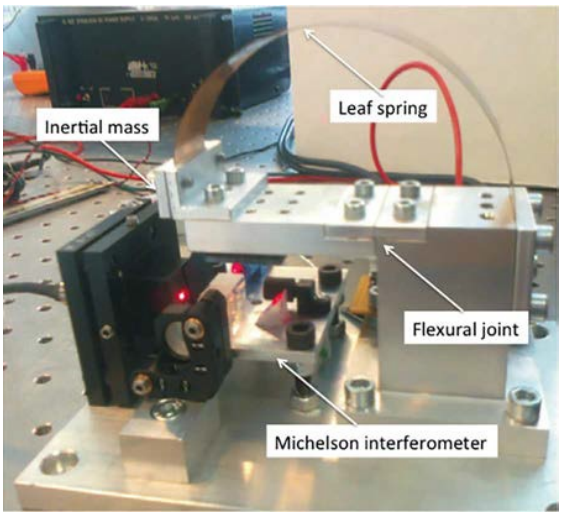

Figure 2.1: NOSE, interferometric inertial sensor [27]

- The linear encoder-based inertial sensor (figure 2.2) offers a high resolution, compact and easy-to-mount inertial sensor [36]. it is based on a circular notch parallelogram guidance with a prestressed leaf spring as a suspension. Its readout consists of a linear encoder. it has a resolution of 10 pm/$\sqrt{\text{Hz}}$ above 4 Hz. It is characterized by an inertial mass $M \approx 200$ g, a principal resonance frequency $f_0 \approx 15$ Hz and spurious resonances above 100 Hz. [36] provides promising concepts to improve its resolution using an amplification mechanism.

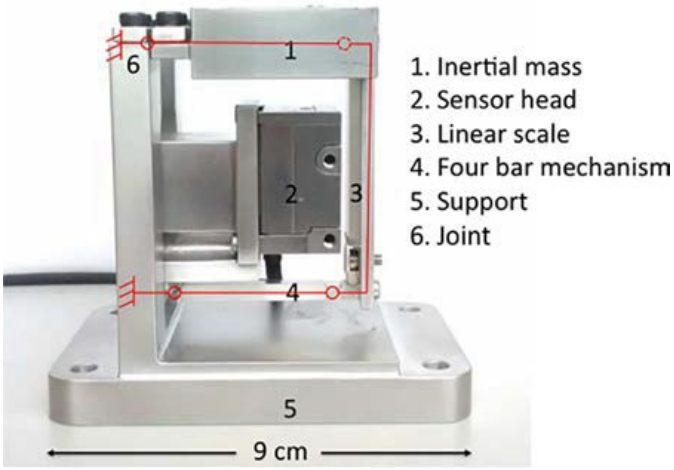

Figure 2.2: Linear encoder based inertial sensor [36]

- The Vertical Inertial Sensor (VINS, figure 2.3) offers a high-resolution inertial sensor that outperforms the commercial of the shelf products [29]. it is based on the STS-1V sensor from Streckeisen. it is based on a cross-spring hinge and a CuBe leaf-spring suspension. Its readout consists of a novel long-range Michelson interferometer. it has a resolution of 2×10^{-13} m/$\sqrt{\text{Hz}}$ at 1 Hz. It is characterized by an inertial mass $M = 600$ g, a principal resonance frequency $f_0 = 260$ mHz and spurious resonances above 70 Hz (but limited from 20 Hz by the readout).

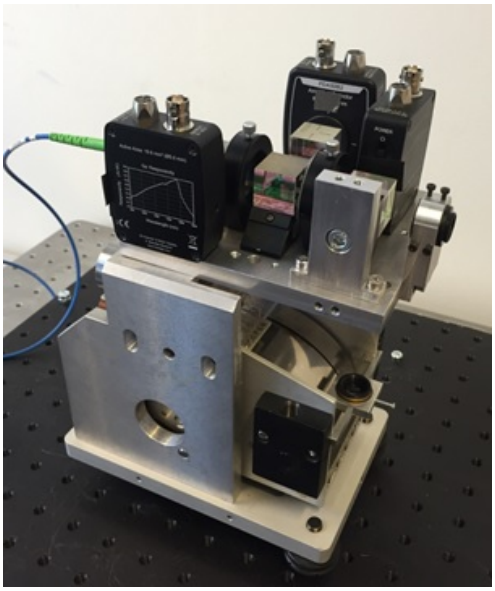

Figure 2.3: VINS, interferometric inertial sensor based on the STS-1V [29]

(a) Guralp GS-13 (b) Trillium 240

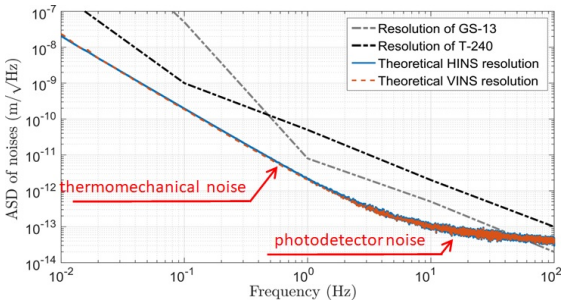

(c) Sensor noise

Figure 2.4: Comparison of the sensor noise of the VINS with the best commercial of the shelf low-frequency inertial sensors [29]

3 Fused Silica Flexures

This chapter details the manufacturing of micro-scale fused silica structure and their mechanical properties. Section 3.1 describes the manufacturing process and the design for manufacturing. Then, an introduction to an annealing process is presented. Next, in section 3.2, to quantify the elastic range of fused silica mechanisms at this scale, an experiment is performed to obtain the bending strength of the material (or its elastic limit). Finally, this material is known for its low internal damping property, the quality factor of oscillators made of fused silica is extracted. This allows us to obtain an estimation of the damping of an oscillator based on a compliant mechanism manufactured by femtosecond laser-assisted wet etching. This experimental analysis is presented at the annual International Conference on Manipulation, Automation and Robotics at Small Scales (MARSS) in Delft in July 2024.

3.1 Manufacturing

3.1.1 Femtosecond Laser-Assisted Etching

Fused silica monolithic structures are obtained using a femtosecond laser included in a machine which is called FEMTOprint. This machine pictured in figure 3.1a features a three-axis precision moving platform (100 nm resolution) on which the glass substrate is fixed (figure 3.1b,c). The UV-grade fused silica glass substrate is provided by Siegert Wafers GmbH. A Thorlabs LMH-20x-1064 or LMH-10x-1064 objective is used to focus the laser (figure 3.1b). The voxel waist is 1.5 μm in diameter and its height is 24 μm using the Thorlabs LMH-20x-1064 laser objective (figure 3.1e). It is 2 μm in diameter and its height is 42 μm using the Thorlabs LMH-10x-1064 laser objective. The selection of the objective depends on the depth of the required machining. The 20x laser objective can be used for machining up to 1 mm depth, while the 10x laser objective can be used for machining up to 5 mm. A microscope is located on top in front of the laser objective. It is used to help select the origin in the machine command to place the toolpath with respect to the glass substrate. It is also used to find the orientation of the glass substrate by selecting different points where the glass-air interface vertical position is detected by moving the laser vertically with a fixed illumination. To define

the laser toolpath, a modified version of the software Alphacam adapted by FEMTOprint SA is used (figure 3.1d). Each parameter of the laser can be tuned independently. After the laser exposition, the substrate is placed in a 12 M Potassium Hydroxide (KOH) bath at 85°C for wet etching (figure 3.1f).

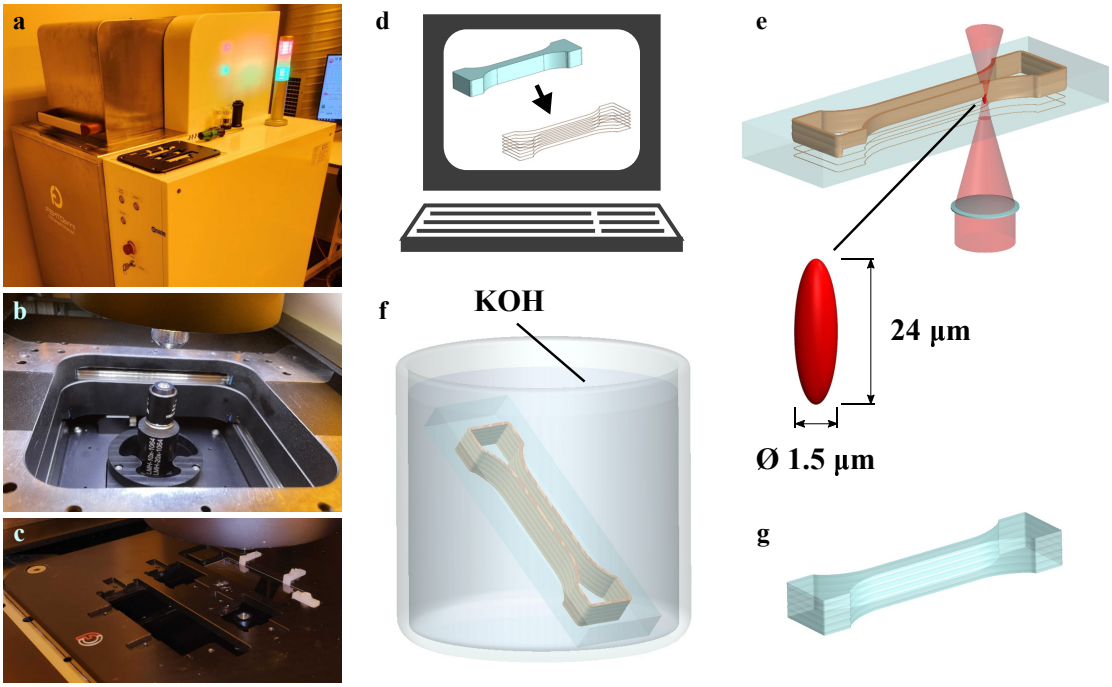

Figure 3.1: Femtosecond laser-assisted etching. **a** The FEMTOprint device is used to perform the laser exposure step. **b** The laser objective is located at the bottom. The microscope at the top is used to calibrate the position and orient the glass substrate correctly. **c** The glass substrate is attached to a holder placed above the laser objective, itself fixed to a moving stage. **d** The laser path is extracted from the 3D model of the designed part. **e** Laser exposure step: the laser path begins at the top of the substrate and finishes at the surface in front of the laser objective. The laser exposed volume is defined by the laser path and the laser voxel dimension. The dimension is assumed according to the FEMTOprint parameters and not measured. The voxel dimension depends on the focusing conditions and laser parameters. (For representation purposes, the proportions are not accurate) **f** Etching step: the substrate is placed in a KOH bath at 85 °C for wet etching. **g** After etching, the finished part is cleaned with pure water.

Figure 3.2 shows an example of the laser toolpath defined to obtain a component by femtosecond laser assisted-etching. To allow the removal of the component, hatching parallel lines are placed everywhere but inside the component volume. This component is part of a custom inertial sensor described in 5.5. The selected vertical pitch for side etching is half of the laser voxel. Beginning the vertical pass two laser voxels high above the glass substrate and finishing two voxels high below it allows for tolerating the thickness variability of the glass

substrate. To perform surface etching, the horizontal pitch shall be less or equal to twice the laser voxel width. To obtain a better surface quality, horizontal passes can be combined both in one direction and in the perpendicular direction. Then, the passes in the perpendicular direction shall be shifted vertically from the other horizontal passes for about 1-2 µm in the vertical direction to prevent high-stress concentration at the surface.

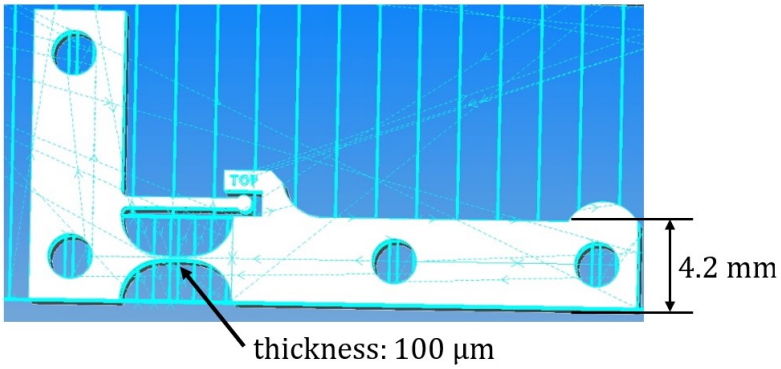

Figure 3.2: Example of the laser toolpath (in light blue) to obtain a component by femtosecond laser assisted-etching. Hatching parallel lines are written to allow the removal of the component.

To perform the wet etching step, the substrate is placed in a polypropylene custom-made net (figure 3.3). It allows to recover the fragile manufactured parts after the etching process. This net is then placed in a polypropylene recipient filled with 12 M KOH. It is then placed in a pure-water container heated at 85 °C. It is also possible to place the recipient in an oven heated at 85 °C. The bath duration is dependent on the geometry of the component to be etched and on the mounted laser objective. Using the 20x laser objective, the etching speed of fused silica in KOH is 130 µm/h. Using the 10x laser objective, the etching speed of fused silica in KOH is 70 µm/h. The etching speed of the non-illuminated fused silica in KOH is 700 nm/h, and the selectivity of the process is 200:1 or 100:1 depending on the laser objective, respectively the 20x and the 10x. Before cleaning it with pure water, the component is left in the KOH container until it attains room temperature. This step ensures safety as 85 °C KOH is a dangerous chemical. After water cleaning, the component is left beside until it is completely dry.

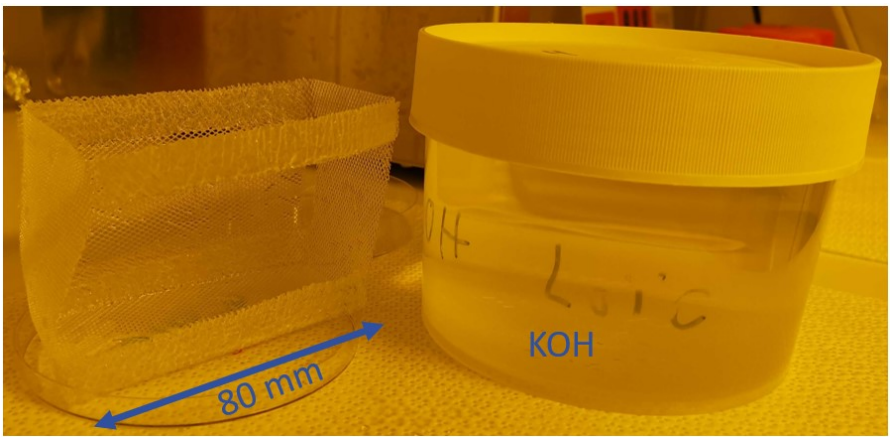

Figure 3.3: KOH Container on the right and a Polypropylene net on the left. The glass substrate to be etched is placed inside the net which is flooded inside the KOH container which is placed inside a pure water ultrasonic bath at 85 °C

Table 3.1 lists a summary of the process parameters according to the mounted laser objective. These parameters are used for all the monolithic fused silica parts machined by femtosecond laser-assisted wet etching in this work unless otherwise specified.

Table 3.1: Femtosecond laser-assisted wet etching process parameters

Laser objective	LMH-20x-1064	LMH-10x-1064
Illumination parameters		
Pulse energy	230 nJ	400 nJ
Repetition rate	1 MHz	650 kHz
Inscription speed	950 mm/min	600 mm/min
Laser voxel diameter	1.5 µm	2 µm
Laser voxel height	24 µm	42 µm
Toolpath vertical pitch	7 µm	20 µm
Toolpath horizontal pitch	3 µm	4 µm
Maximum depth	1 mm	5 mm
Polarization	Perpendicular	
Etching parameters		
Temperature	85 °C	
Etchant	KOH 12 M	
Illuminated fused silica etching rate	130 µm/h	70 µm/h
Non-illuminated fused silica etching rate	700 nm/h	

Flexure Manufacturing Results In summary, the most difficult parts to obtain are presented in this section. Figure 3.4 shows a cross-spring hinge obtained in a 500 µm fused silica substrate. Overall, the smaller the substrate the easier it is to produce. However, this hinge is in 3D and

contains multiple surfacing layers. The difficulty in this manufacturing is the removal of the residual material. I have also managed to manufacture a cross-spring hinge from a 2 mm fused silica substrate. Only the 500 µm thick is shown here due to the lens's limited depth of field.

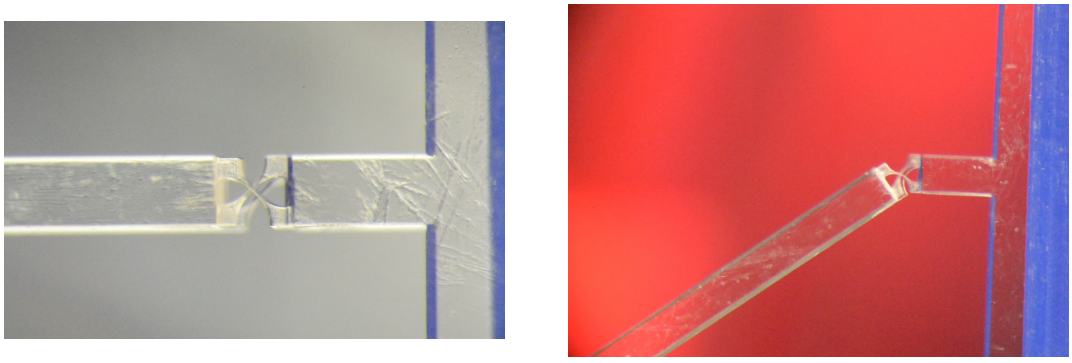

Figure 3.4: Cross-spring hinge manufactured from a 500 µm fused silica substrate. The rigid moving part is 500 µm wide and the central thickness of the flexure beams is 10 µm. On the left, the hinge is at rest. On the right, the hinge is bent at maximum before rupture

Figure 3.5 shows the two stages of the manufacturing process results of a monolithic compliant mechanism. The left picture shows the state of the glass plate after illumination of the shape of the specimens using the femtosecond laser. The right picture shows one specimen after the KOH etching and pure water cleaning. The specimen manufactured corresponds to the Bragg grating sensor design detailed in Chapter 5.

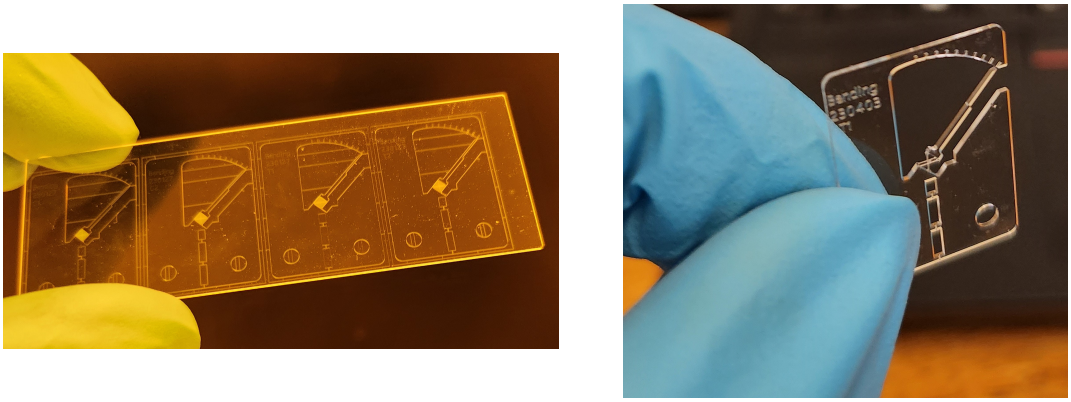

Figure 3.5: Bragg grating sensor tester manufactured from a 500 µm fused silica substrate. On the left, a view of 4 samples inscribed on the same plate with the FEMTOprint machine. On the right, is the view of one finished sample obtained after the KOH wet etching.

Figure 3.6 shows structures composed of circular notch hinges manufactured from a 5 mm fused silica substrate. These structures take the entire volume of the glass substrate. This was difficult to produce due to the optical irregularities close to the sides of the substrate and

its holders. These parts are also really fragile due to their weight and aspect ratio with their flexure hinges. They are used as a mirror guiding mechanism in an inertial sensor, as detailed in Chapter 4.

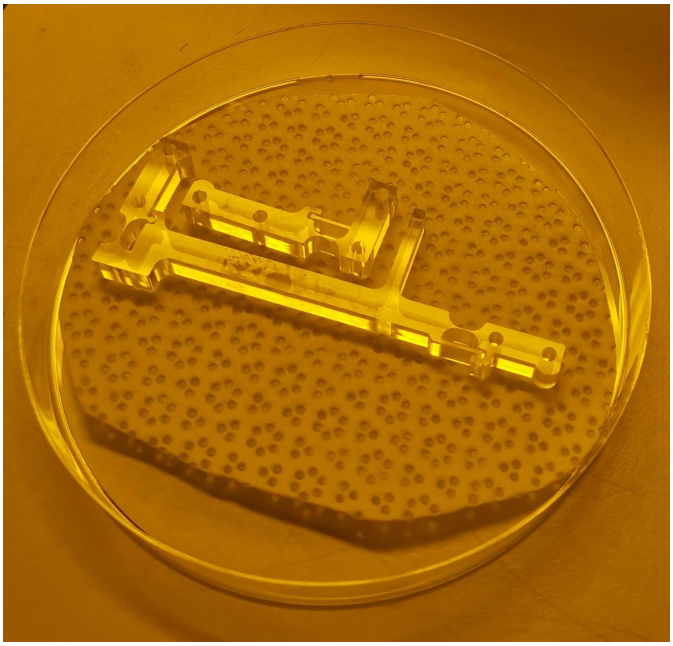

Figure 3.6: Structures are composed of circular notch hinges manufactured from a 5 mm fused silica substrate. This structure is part of a mirror guiding for an inertial sensor optical readout. The circular notch hinges have a central thickness of approximately 80 µm

Figure 3.7 shows a hinge composed of two 50 µm thin leaf springs manufactured from a 2 mm fused silica substrate. The difficulty was finding a way to design easy-to-etch mechanical stops. First, 3D mechanical stops were designed but were not successfully produced due to waste removal complexity. This design includes an easy-to-produce mechanical stop. This stop is obtained leaving a 35 µm gap along the length of the part. This gap is produced by passing 1 time with the laser. So, the original gap is about 3 µm, the width of the laser voxel. Then, the gap increases by etching the non-illuminated material due to the long etching time of the part (22 h). This flexure hinge is used as the guiding joint of a proof mass in an inertial sensor, as detailed in Chapter 4. It is used in combination with the guiding of figure 3.6.

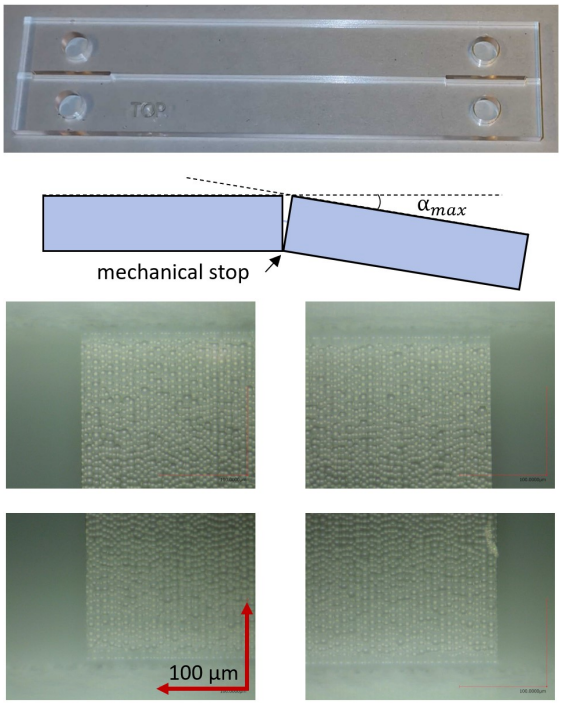

Figure 3.7: On the top, is a flexure hinge composed of 2 leaf-springs manufactured from a 2 mm glass substrate. Each leaf spring is located between the passing holes. They are 7.4 mm wide, 500 µm long and 50 µm thick. On the centre, a scheme of the mechanical stop limits the bending range of the hinge (In the same way as the specimen in figure 3.12c). On the bottom, a close view of the corners of one of the leaf springs. On the surface, the visible craters are the marks of the laser voxel.

Discussion Three-dimensional structures with high aspect ratios such as flexures have been manufactured in our lab using the femtosecond laser-assisted wet etching process. It is a long process for thick part manufacturing. It takes about three to five days to manufacture structures from a 2 mm to 5 mm thick substrate. For example, the flexure joint of figure 3.7 takes about one day of machining, one day of etching and half a day of cleaning and drying. However, this process allows the manufacture of these parts in fused silica glass. Also, as the material is transparent, it can be machined with a contactless method such as using a femtosecond laser. So, complex three-dimensional designs can be manufactured. During my work, the design limit was to manufacture structures with non-vertical or non-horizontal toolpaths. This is due to the Alphacam software complexity. If the "cut" is not vertical, as in figure 3.2, instead of defining a pitch, each horizontal plane toolpath has to be defined manually. This has been improved lately by the newly updated Alphacam from Femtoprint which has a special function to define intelligent surface machining. It has been used to improve the optical fibre mechanical guide described in Chapter 5 for example. Also, figure 3.8 shows a test of free cross-spring hinge manufacturing in a 2 mm substrate in a transverse orientation from the one obtained in figure 3.4. Unfortunately, the wet etching was not a

success. The etchant was not able to penetrate through all the substrate. The pitch of the horizontal layers, the orientation of the toolpath and the hatching need to be investigated.

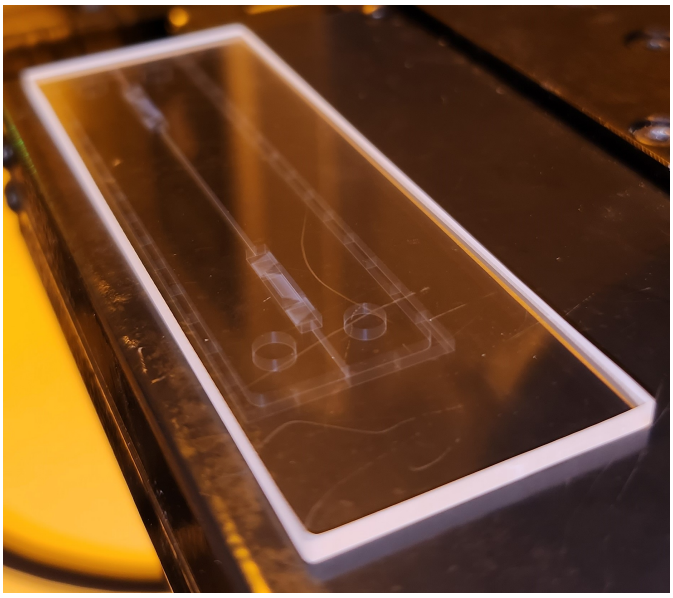

Figure 3.8: Sample example processed using the surface machining macro to manufacture oblique flexure joints using the x10 laser objective. The KOH etching failed. The oblique parts were not etched completely.

3.1.2 Annealing

As demonstrated in [89], fused silica mechanical strength can be increased by annealing the structures after the femtosecond laser-assisted wet etching. It has been reported that their compressive strength was improved from 8 GPa without annealing to 10 GPa for 17 µm diameter pillars with an annealing of 4 h at 1200 °C. We have decided to test this process for our bending specimens. They will then be used to perform bending tests that estimate the bending strength of fused silica in their dimension range. The annealing is performed using a Nabertherm oven. At first, the specimens are cleaned in acid. Pure acetic acid (CH_3COOH) and hydrochloric acid (HCl) are tested as cleaning solutions. The specimens are bathed in acid for 2 x 10 minutes at laboratory temperature. After the first 10 min, the specimens are flipped and the bath continues for 10 min. Afterwards, they are cleaned with pure water. The acid cleaning removes the residual alkali metals such as Potassium or other impurities at the surface. Alkali such as Potassium can adsorb in fused silica during the heating process and crystallize above 700 °C which changes the properties of the structure. Then, after the specimens are dehydrated, they are placed in the oven lying on Platinum pots (figure 3.9).

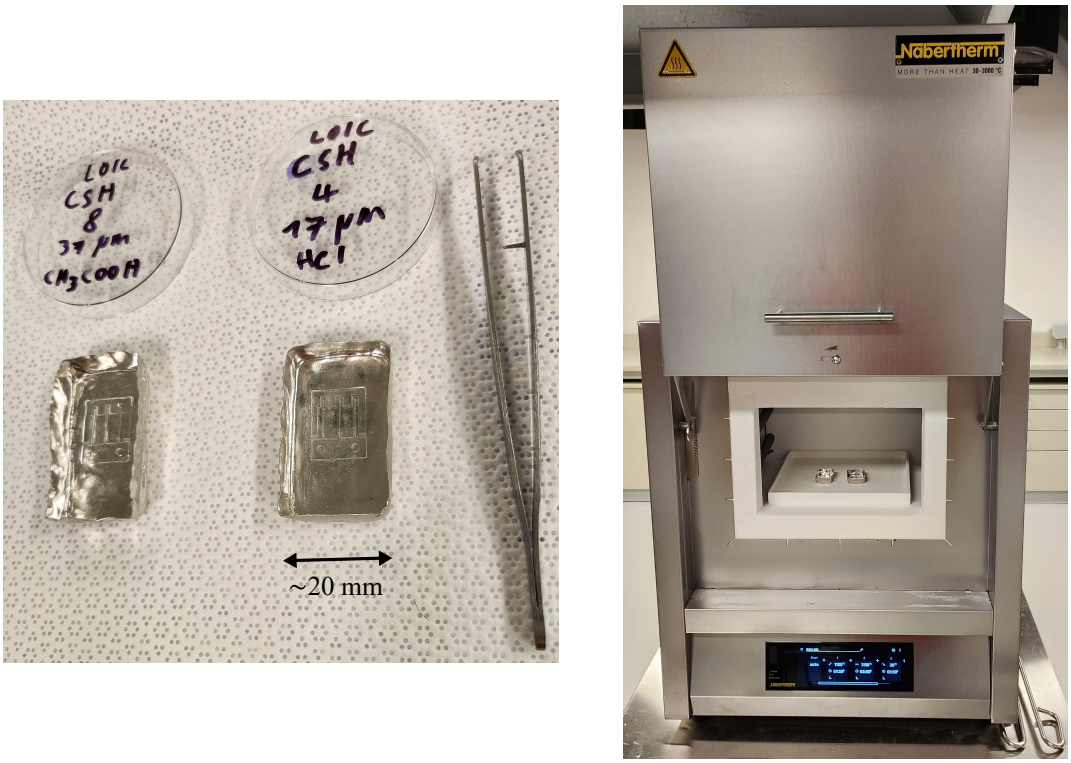

Figure 3.9: Annealing process. On the left, is a view of 2 samples cleaned in an acid bath and placed inside separated platinum annealing pots. On the right, the oven used for the annealing process.

Visual Results The first results were obtained following the same annealing step as in [89]. The temperature is increased with a ramp of 10 °C/min. Then, the temperature of 1200 °C is kept for 4 h for annealing the samples. This first test was performed without acid cleaning. Only a pure water cleaning was performed before the annealing. Figure 3.10 shows pictures of the annealed specimen. The complete monolithic structure was deformed. On the closed view of one of the cross-spring hinges, deformation is present along the length of one of the beams. Also, crystallization is present at different locations of the structure. To mitigate the deformation, the annealing step shall be shorter. It has then been performed during 3 h at different temperatures (figure 3.11). Crystallization is prevented by cleaning the specimens using HCl or CH_3COOH. It is explained by the fact that some impurities such as Alkalis are present at the surface of the fused silica substrate. Then, cristobalite can appear at temperatures above 800 °C [54]. Finally, it crystallizes during the cool-down. The test performed with the acid cleaning (figure 3.11) shows no more crystallization. The source of the impurities is probably the KOH etching step of the structure manufacturing.

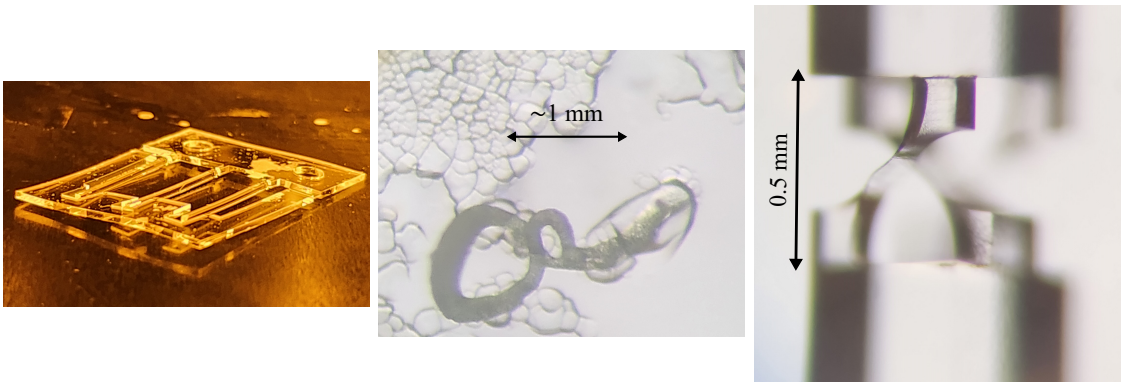

Figure 3.10: Annealing defects. On the left figure, the sample shape is deformed after the 4h annealing at 1200 °C. In the middle, crystallization appears at the surface of the sample. Also, it shows random holes passing through the thickness of the sample. On the right, a 7 µm beam is deformed after the 3h annealing at 1150 °C.

Figure 3.11 shows closeup views of a cross-hinge specimen after different annealing (3 h at 1100 °C, 3 h at 1150 °C and 4 h at 1200 °C). The visual effect of the annealing is perceptible after the 4 h annealing at 1200 °C. The edges of the specimen become rounded. The mechanical effect of the different annealing experiments is tested in the next section along with non-annealed specimens. An experiment is used to estimate the bending strength of the fused silica material at the micro-scale. As glass is a brittle material, its strength is influenced by micro-cracks at its surface. Then, by annealing, it can mitigate the crack concentration.

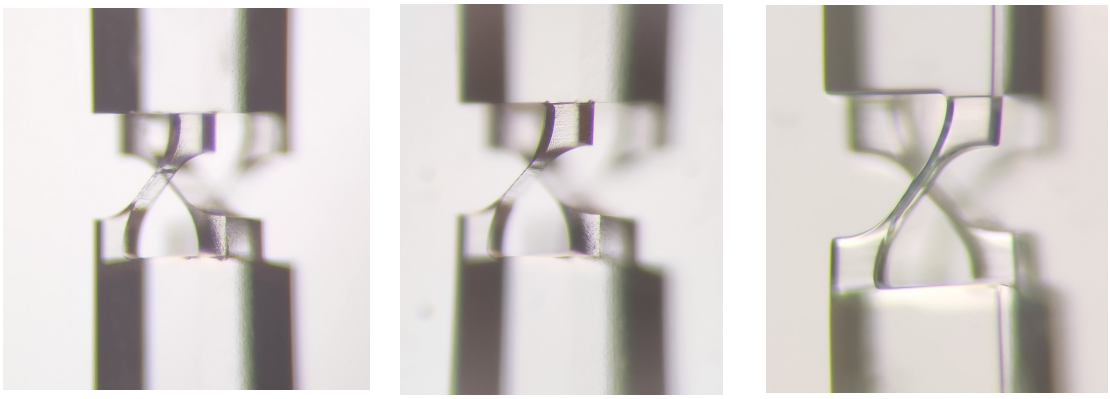

Figure 3.11: Annealed samples. From the left to the right: 17 µm, 7 µm and 26 µm thickness cross-spring hinge samples annealed respectively 3h at 1100 °C, 3h at 1150 °C and 4h at 1200 °C.

3.2 Material Properties: Experimental Analysis of The Bending Strength and Damping Characteristics

Fused silica is best known for its use in optics due to its transparent properties. This material has also a very high elastic range that can be defined as its elastic limit (> 1GPa) to Young modulus (72 GPa) ratio. This ratio is the largest among other materials such as Steel, Titanium or Copper-Beryllium. With its elastic modulus being in the same range as those materials, fused silica can replace them for the design of compliant mechanisms. Being a brittle material, its use was limited due to the machining complexity in the past. Nowadays, 3D structure manufacturing is possible by femtosecond laser-assisted wet etching [7]. Various compliant mechanisms have been obtained using this technique [9, 50, 62]. Thanks to its bio-compatibility, fused silica is also used to design surgical tools [94, 81]. We have demonstrated that thanks to the versatility of femtosecond laser machining, it is possible to include strain sensors in fused silica compliant mechanisms during their manufacturing [84, 1]. In this work, the elastic range of fused silica for micro-scale compliant mechanisms is studied. Estimations of the bending strength are presented for different flexure specimens. The results are compared to the previously reported value of 2.7 GPa [8]. Then, the damping characteristics of the fused silica flexure specimens are studied for their potential use as resonators.

Fused silica, with its high-temperature stability and low-damping behaviour, is also a well-suited material for precision sensors. The operating range of a sensor based on an oscillator can be limited by thermal noise in the low-frequency domain [72]. Using low-damping materials, this noise is mainly dominated by gaseous thermal noise. Nevertheless, at low frequency and in a low vacuum environment, there is a dissipation occurring inside the material, called thermoelastic damping (TED). Each energy dissipation phenomenon can be included in one term called the quality factor or 'sharpness of resonance': $\frac{1}{Q} = \sum_i \frac{1}{Q_i}$. The smallest Q_i dominates. Fused silica's high-quality factor can differ according to its manufacturing method [63]. Two different experiments are built to extract this characteristic.

The flexure specimen geometries are presented in this work in the first section. Then, the bending strength experiment is described and the results are listed for two different types of flexure elements. In the next section, the quality factor model and experiment are shown for two different scales of resonators based on micro-scale fused silica flexure hinges. Finally, the results are discussed and further approaches are proposed.

3.2.1 Flexure Specimens

Flexure elements are compliant joints for monolithic mechanisms. Their degrees of freedom are defined by their geometry. A structure can be considered as a flexure element when its thickness is at least ten times smaller than its other dimensions. Then, as this joint is

monolithic, it acts like a spring in its degrees of freedom. Therefore, the bending range of such a joint is limited by the bending strength of the material. As fused silica is a brittle material, its bending strength is limited by its surface quality. It depends on the probability of cracks in the structure. So, it explains why the typical bending strength of fused silica is about 50 MPa on the datasheets but can be considered above 1 GPa for micro-scale structures. The two structures tested in this work are described in Fig. 3.12. The circular notch (Fig. 3.12 a) is a 3 DoF joint with a stable rotation centre but a limited bending range due to stress concentration. (Fig. 3.12 b) The free cross-spring hinge is a 1 DoF joint which can have the low stiffness of a leaf spring[79]. The parallel leaf spring joint (Fig. 3.12 c) is a 2 DoF joint used as the hinge of the pendulum for the vacuum experiment in Section IV B.

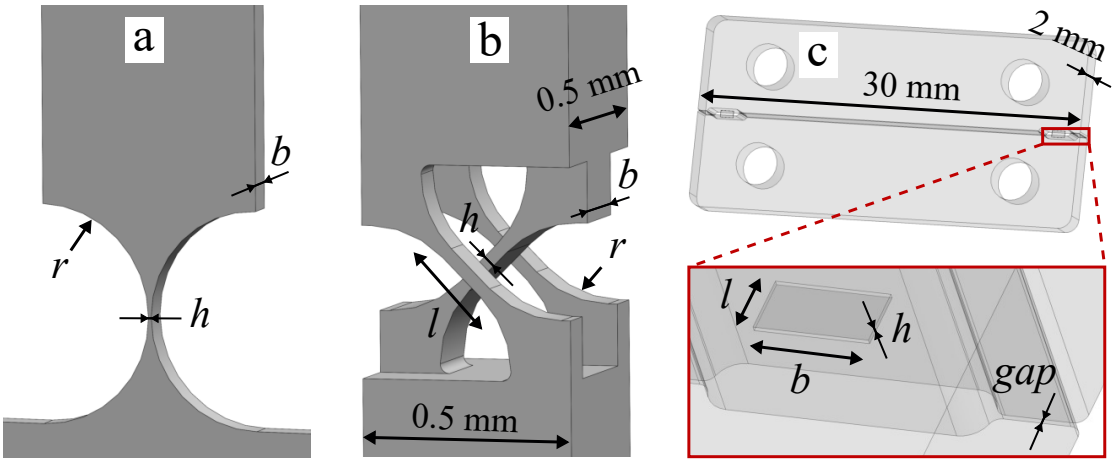

Figure 3.12: The flexure specimens. **a** The circular notch of width $b = 500$ µm, with its radius $r = 2$ mm and its central thickness h between 25 µm and 55 µm. **b** The free cross-spring inspired from [79] of total beam width of $2b = 400$ µm, beam length $l = 300$ µm, beam thickness h between 8 µm and 37 µm and with a stress relaxation radius at the extremities of the beam $r = 260$ µm. **c** The parallel leaf-spring hinge joint is designed to hang a pendulum oscillating proof mass. Each leaf spring beam has a width $b = 1$ mm, a length $l = 500$ µm and a thickness $h = 50$ µm. These beams are located in the central thickness of the 2 mm thick monolithic part. A 50 µm gap is etched along the width of this joint to limit the rotation range of the joint.

3.2.2 Bending Strength Estimation

To estimate the bending strength, the flexure specimens are fixed on a 2 DoF translation platform (Fig. 3.13 d). A rigid pin (a screw or a resistor leg) can push at the free extremity of the rigid body attached to the flexure specimen. A camera placed on top is recording the bending. The specimen is bent until it breaks. Then, the image of the camera just before the rupture of the specimen is extracted. The maximum bending angle can be measured on this image (Fig. 3.14).

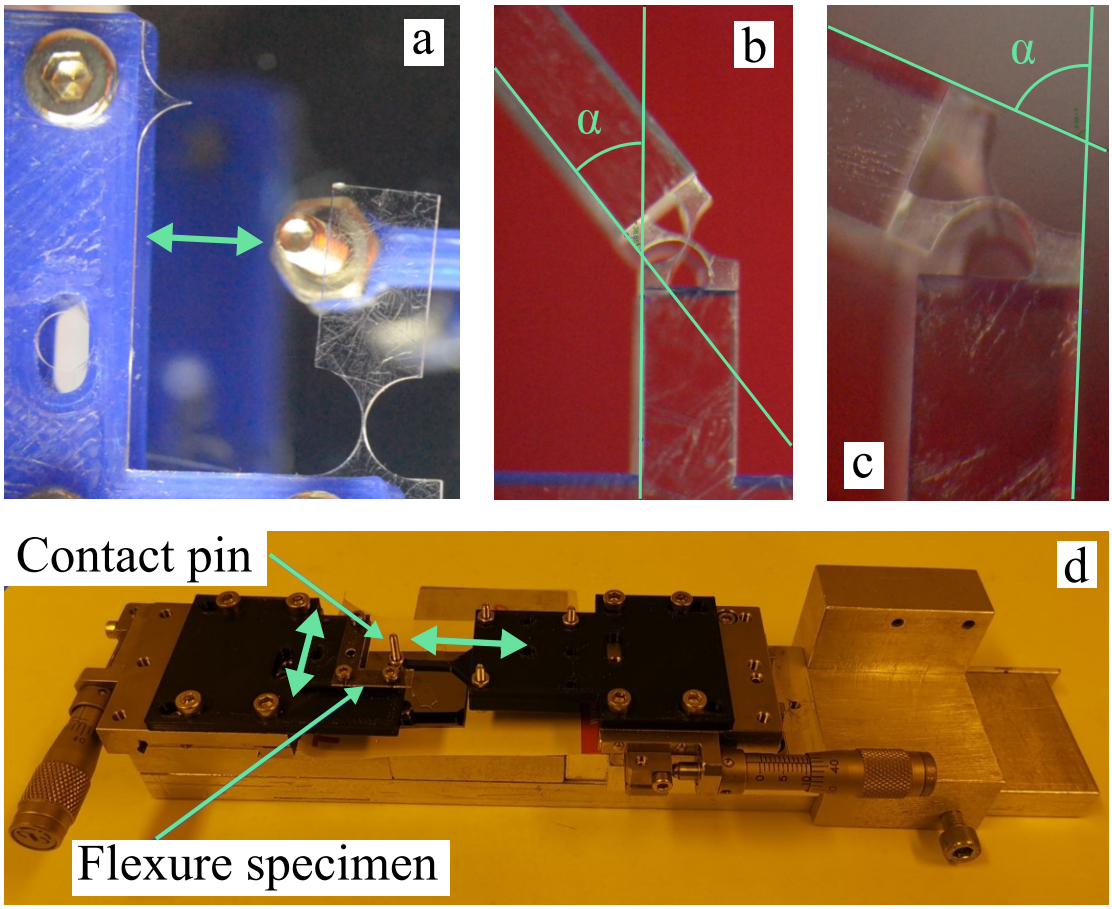

Figure 3.13: The experiment to estimate the bending strength of fused silica at the micro-scale (8 µm to 55 µm flexure thickness). **a** The circular notch bent by pulling the rigid part at its free end with a screw mounted on a manual translation stage. **b** The free cross-spring bent at its maximal bending angle before the first beam breaks. **c** The free cross-spring bent at its maximum bending angle before the last remaining beam breaks. **d** The test bench used to bend the flexure specimens.

Circular Notch Hinge Bending

From the stiffness of the circular notch and the measured maximum bending angle $\alpha_{\max}$, the maximum bending stress in the specimen can be expressed as[37]:

$$\sigma_{\max} = \frac{4E\alpha_{\max}\sqrt{h}}{3\pi\sqrt{r}} \tag{3.1}$$

with E, Young's modulus of fused silica (72 GPa), h, the central thickness of the circular notch and r, the central radius of the circular notch.

Triple Beam Cross-Hinge Bending

The free cross-spring hinge has three beams. Due to the manufacturing technique etching aspect ratio, the thickness of the beams varies. A compensation in the design has not been performed. So, the middle beam is thicker and breaks before the other ones. To perform the estimation on a simplified model, the bending angle $\alpha_{\max}$ before the last beam breaks is considered. The maximal stress located at the surfaces of the beam can be expressed as:

$$\sigma_{\max} = \frac{E\alpha_{\max}h}{2l} \tag{3.2}$$

with h, the thickness of the beams of the cross-hinge and l, their length.

Results

The results of the bending experiments are reported in Fig. 3.14. The estimated maximal bending stress varies from 1.3 GPa to 2.7 GPa for the free cross-hinge specimens and from 1.1 GPa to 2.3 GPa for the circular notch specimens. This experiment consolidates the results obtained in [8]. It also shows that this limit is not dependent on the thickness of the specimen in the studied range (8 µm to 55 µm).

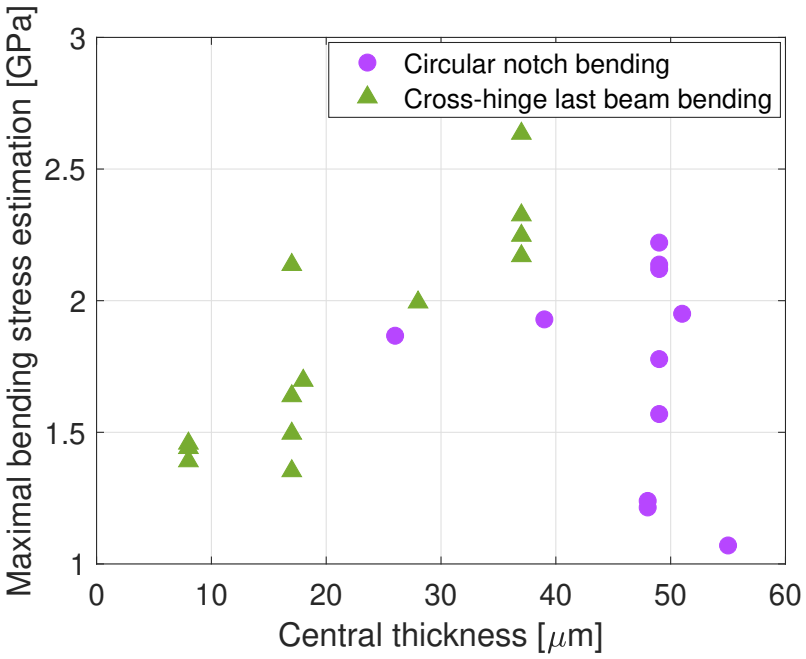

Figure 3.14: The maximal bending stress of the element is estimated from their maximum bending angle before rupture. The bending test is performed on the circular notch and cross-spring specimens described in figure 3.12.

In addition to the figure 3.14, the figure 3.15 contains the results of the bending test performed

on the annealed cross-spring specimens described in the previous section (figure 3.11). These results show no improvement in the bending strength of these specimens by the selected annealing processes. The estimation of the maximal bending stress of one specimen annealed 4h at 1200 °C was even lower than 1 GPa. It is probably due to the unforeseen deformation of the specimen as shown in figure 3.10.

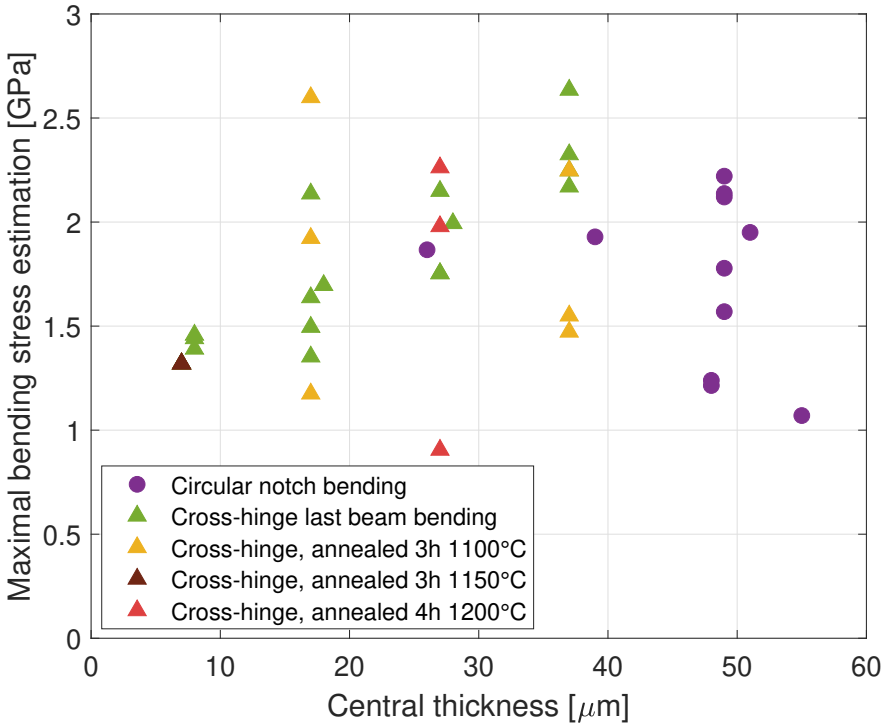

Figure 3.15: The maximal bending stress of the element is estimated from their maximum bending angle before rupture. The bending test is performed on the circular notch and cross-spring specimens described in figure 3.12. This figure contains the results of the figure 3.14 and bending test from annealed cross-spring specimens.

The bending strength of fused silica, being a brittle material, cannot be defined precisely. Nevertheless, the probability of failure for a given stress can be estimated, it is called the Weibull distribution [88]:

$$P = 1 - e^{-(\frac{\sigma}{\sigma_N})^m} \tag{3.3}$$

with σ, the maximal bending stress estimation and σ_N and m, the fitting parameters extracted in figure 3.16. From the obtained distribution, the bending strength of fused silica can be selected for the design of compliant mechanisms. With a considered bending strength of 1 GPa, the probability of failure is less than 5 %.

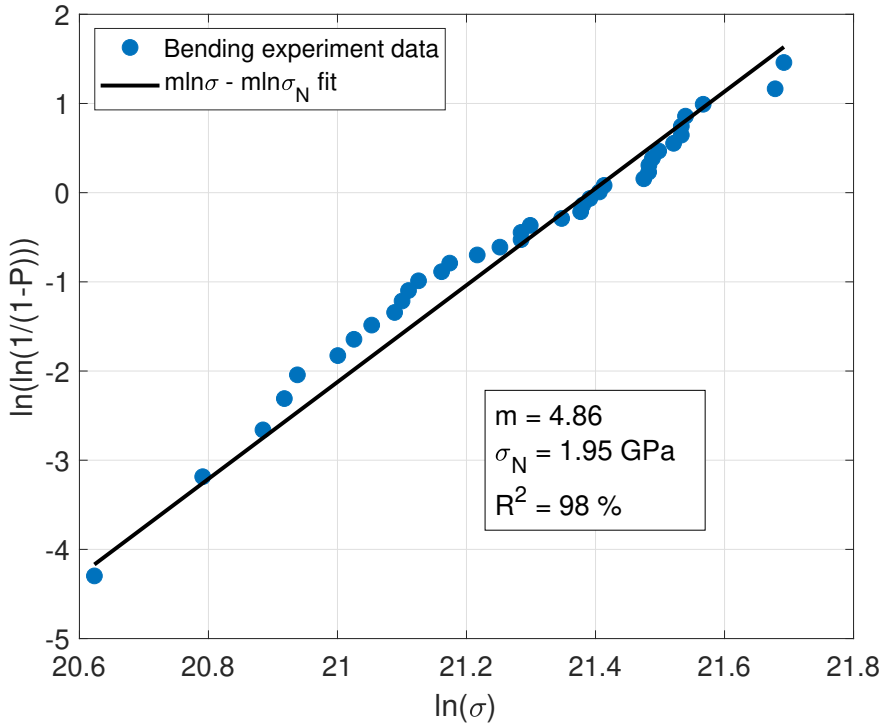

Figure 3.16: Linearization of the probability of fused silica failure according to the estimated maximum bending stress from the data of the bending experiments. The data is fitted with the least squares method using the Weibull distribution.

3.2.3 Damping Quality Factor Estimation

Fused silica being a low-damping material, it is necessary to analyze the oscillation energy dissipation under vacuum. At ambient pressure, the dissipation is governed by the gaseous damping. To model the dissipation, there are two regimes to consider: at high pressure, the gas acts in a viscous regime. At lower pressure, the air is rarefied. The air molecules are less likely to hit each other. Only the collision between the oscillator and the molecules can be considered. By evaluating the momentum transfer rate from a rectangular-shape vibrating beam to the surrounding gas due to the collisions between the beam and the gas molecules, the pressure-dependant quality factor can be expressed as [23, 14]:

$$Q_{\text{molecular}} = \frac{\rho_b t \omega_0}{4} \sqrt{\frac{\pi}{2}} \sqrt{\frac{RT}{M_{\text{air}}}} \frac{1}{p} \tag{3.4}$$

with ρ_b, the density of the material, t, the thickness of the pendulum, ω_0, its natural resonance frequency, R, the gas constant, M_{air}, the molecular mass of the gas and p, the gas pressure. If the oscillator is close to walls though, another approach has to be considered [6].
For the viscous regime, the quality factor can be described using fluid mechanics. Considering

that the viscosity is constant and the air is not compressed, the Navier-Stockes equation and the continuity equation for an incompressible fluid can be used. The problem cannot be solved analytically. By using a model which considers the oscillator as a string of spheres, with a diameter equal to the width of the oscillator, Hosaka et al. [39] propose a direct evaluation of the quality factor:

$$Q_{\text{viscous}} = \frac{2\rho_{\text{b}} t w^2 \omega_0}{6\pi\mu w + \frac{3}{2}\pi w^2 \sqrt{2\mu \frac{M_{\text{air}}}{RT}\omega_0 p}} \tag{3.5}$$

with w, the characteristic length of the oscillator (for example, its length) and μ, the dynamic viscosity of the gas. The limit between the two regimes can be separated using the Knusden number [14]: $Kn = \frac{\lambda}{w}$, with λ, the mean free path of gas molecules and w, the width of the gas layer in motion. The free molecule regime is considered when $Kn > 10$. The viscous regime is considered when $Kn < 0.1$. In between, there is a transition regime where both phenomena have influence.
Other than the gas damping, an energy dissipation can occur through the clamping. Vibration waves are propagating through the clamping and are damped in their way before coming back. It means that an amount of the vibrational energy is dissipated through the clamp. The quality factor can be expressed as the clamped-free model in [34]:

$$Q_{\text{c}} = \gamma_0 \frac{L}{t} \tag{3.6}$$

with γ_0, a vibration mode material dependant constant, L, the length of the oscillator and t, the thickness of its flexure hinge joint. This phenomenon is not reported in this work as it occurs multiple orders of magnitude above the other quality factor models.
The quality factor dependent on the material describes its thermoelastic damping (TED). It describes the heat flow dissipation due to internal friction inside the material. It can be expressed as[51]:

$$Q_{\text{TED}}^{-1} = \frac{E\alpha_{\text{T}}^2 T}{C_{\text{p}}\rho_{\text{b}}}\left[\frac{6}{\xi^2} - \frac{6}{\xi^3}\frac{\sinh(\xi)+\sin(\xi)}{\cosh(\xi)+\cos(\xi)}\right] \tag{3.7}$$

$$\xi = w\sqrt{\frac{\rho_{\text{b}} C_{\text{p}} \omega_0}{2k}} \tag{3.8}$$

with α_{T}, the coefficient of thermal expansion, C_{p}, the specific heat, w, the width of the flexure hinge joint and k, the thermal conductivity.

Ring-Down Experiment - Cross-Hinge

The quality factor is estimated through ring-down experiments. The test bench is represented in Fig. 3.17. The oscillators composed of a free cross-hinge specimen as its flexure joint are

placed inside a small vacuum chamber. A rigid pin located on a 3 DoF translational platform inside the vacuum tank that can be controlled manually from outside is used to bend the oscillator and release it. A glass window is located on top of the tank (in the centre of Fig. 3.17). A camera is placed on top of this window to record the oscillation. The amplitude of the oscillation is then obtained by image recognition of the trace of the oscillator as in Fig. 3.17 b.

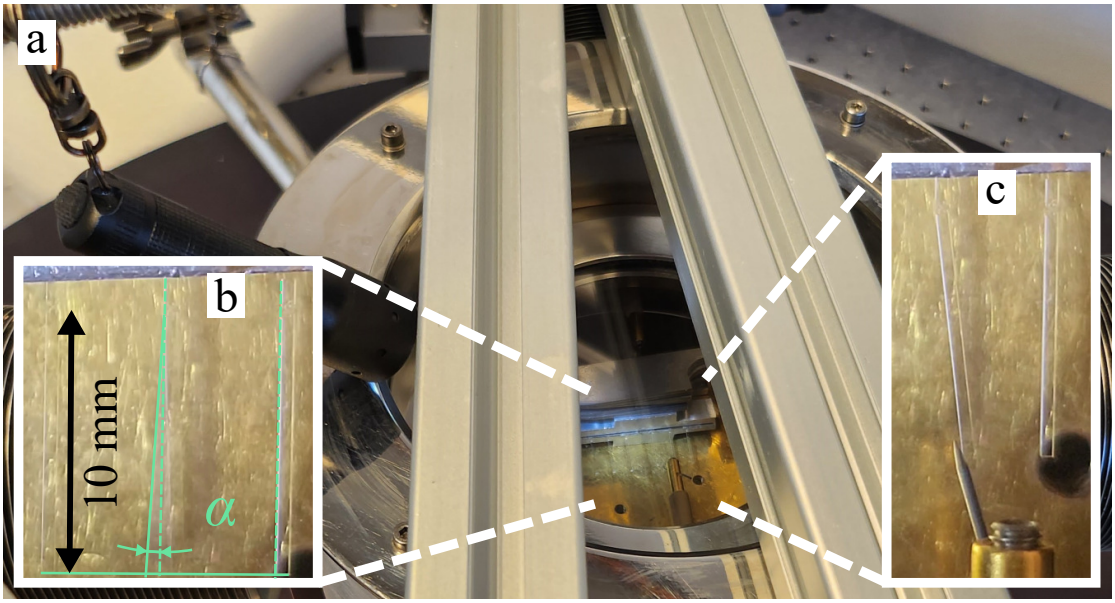

Figure 3.17: The test bench to perform the ring-down experiments on the cross-hinge-based oscillators. **a** The vacuum tank with a transparent window at the top, a flashlight on the side to highlight the sides of the glass structure and two Aluminum profiles used as a mount for the camera. **b** The image seen by the camera which is used to extract the bending amplitude of the resonators of length $L = 10$ mm. **c** The translational pin used to apply the starting amplitude to the resonators which are controlled manually from outside the vacuum chamber.

The oscillation damping can be quantified by taking an exponential fit of the envelope of the oscillation amplitude in the time domain. The amplitude is described as $A = A_0 e^{-\alpha t}$, with t, the time, A_0, the amplitude at $t = 0$ and α, the attenuation factor. It is obtained using the Matlab function "fit" with the fit type set as "exp1". The quality factor is then estimated as:

$$Q = \frac{\omega_0}{2\alpha} \tag{3.9}$$

with ω_0, the natural resonance frequency of the cross-hinge and α, the attenuation factor of the oscillation extracted from the ring-down experiment as detailed in Fig. 3.18.

$$\omega_0 = \sqrt{\frac{K_{\theta M}}{I}} \tag{3.10}$$

with $K_{\theta M} = \frac{Ebh^3}{6l}$, the rotational stiffness of the beams of the cross-hinge and I, the inertia of

the oscillator, which can be described as a thin beam attached to the cross-hinge:

$$I = \frac{mL^2}{12} + mr_{\text{CoG}}^2 \tag{3.11}$$

with m, the mass of the 500 µm side squared oscillator of length L and r_{CoG}, the distance between its Centre of Gravity and the centre of the cross-hinge. The obtained resonance frequency $f_0 = \frac{w_0}{2\pi}$ has been verified experimentally. A vibrometer has been placed instead of the camera. The resonance frequency has been then extracted by recognition of the resonator cyclic pattern period.

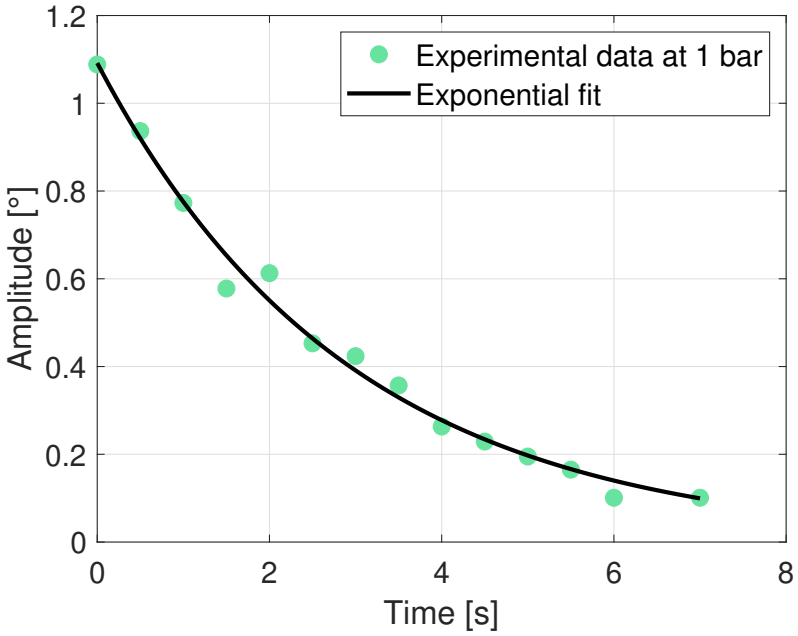

Figure 3.18: The bending amplitude of the resonators. Each green point in the graph corresponds to the maximal amplitude of the trace of the beam extracted from a picture as in Fig. 3.17 b. The exponential fit is expressed as $A = 1.09e^{-0.34t}$.

Ring-Down Experiment - Pendulum

Ring-down experiments are also performed on a larger pendulum. An Aluminium proof mass is suspended using the parallel leaf spring fused silica flexure joint described in Fig. 3.12. This pendulum is placed inside a larger vacuum tank (Fig. 3.19). There is a transparent window located on top of the vacuum tank. A vibrometer OFV 500 from Polytec is used to record the oscillation of the pendulum. The laser head is placed outside from the tank on top of the window facing a mirror. The mirror reflecting the laser is placed at 45° from the laser head and at 45° from the pendulum (Fig. 3.19 c).

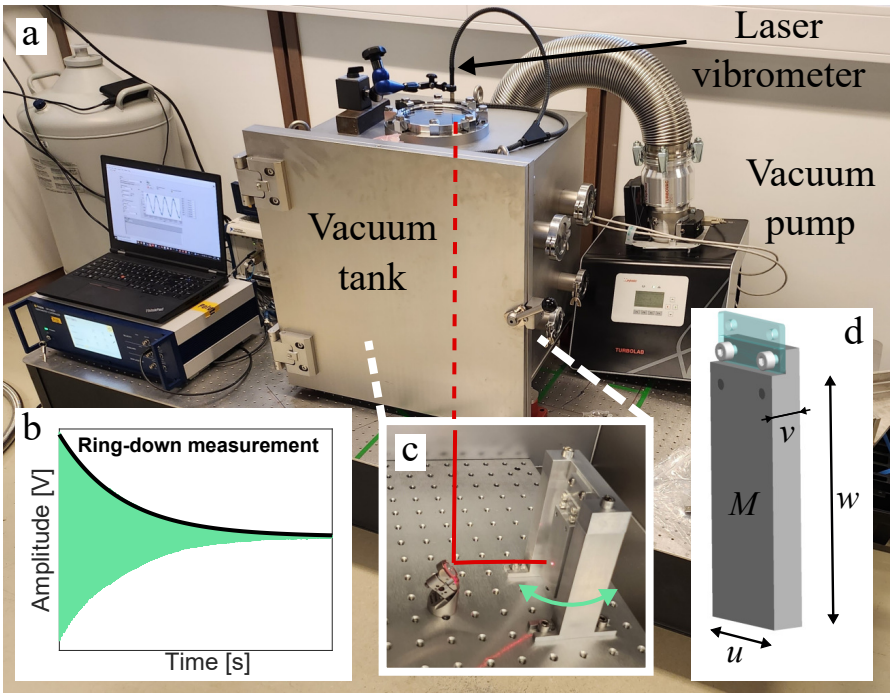

Figure 3.19: The test bench to perform the ring-down experiments on the parallel leaf spring-based pendulum. **a** The test bench is composed of a vacuum tank, a vibrometer and the data acquisition system (DAQ). **b** A representation of the amplitude time measurement of the pendulum recorded with the vibrometer. **c** The pendulum is located inside the vacuum tank facing the 45° mirror. **d** The pendulum geometry of width $u = 30$ mm, length $w = 82$ mm, thickness $v = 10$ mm and of mass $M = \rho_{Al} u v w$.

The quality factor can be extracted by performing an exponential fit on the envelope of the amplitude signal recorded with the vibrometer.

$$Q = \frac{\omega_0}{2\alpha} \tag{3.12}$$

with ω_0, the natural resonance frequency of the pendulum extracted from the ring-down vibrometer oscillation amplitude signal and α, the attenuation factor of the oscillation extracted from the ring-down experiment.

Results

The quality factor extracted from both experiments is reported in Fig. 3.20. The quality factor data of the cross-hinge-based resonators compare with the model. Unfortunately, it was not possible to decrease the pressure in the small tank below 2×10^{-3} mbar. So, this experiment is not sufficient to quantify the thermoelastic noise described by the slope tending to saturation at low pressure. The maximal Q-factor obtained at $p = 2 \times 10^{-3}$ mbar is $Q = 1.85 \times 10^5$. Regarding the leaf spring-based pendulum experiment, there is an unexpected saturation at $Q = 2.5 \times 10^4$.

The dissipation source is probably not explained by clamping dissipation as it faces almost the same conditions as the other experiment. A hypothesis is that the load applied to the small flexure joint induces stress that may influence the internal friction in the leaf springs. However, the contrary is reported explaining that applying tensile stress leads to a decrease of the thermoelastic damping[41, 46, 85]. Then, other approaches need to be investigated. The asymmetry of the manufactured part or its surface quality under tensile stress may lead to dissipation. Or friction at the fused silica-aluminium boundary may occur.

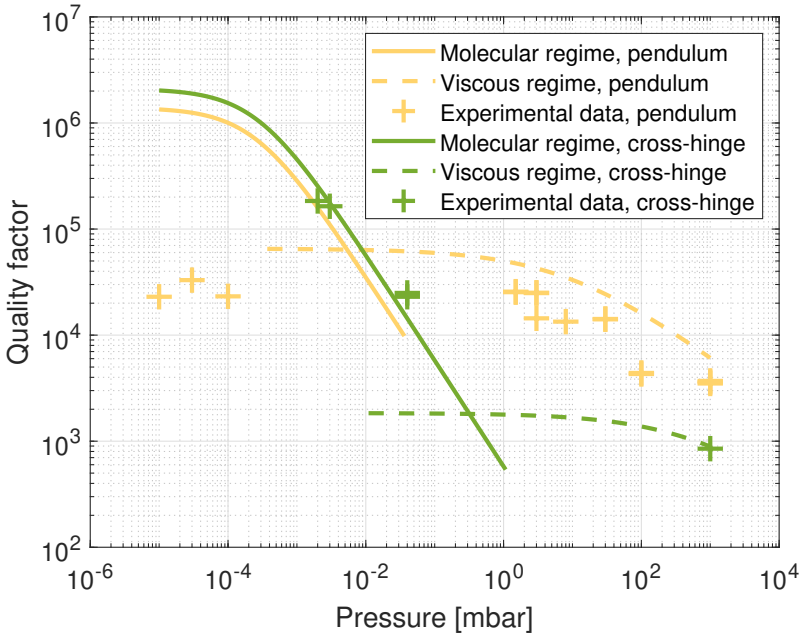

Figure 3.20: The estimations of the quality factor obtained through the ring-down experiments at different pressures. In green, the model and data correspond to the cross-hinge-based resonators. In yellow, are the model and data corresponding to the parallel leaf springs-based pendulum.

3.2.4 Conclusion

This work consolidates the design rule that 1 GPa bending strength can be considered for fused silica micro-scale structures. Continuing with bending strength, a study reported that annealing the fused silica part machined through femtosecond laser-assisted wet etching increases their compressive strength[89]. Our experimental method can be used to investigate if annealing has a significant impact on bending strength. However, as depicted in figure 3.15, our bending test on annealed specimens did not show any improvement in the bending strength of fused silica structures manufactured by femtosecond laser-assisted etching. The annealing process was not deeply studied though. A further experimental study would be beneficial. A theoretical analysis of such specimens' annealing would also be valuable. To assess the dynamic properties of fused silica, the damping characteristics have been investigated for

two different configurations. The quality factor of the free cross-hinge-based fully monolithic fused silica resonators is not limited by thermoelastic damping at pressures above 2×10^{-3} mbar. An improvement on the setup is necessary to perform ring-down experiments at lower pressures. The quality factor of the parallel leaf spring-based loaded pendulum saturates at $Q = 2.5 \times 10^4$ below 1 mbar. A deeper study is required to explain this dissipation. An investigation of whether annealing the fused silica flexure specimens has an influence or not on their damping characteristics is planned.

4 Flexure Mechanisms

This chapter describes the conception of vertical inertial sensor mechanisms. It focuses on the various flexure mechanisms featuring the sensors, their manufacturing and integration. Section 4.1 mainly discusses the mirror translational guiding of a vertical inertial sensor for high-resolution quantum gravimeter hybridizing. Part of this study has been published along with the work of Anthony Amorosi at the ISMA Conference in 2022 [2]. Section 4.2 presents an experimental study to optimize the design of an astatic leaf spring suspension mechanism for vertical inertial sensors. It has been used to design the vertical inertial sensors used for the active isolated platform of the E-TEST experiment (Einstein Telescope EMR Site & Technology) [73, 74].

4.1 Design Optimization of a 1 Degree of Freedom Translational Oscillator for a Low-Frequency Vertical Inertial Sensor

Our laboratory, the Precision Mechatronics Laboratory, is currently developing a low-frequency inertial sensor. For this laboratory, the low-frequency domain is considered in the 1 Hz order and below. It will be used for the active isolation of an Absolute Quantum Gravimeter. This section focuses on conceiving the guiding mechanism of this sensor's oscillator.
Atomic Quantum Gravimeters (AQG) are ultra-stable absolute gravity sensors [15, 33, 65]. They can detect changes in gravitational acceleration caused by subsurface structures, such as caves, or density anomalies, providing valuable information for geological surveys. They also can be used to monitor changes in groundwater levels or magma movements beneath volcanoes. Their performance is mainly limited by seismic motion [15, 33, 65]. In addition to this noise source, atomic interferometers suffer from dead times and a small bandwidth due to their discrete functioning. Dead times refers to periods where the instrument is not collecting data. It occurs between each measurement interval, during the setup and initialization phases, and automatic calibration periods. Several solutions have been suggested to mitigate these problems:

- Employing combinations of active/passive vibration isolation for the gravimeter sensor

head [32, 97].
- Implementing real-time vibration compensation at the sensor output [57, 56].
- Hybridizing the sensor to enhance its performance [49, 22].

Merging a vertical inertial sensor such as a classical accelerometer with a gravimeter can mitigate dead times and the noise level induced by ground vibrations. So, their resolution can be improved depending on the accelerometer resolution. The solution is mainly addressed by adapting existing vertical inertial sensors such as the Vertical INertial Sensor (VINS) [29] to interface with an existing gravimeter. However, to investigate the limit of this kind of sensor for other uses in active isolation strategies, additional requirements are defined:

- Make it vacuum-compatible to mitigate the gaseous thermal noise.
- Fabricate the flexure guiding in fused silica to mitigate the thermoelastic noise.

Before getting into more details about the mechanical design of this sensor, the concept of active isolation is briefly introduced in 4.1.1. Then, the requirements of the inertial sensor are listed in 4.1.2. The guidance for the mirror of the interferometer is defined in 4.1.3. To maximize the operating range of this sensor, first, the geometric parameters are defined to limit the stiffness of the mechanism in 4.1.4, and then, they are selected such that the stiffness of the first spurious modes is maximized in 4.1.5. Finally, subsections detailing the design of the sensor and its performance are discussed in 4.1.6, 4.1.7 and 4.1.8.

4.1.1 Active Isolation

Some highly sensitive physical experiments require a high level of isolation. It means that the external source of vibrations impacts the experiment, and thus, needs to be mitigated. The basics of isolation are to put a large mass on a suspension. The model is illustrated on the left in black of figure 4.1. m represents the mass of the plant, x is the motion of the mass, w is the motion of the ground and F_a is an external force applied on the mass. The dynamics of the system can be described as:

$$m\ddot{x} + c(\dot{x} - \dot{w}) + k(x - w) = F_\mathrm{a} \tag{4.1}$$

with k, the spring constant of the suspension, and c, the damping coefficient of the suspension. Using the Laplace transform, the motion of the mass can be described by the transfer function:

$$X(s) = \frac{k + cs}{ms^2 + cs + k} W(s) + \frac{1}{ms^2 + cs + k} F_\mathrm{a}(s) \tag{4.2}$$

with $X(s)$, $W(s)$ and $F_\mathrm{a}(s)$, respectively the Laplace transforms of x, w and F_a. This transfer function can be separated into two parts. A part that represents the transfer function of the ground motion to the mass motion, is called transmissibility. The other represents the transfer

function of an external force on the mass to the mass motion, called compliance.

$$X(s) = T_{wx}W(s) + T_{fx}F_a(s) \tag{4.3}$$

with T_{wx} and T_{fx} representing respectively the transmissibility and the compliance. Their magnitude and phase are illustrated in figure 4.2. The black curve represents the transfer function of a mass on a spring. At low frequency, both the transmissibility and the compliance are equal to 0 dB which indicates there is no isolation of the mass. Then, there is a pole at $f = \frac{1}{2\pi}\sqrt{\frac{k}{m}}$ which is the natural resonance frequency of the mass on a spring. And after the pole, the curve is decreasing. That is the isolation property where $|T_{wx}(j\omega)| < 1$. As one can see in figure 4.2, the overshoot at the resonance frequency of the plant results in an amplification of the motion of the mass. If this pole is contained in the working range of the isolation plant, it needs to be damped. There are different passive and active strategies to implement this damping. An inertial sensor can be used to actively damp the plant by placing it on top of the mass. The signal of this sensor describing an estimation of x is used to control the motion of the mass x. The model of this system is shown in figure 4.1. The figure on the left represents the use of a perfect motion sensor. The figure on the right represents the use of an inertial sensor. The inertial sensor is also described as a mass on a spring. Its mass shall be very small compared to the mass of the plant. Its mass can also be used for damping but is not explored in this work.

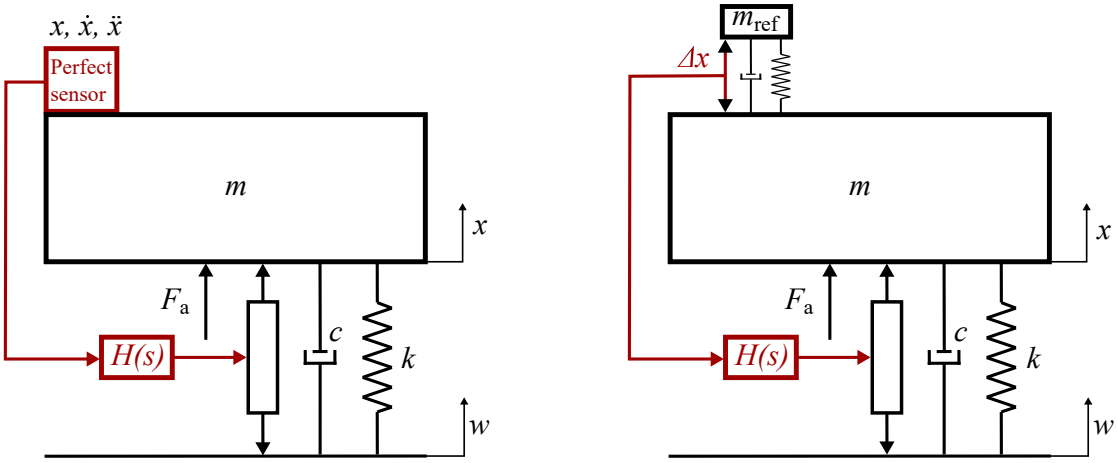

Figure 4.1: Principle of an active isolation plant with the sensor mounted on top of the plant considering a perfect sensor on the left, respectively an inertial sensor on the right.[26]

One way to damp the pole of the plant is to apply a PD controller on the isolator using the signal of the sensor. The transmissibility and compliance of the plant using this strategy are shown in figure 4.2. Considering an inertial sensor, you can see that the sensor's dynamics limit the plant's isolation. First, to minimize $|T_{wx}(j\omega)|$, the resonance frequency of the inertial sensor shall be as low as possible. Secondly, it is important to take into account the higher modes of motion of the sensor. They shall be higher than the working frequency range. Then,

damping is very limited or even not possible.

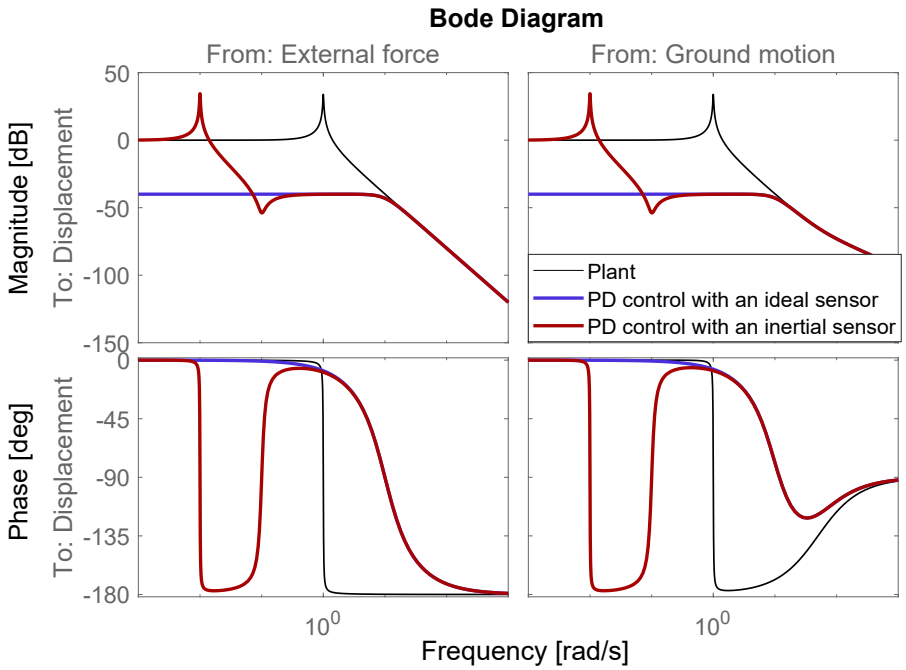

Figure 4.2: Transmissibility and compliance of an isolation plant with the reference on top like the one in figure 4.1.

4.1.2 Inertial sensor requirements and concept

The prototype that we are developing shall be able to operate from 10 mHz to 100 Hz and respect a $10 \times 10 \times 10$ cm^3 footprint. First, we have decided to use a long-range Michelson interferometer readout to allow for reaching the highest possible resolution. Inertial sensors based on interferometric readout currently offer better performance than conventional seismometers with electromagnetic readout. Sub-picometer resolutions have been achieved using Michelson interferometric readings of the proof-mass motion of inertial sensors [98, 28, 35, 24]. Also, as recommended by the lessons learned, linear guidance should be designed to allow the use of a flat mirror. Previously, corner cubes were used but some additional non-linearities appear. Then, the inertial mass compliant mechanism shall be optimised such as the principal resonance frequency is minimized while the spurious resonances staying above 100 Hz. Our current mechanical design (figure 4.3) is based on the linear encoder-based inertial sensor [36], replacing the encoder on the linear guidance by the moving mirror of the interferometer. This design is stiff enough in the transverse motion direction while allowing the use of the available space to minimize the stiffness of the oscillator.

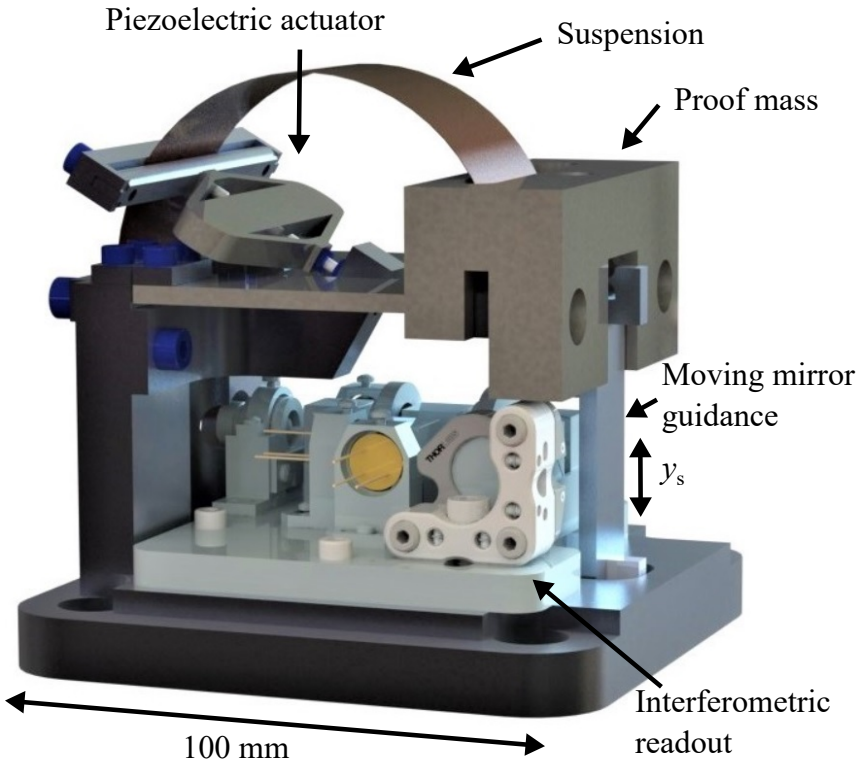

Figure 4.3: First version of the low frequency vertical inertial sensor prototype featuring a piezoelectric stack actuator and a custom long-range Michelson interferometer, $10 \times 10 \times 10$ cm^3

4.1.3 Linear Guidance System

Since the seismic motion is measured using a moving flat mirror, translational guidance is required to ensure the reflection of the laser beam on the same axis in the interferometer. Figure 4.4 shows the mechanics of the proposed inertial sensor. The mirror (8) is placed at the output stage of a parallel four-bar linkage (the rigid part between (2) and (4)). The mass M is linked to the fixed frame by one hinge joint, the (1), in parallel to (5), the compensation mechanism. Having no joint in series but in parallel maximizes the spurious resonance frequencies. (Each flexible joint can be considered a perfect joint with a spring. It is called the pseudo-rigid-body model [40]. So, when joints are placed in parallel, their stiffness is summed. And then, when they are placed in series, the inverse of their stiffness, their compliance, is summed.) Flexure hinges (2-4) are circular notch hinges. These joints serve only as guides for the mirror. Therefore, they do not have to support a significant mass. Thus, the flexure hinge types are selected based on their manufacturability and their centre of rotation drift. Henein describes the usual flexures in [37]. Introducing a 3D glass monolithic micro-flexure, Tielen and Bellouard compared their cross-spring pivot hinge with the other usual flexure hinge types [79]. It was found that the circular notch has the lowest centre of rotation drift, which is even negligible. Therefore, the circular notch hinge is the best choice for limiting the non-linearities.

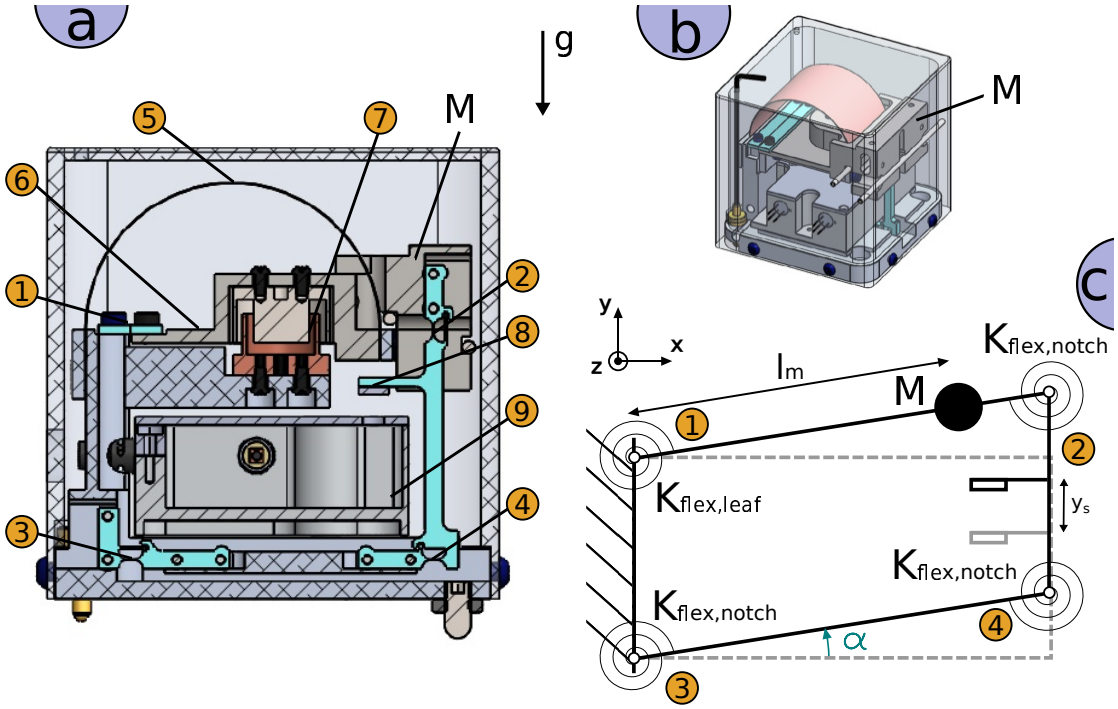

Figure 4.4: The flexure joints are labelled with enumeration (1-6). (a) Fused silica joints are highlighted in cyan blue. (b) Trimetric view of the sensor construction. It consists of a leaf-spring hinge (1) linking the inertial mass M to the frame and 3 circular notch hinges (2-4) transferring the inertial mass motion to the mirror in translation. The mirror (8) is located between (2) and (4). (6) is the thin part of the inertial mass. (c) $K_{\text{flex,leaf}}$ and $K_{\text{flex, notch}}$ are the bending stiffnesses of the hinge joints of the translational guide. α is the angle of rotation of the inertial mass M with l_{m} its radius of gyration. The inertial mass is suspended horizontally by a Beryllium Copper bent leaf spring (5). The inertial sensor contains a voice-coil actuator (7) and an interferometric readout (9)

Their geometry is chosen according to the manufacturing constraints to limit their stiffness. Concerning the flexure hinge (1), there are two functions to consider: the rotational guidance and the prestress to compensate for the gravity to maintain the proof mass horizontally. In the linear encoder-based inertial sensor of [36], the suspension mechanism for the inertial mass consists of applying a prestress in the flexure hinge (1). Since we will primarily use fused silica for the flexures, applying a prestress is difficult or insufficient (However, it is possible [4],[61]). As it has been widely used for low-frequency inertial sensors, we decided to use leaf-sping (5) to suspend the inertial mass M. E. Whielandt explains that the astatic leaf-spring suspension was invented for this purpose [91]. It combines a small overall size with a long free period. Finally, the flexure hinge (1) of our current design is a two-part cantilever beam (figures 3.7,4.9 and 4.11c). This flexure is easy to manufacture, can withstand large deflection and can be very thin. This allows us to make it wider to stiffen the mechanism in the transverse motion direction of the DoF.

Considering the kinematic scheme in figure 4.4, to maximize the resolution of the sensor, the

length of the bar between (1) and (2) must be maximized. To limit the principal resonance frequency, the radius of gyration must be maximized. The mirror displacement measures the motion of the inertial mass. This mirror is placed on the rigid body between the joints (2) and (4). Indeed, the mirror displacement is proportional to this distance:

$$y_s = d_{1-2} * \sin\alpha \tag{4.4}$$

($\sin\alpha \approx \alpha$ for small displacements). Then, to limit stress in joints, the suspension leaf spring shall be attached as close as possible to the centre of mass of the inertial mass.

4.1.4 Minimization of the resonance frequency for the 1st mode of motion

The resonance frequency is characterized by the stiffness of the link to the ground of the inertial mass and by its inertia. Its stiffness K_{equ} can be obtained as follows (4.5):

$$K_{equ} = K_{flex,leaf} + 3K_{flex,notch} + K_{suspension} \tag{4.5}$$

$K_{flex,leaf} = K_{flex,notch}$ is chosen to keep the symmetry of the parallelogram table guidance. $K_{suspension}$ is neglected since an advanced model is required to characterize it. Also, the proof mass is considered at the horizontal equilibrium. It will be studied experimentally in the next section. Note that to amplify the inertia, the position of the centre of mass, l_m, should be maximized. It will also allow a longer leaf-spring astatic suspension, and then, increase its free period. Thus:

$$K_{equ} = 4K_{flex,notch} \tag{4.6}$$

The principal resonance frequency is then:

$$f_0 = \frac{1}{2\pi}\sqrt{\frac{K_{equ}}{I_z}} \tag{4.7}$$

considering $I_z = Ml_m^2$:

$$f_0 = \frac{1}{2\pi}\sqrt{\frac{4K_{flex,notch}}{Ml_m^2}} \tag{4.8}$$

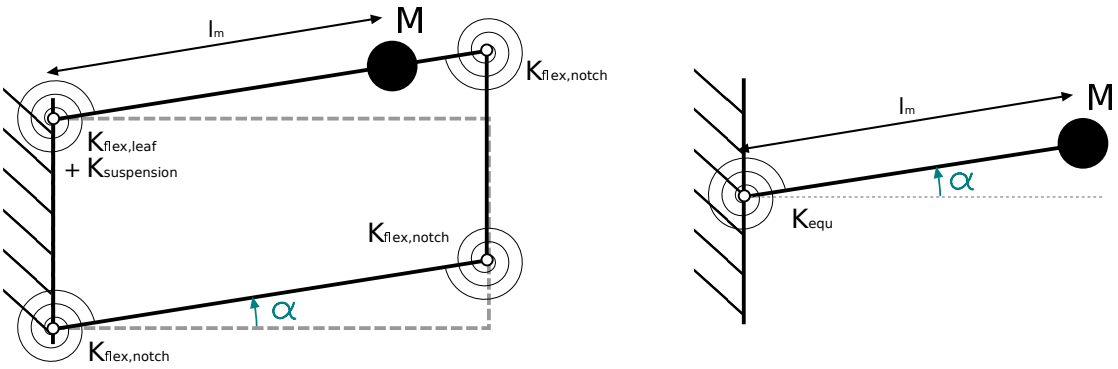

Figure 4.5: 2D Kinematic scheme of the sensor in the principal mode of motion

Figure 4.6 shows the design of the circular notch hinges. An approximation of its stiffness can be obtained as described in [37]:

$$K_{\text{lex,notch}} \simeq \frac{2Ebe^{2.5}}{9\pi\sqrt{R}} = 21.8 \text{ mNm} \tag{4.9}$$

with its thickness $e = 100$ µm, its width $b = 4$ mm, its radius $R = 8$ mm and the Young's modulus of glass $E = 68.9$ GPa. Lower thickness can be obtained with the femtosecond laser-assisted etching process, to 10 µm. However, it is very fragile. The chosen thickness, $e = 100$ µm is a compromise between small thickness and handling easiness.

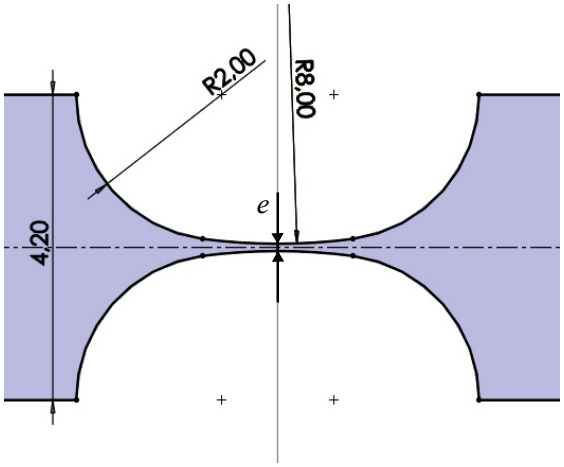

Figure 4.6: Circular notch design, thickness $e = 100$ µm

Figure 4.13 shows the geometry of the inertial mass, $M = 221.5$ g. Since its resonance frequency shall be minimized to limit thermal noise in the low-frequency domain, the inertial mass has been maximized regarding the available space. Its position, $l_1 = 48.3$ mm, has also been maximized. It is built out of stainless steel. This material is dense and can be provided easily.

Those properties allow us to obtain the principal resonance frequency of the oscillator:

$$f_0 = \frac{1}{2\pi}\sqrt{\frac{4K_{\text{flex,notch}}}{Ml_{\text{m}}^2}} = 2 \text{ Hz} \tag{4.10}$$

Regarding figure 4.2, it can be shown that the isolation capabilities below the resonance frequency of the inertial sensor are limited. According to the working range expected of the inertial sensor, from 10 mHz to 100 Hz, its oscillator resonance frequency is high. So, a stiffness mitigation strategy is required.

Other stiffness mitigation strategies

- Compliance can be added by decreasing the size of the rigid bodies. This strategy has not been selected because it will also lower the spurious resonances of the mechanism. This is not allowed because it would limit the working range of the sensor.
- There exist some examples as in [16] where negative stiffness is applied in the compliant mechanism. This strategy is complex as it would give instability to the system. Therefore, it has not been selected.
- Exceeding the geometry allows an increase in the inertia of the inertial mass, and thus, lowers its principal resonance frequency. However, the space available is limited.
- Active damping of the inertial mass can flatten the response of the inertial sensor. It is then possible to use it at a wider frequency range in the low frequencies. This strategy is currently under study. The actuation noise shall be investigated. If the spurious noise injected by the actuator is too important, it could significantly lower the resolution.

A prototype has been mounted to investigate the active damping of the inertial mass and the assembly of the glass flexure hinge (figure 4.7). A piezoelectric stack actuator is installed against the suspension leaf-spring (figure 4.7a). There is only one flexure hinge to simplify the testing (figure 4.7b). The flexure hinge (figure 4.7b) contains a stopper. It is screwed to the static structure and it is screwed and clamped to the inertial mass (figure 4.7c). The flat beam on the right end side of the sensor (figure 4.7a) is used for motion sensing.

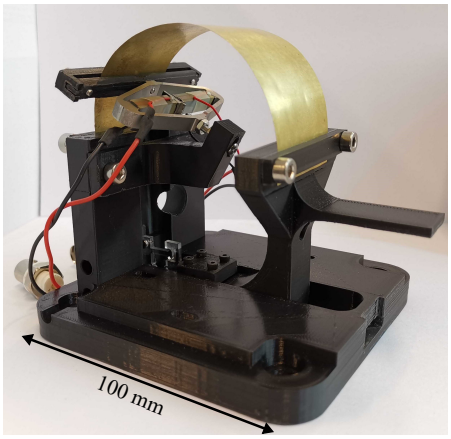

(a) Overall prototype

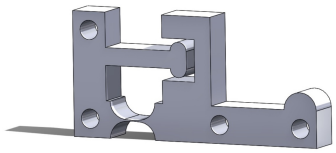

(b) Circular notch flexure hinge design

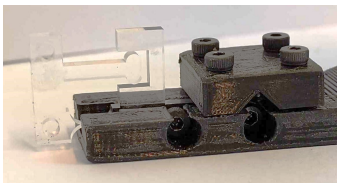

(c) Flexure hinge assembly

Figure 4.7: Prototype for active damping and glass flexure hinge assembly testing

4.1.5 Maximization of the operating range

The working range of the inertial sensor is limited by its spurious resonances above the principal resonance frequency. The placement and geometry of the joints can be optimized to stiffen the mechanism except in its principal DoF. The sensor's kinematic (figure 4.4) shows that the critical joint is the (1). Indeed, that joint links directly the inertial mass to the structure of the sensor.

Method

First, a glass monolithic simple design is defined to simplify the calculations (figure 4.8). The structure of the sensor on the left end side of figure 4.8 is fixed to the ground at its base.

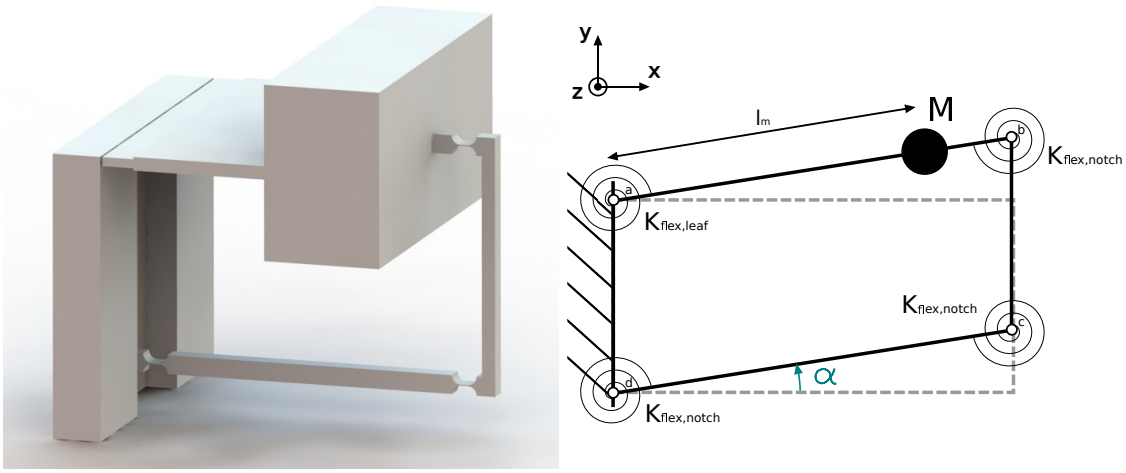

Figure 4.8: Inertial sensor simplified glass monolithic design

To optimize the critical joint, the parallel leaf spring hinge, the design of experiments method is used [59]. A three-factor factorial experiment involving the thickness of the two leaf springs, their length and the distance separating each other as inputs (figure 4.9). The output of the experiment is the first spurious resonance frequency after the principal resonance frequency. The principal resonance frequency is also computed to verify that the compliance of the mechanism has not been changed.

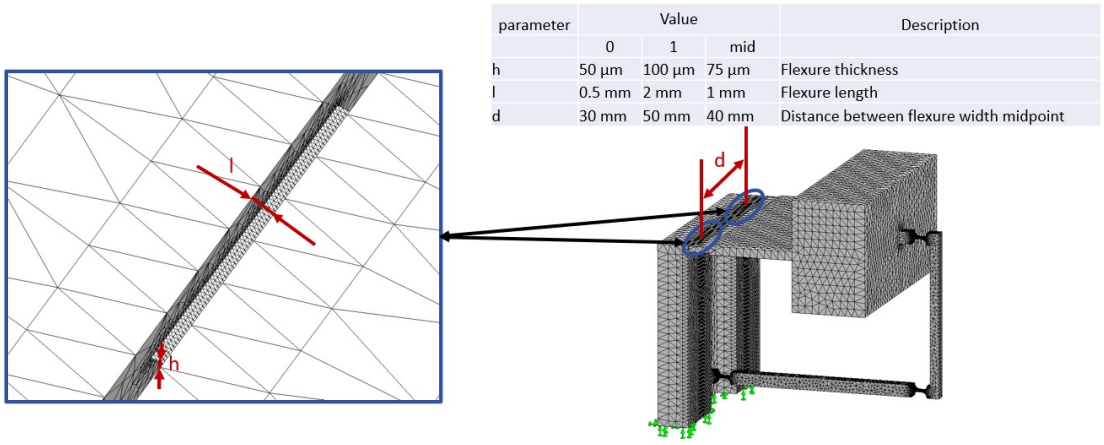

parameter	Value			Description
	0	1	mid	
h	50 µm	100 µm	75 µm	Flexure thickness
l	0.5 mm	2 mm	1 mm	Flexure length
d	30 mm	50 mm	40 mm	Distance between flexure width midpoint

Figure 4.9: Input parameters for the design of experiment

The width b of the flexure hinge depends on its thickness and its length. It is computed as follows knowing the fixed stiffness of the flexure hinge $K_{\text{flex,leaf}} = K_{\text{flex,notch}} = 21.8$ mNm:

$$I_z = \frac{b_{\text{tot}} h^3}{12} \tag{4.11}$$

$$K_{\text{flex,leaf}} = \frac{E I_z}{l} = \frac{E b_{\text{tot}} h^3}{12 l} \tag{4.12}$$

$$b = \frac{1}{2} b_{\text{tot}} = \frac{6 l K_{\text{flex,leaf}}}{E h^3} \tag{4.13}$$

The values are chosen as follows:

- The thickness: from 50 µm which is the lowest possible for manufacturing without significant complications. Then the maximum value is arbitrarily doubled.
- The length: 0.5 mm is the lowest possible for manual assembly without significant complications (if metal clamped leaf-springs are required). The maximum value is arbitrarily 2 mm.
- The distance between the flexure width midpoints: 30 mm is the minimum value where the two leaf springs join by their width in the centre (where the distance between their

internal edges is zero). 50 mm is the maximum value where the leaf springs external edges are located at the edges of the inertial mass for the widest case.

Table 4.1: List of experiments

Experiment	thickness [µm]	length [mm]	distance [mm]
000	50	0.5	30
001	50	0.5	50
010	50	2	30
011	50	2	50
100	100	0.5	30
101	100	0.5	50
110	100	2	30
111	100	2	50
Center	75	1	40

The experiments are in two parts. First, a numerical resolution is executed using the simulation toolbox of SolidWorks. Then, from the results of the simulation, an analytical model is identified. Finally, the results are compared between the numerical approach and the analytical approach.

Numerical approach A computer-aided design for each experiment is edited on SolidWorks. Then, a standard mesh is applied to the designs with $r = 2.5$ mm including mesh control with $r = 0.1$ mm on the flexure surfaces (figure 4.10). Finally, the frequency simulation study is applied.

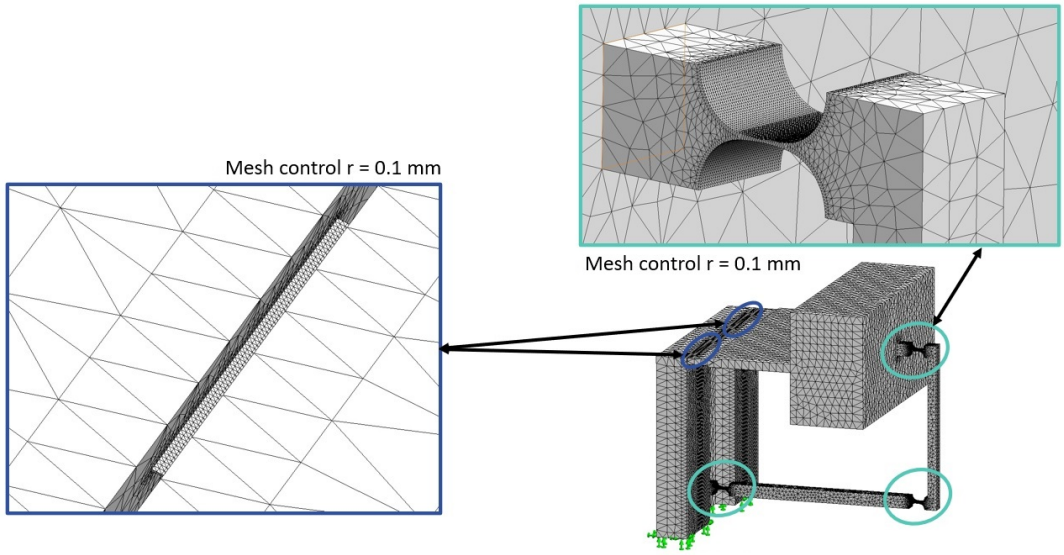

Figure 4.10: Mesh of the monolithic inertial sensor design

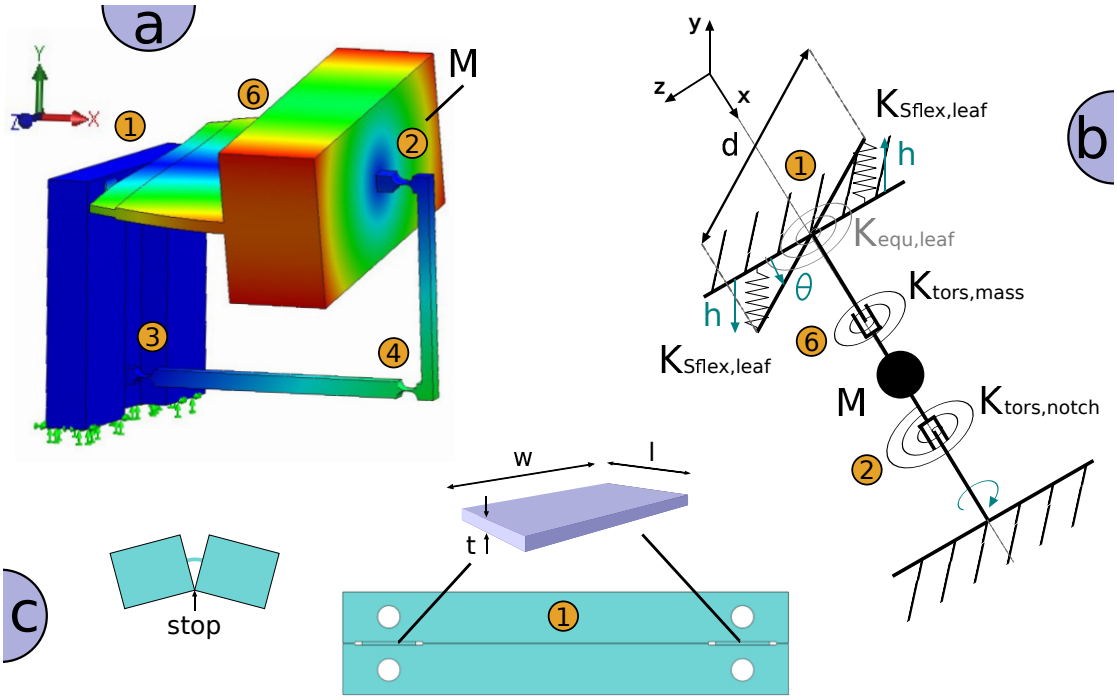

Figure 4.11: (a) The 1st spurious mode shape is studied using a simplified design of the mechanics. (c) The leaf-spring hinge joint (1) consists of 2 parallel leaf-springs of width w, length l and thickness t. The motion stops are included in its design. The geometry of these leaf springs is defined to maximize the 1st spurious resonance of the inertial mass. (b) The pseudo-rigid model of this mode is extracted. $K_{\text{Sflex, leaf}}$ is the double bending stiffness of the leaf-spring, $K_{\text{tors, mass}}$ is the torsional stiffness of the thin part of the inertial mass (6) and $K_{\text{tors, notch}}$ is the torsional stiffness of the circular notch (2). θ is the torsional angle of the inertial mass, h is the deflection of the leaf-springs and d is the distance between their centre.

Analytical approach Regarding the results of the numerical simulation, it appears that the first spurious mode is the torsion mode of the oscillator for every experiment (figure 4.11). Figure 4.11 shows that there is a nodal point on the top of the rigid body between (2) and (4) after the circular notch (2) next to the inertial mass. A simple analytical model can be identified. There are three compliant parts in this mechanism: the double bending of the leaf springs in opposition, the torsion of the flat part of the inertial mass and the torsion of the circular notch. Figure 4.12 shows that the double bending of the leaf-springs $K_{\text{Sflex,leaf}}$ with h deformation can be projected in $K_{\text{equ,leaf}}$ with a torsion θ:

$$\frac{1}{2}K_{\text{equ,leaf}}\theta^2 = 2\frac{1}{2}K_{\text{Sflex,leaf}}h^2 \tag{4.14}$$

considering $h = \frac{d}{2}\sin(\theta) \approx \frac{d}{2}\theta$:

$$K_{\text{equ,leaf}} = \frac{d^2}{2}K_{\text{Sflex,leaf}} \tag{4.15}$$

Then, there are two links between the mass M and the "ground" to consider to identify the stiffness in torsion of the inertial mass joint. The first link is composed of the compliance of the flat part of the proof mass and the leaf springs in series. The second link considers the compliance of the circular notch:

$$K_{\text{equ}} = \frac{K_{\text{equ,leaf}} K_{\text{tors,mass}}}{K_{\text{equ,leaf}} + K_{\text{tors,mass}}} + K_{\text{tors,notch}} \tag{4.16}$$

Then, the resonance frequency of the torsion mode is obtained as follows:

$$f_{\text{torsion}} = \frac{1}{2\pi} \sqrt{\frac{K_{\text{equ}}}{I_{\text{x}}}} \tag{4.17}$$

with I_{x} the inertia of the inertial mass in its torsion axis x:

$$I_{\text{x}} = \frac{1}{12}(w^2 + c_1^2)M_1 + \frac{1}{12}(w^2 + c_2^2)M_2 \tag{4.18}$$

considering the mass dimensions in figure 4.13.

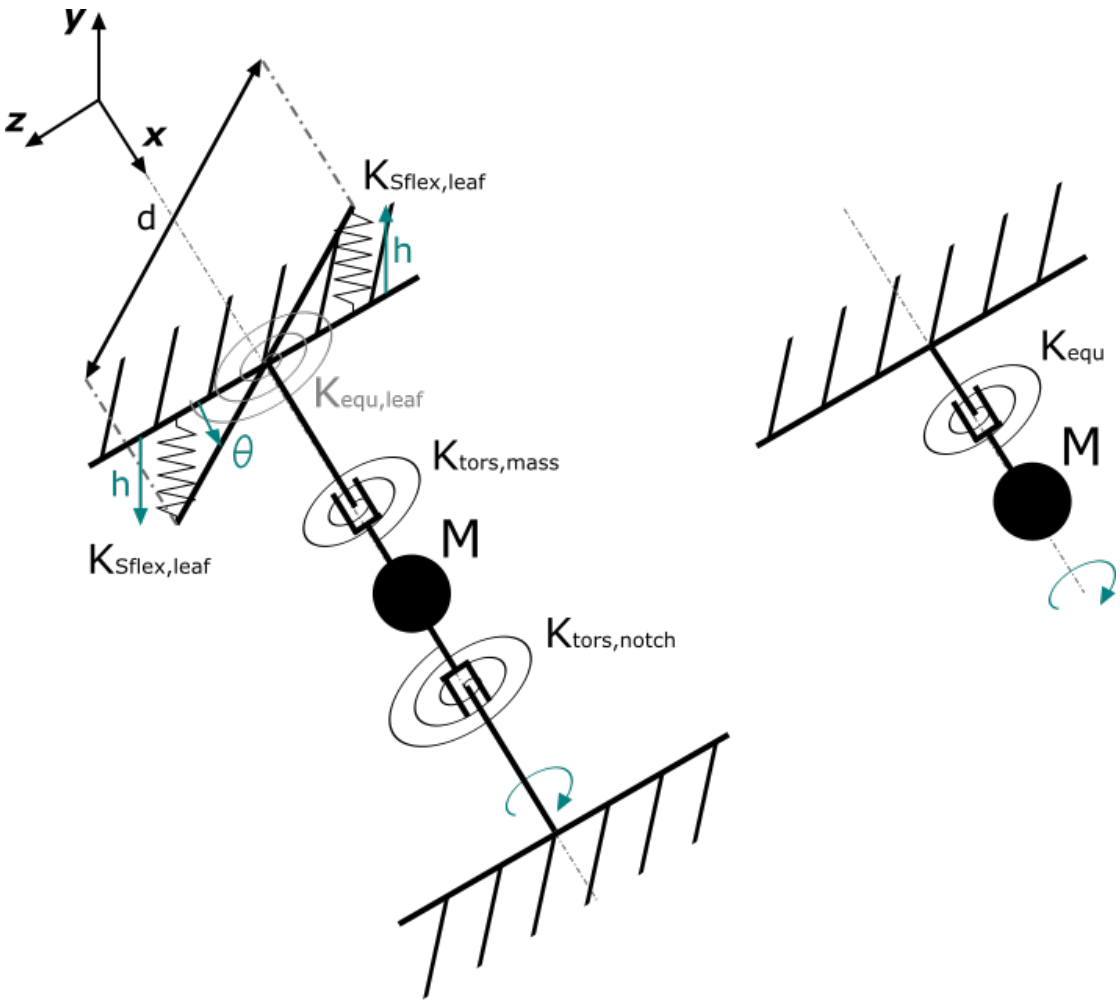

Figure 4.12: Torsion mode kinematic scheme

The different stiffness can be obtained as in [37]:

- The double bending stiffness of a leaf-spring:

$$K_{\text{Sflex,leaf}} = \frac{Ebh^3}{l^3} \tag{4.19}$$

  with its width b depending on its thickness h and its length l as described before.
- The torsion stiffness of the inertial mass:

$$K_{\text{tors,mass}} = \frac{Gwc_2^3}{3a_2} \tag{4.20}$$

  with the flat mass dimensions on figure 4.13 and the shear modulus of glass $G = \frac{E}{2(1+\nu)}$ with $\nu = 0.23$.

- The torsion stiffness of the circular notch:

$$K_{\text{tors,notch}} = 0.284 \frac{Gbe^{2.5}}{\sqrt{r}} \tag{4.21}$$

with the dimensions on figure 4.6 and its width b = 4 mm.

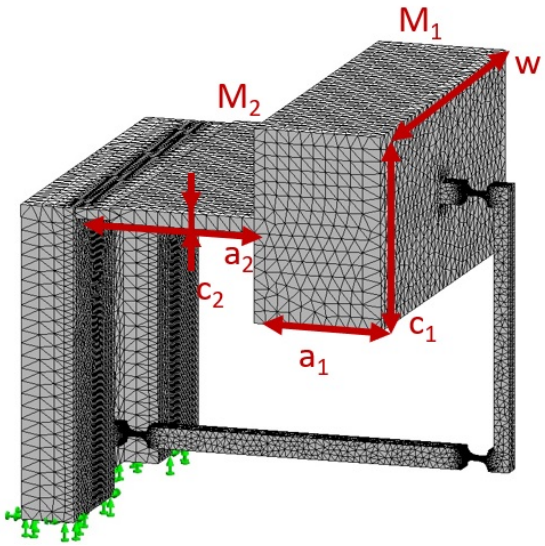

Figure 4.13: Inertial mass dimensions

Extended analytical approach To consider the double bending stiffness of the leaf springs in opposition to a height h as a torsion stiffness of an angle θ, an approximation has been made that the deformation of the leaf spring is constant along with its width. However, it is possible to compute the equivalent torsion stiffness considering the integration of double bent leaf springs of width dz:

$$K_{\text{equ,leaf}} = \frac{2K_{\text{Sflex,leaf}}}{b} \int_{\frac{d}{2}-\frac{b}{2}}^{\frac{d}{2}+\frac{b}{2}} z^2 dz \tag{4.22}$$

with the dimensions in figure 4.9.

Results

Figure 4.14 shows the results of the different approaches. The labels of the points correspond to the experiments listed in Table 4.1.

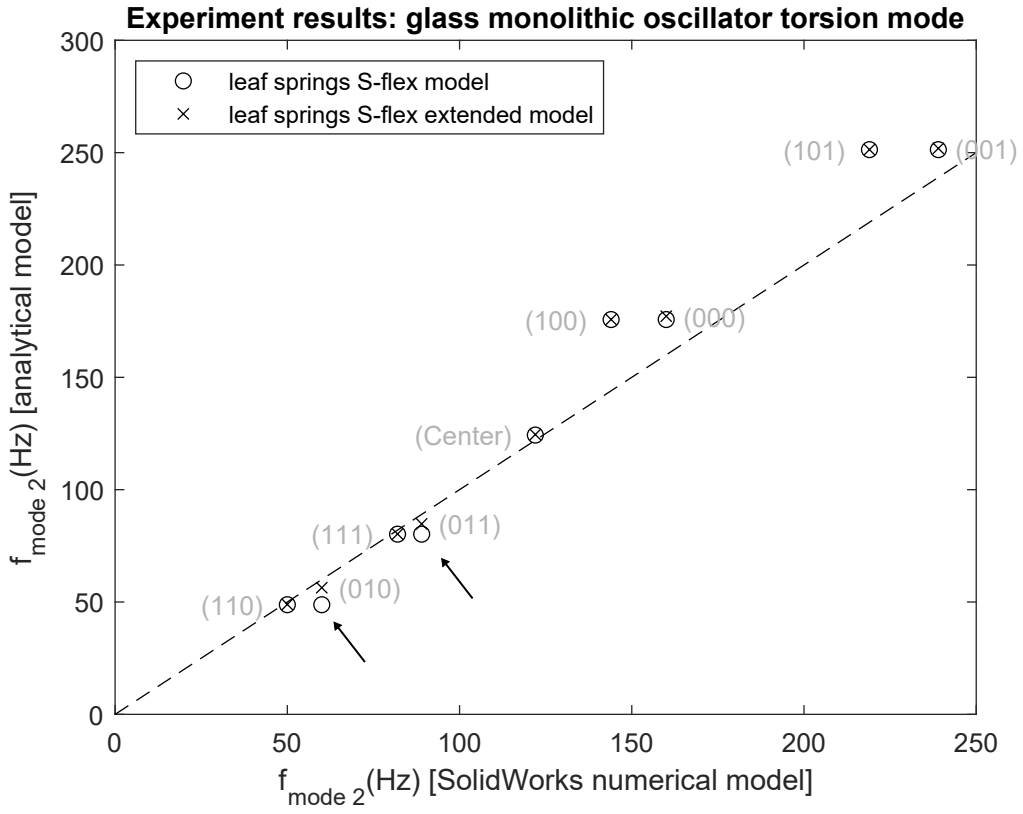

Figure 4.14: Comparison between the torsion mode results of the numerical approach and the analytical approach

The results of the analytical model are fairly close to the results of the numerical approach. The extended analytical does not improve the results for all experiments. The improvement is only significant for experiments (010) and (011). Those two experiments have the widest leaf-springs. Thus, it explains why it has a greater influence. So, for the others, the deformation of the leaf-springs can be considered as constant along their width. The results also show that the length of the leaf springs and their separation distance has a great influence while the thickness is less significant. Finally, taking into account the parameters of (001), a complementary study is performed using SolidWorks to verify that the spurious modes of the sensor are above 200 Hz (figure 4.15). Although the limit of the operating range is 100 Hz, a safety factor is considered to avoid the non-linear effects near the spurious modes. This experiment shows that the upper limit of the operating range of the sensor corresponds to the specification (spurious modes above 100 Hz). However, when using a 2 mm width mirror guide, the spurious mode at 169 Hz may affect the upper limit of the operating range.

4.1.6 Inertial Sensor Selected Design

The outputs of this analytical work can be used for the design of our inertial sensor. This sensor is named µVINS about the larger VINS (Vertical INertial Sensor) having the same type of suspension and interferometric readout. The geometry of experiment 001 has been chosen for the prototype design. It is also used for the design of the inertial sensor presented in section 4.2.2. Regarding the results, it can be seen that it can be further improved by lowering the length of the leaf springs, lowering their thickness and increasing the distance between them, but those parameters are limited by the manufacturing and the geometry. Also, that is not useful as the numerical simulation reveals the next spurious resonance frequency at $f_{\text{mode},3} = 246$ Hz for all experiments. That is an internal mode of guidance. Finally, the analytical model gives a good understanding of the torsion mode of the inertial mass.

Then, as a transition from the simplistic monolithic design to the real sensor design, various modal analyses are performed using SolidWorks. The results are listed in figure 4.15. Only the first 3 modes are kept since the operating range of the sensor will be limited by the first and the second modes. These are shown in the blue, red and orange squares on the right of the figure 4.15. The parameters of the analysis are the width of the mirror flexure guiding, the orientation of the flexure joint (2) and the proof mass. From the top to the bottom of the figure 4.15, the results depend on the width of the mirror guiding (respectively 2, 4 and 5 mm). From left to right: the original simplistic design based on the experiment 001 of the previous section; The mirror is added to the guiding; The proof mass is doubled and the flexure (2) is switched from its horizontal orientation to a vertical orientation; The simplistic model of the proof mass is replaced by the real design of the proof mass. From the modal analysis results of the figure 4.15, the 5 mm flexure width of the mirror guiding is selected. The 2 mm one reveals a mode lower than the 200 Hz safety margin. Also, a 5 mm width is selected instead of 4 mm because of the stock available at the laboratory. Then, it can be seen that the doubled simplistic mass cannot represent well the inertia of the real proof mass. The reason is the large difference in density. The simplistic design is made of fused silica but the real-proof mass is made of stainless steel. So, the inertia of the two bodies does not match.

The fused silica parts are manufactured by femtosecond laser-assisted etching. The flexible structures for the mirror guide and the leaf-spring hinge joint are machined from a 5 mm and a 2 mm thick fused silica substrate, respectively (figure 4.16c,d). The assembly of the inertial mass and its hinge joint is performed using a 6D-compliant mounting platform to reduce the stress in the flexure hinge (figure 4.16b). Figure 4.16a shows the fully assembled µVINS mechanics. To interface this sensor with an interferometric readout, a flat mirror is glued to the output stage of the translation guide (figure 4.16d).

Concerning the actuation selected for the force feedback strategy, the testing of the prototype

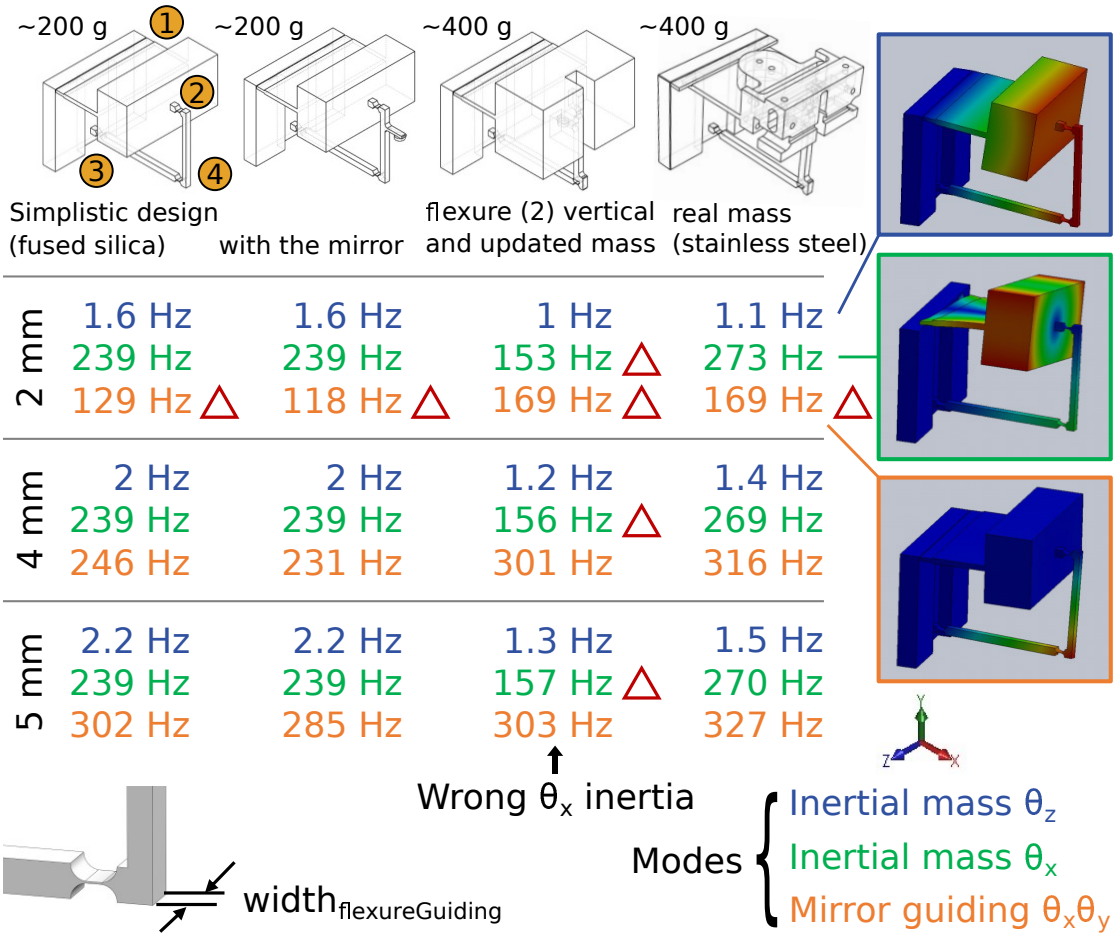

Figure 4.15: The design of inertial sensor mechanics is simplified to allow a rapid modal analysis of a monolithic fused silica design. (1-4) represents the flexure hinge of the mechanism. The modal analysis is performed using SolidWorks. The first parameter is the width of the mirror flexure guiding. The resonance frequency of the 3 first modes is estimated. Then, the analysis is performed with different complexifications of the design: first with the mirror; then, with doubling the mass and changing the orientation of the hinge (2); finally, replacing the mass block with the design of real inertial mass made of stainless steel. The red triangles indicate that the frequency is lower than 200 Hz.

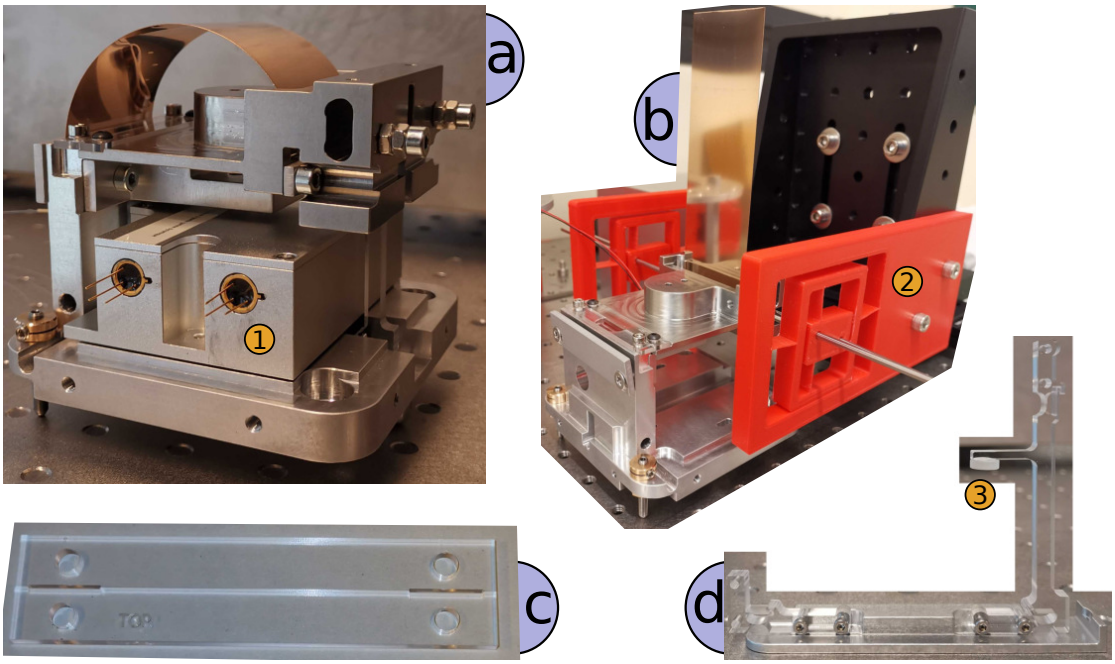

Figure 4.16: (a) The inertial sensor is mounted with an interferometric readout (1). (b) A 6D-compliant custom mounting platform (2) is used to assemble the inertial mass M to the frame with its fused silica leaf-spring hinge joint (c). (d) The mirror guiding is pre-assembled and slid below the inertial mass with the interferometric readout. The flat mirror (3) is glued to its translational guiding.

of figure 4.7a revealed that the piezoelectric actuator fixed to the leaf spring suspension was not sufficient to obtain the desired sensor sensibility at low frequency. We decided to use a voice-coil actuator (VCA) instead (figure 4.4a). The magnet is fixed to the proof mass and the coil is fixed to the frame of the inertial sensor. The VCA is placed as close as possible to the centre of mass of the proof mass.

It can be seen in figure 4.16a that it contains the custom interferometer (1). However, it arrived late in the project. For the testing of our prototype, we have used an Eddy current sensor instead. For that purpose, a Copper foil has been glued to a 3D printed plastic mount fixed to the mirror guiding (figure 4.17). Then, the Eddy current sensor can be placed vertically facing the copper foil. So, the displacement of the mirror can be recorded without using the interferometer (figure 4.18). A red plastic dummy interferometer is still integrated into the inertial sensor to validate the mounting procedure.

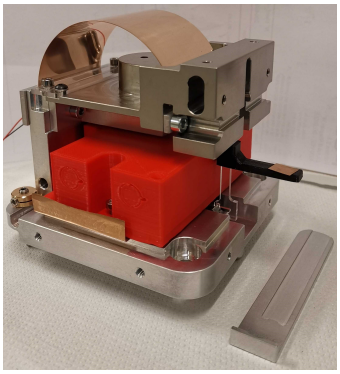

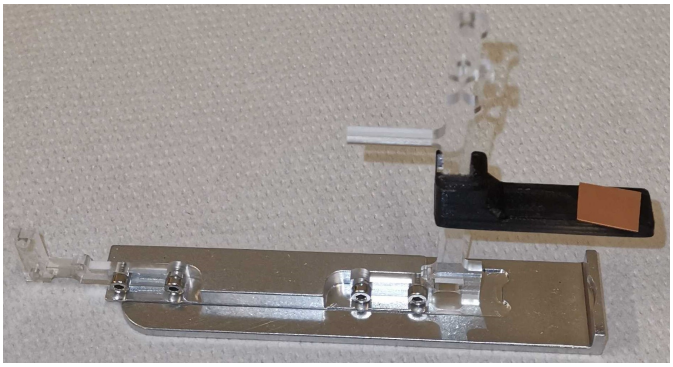

Figure 4.17: On the left, is the compact vertical inertial sensor containing a red dummy interferometer to validate the mounting procedure. On the right, the fused silica flexure mirror guidance before it is mounted on the sensor mechanism. A plastic part containing a Copper-Beryllium sheet is mounted on the mirror guiding as an interface to an Eddy-current sensor.

A ringdown experiment is performed in an open-air environment. The quality factor of the sensor (2800) and its resonant frequency (2.8 Hz) are determined [2].

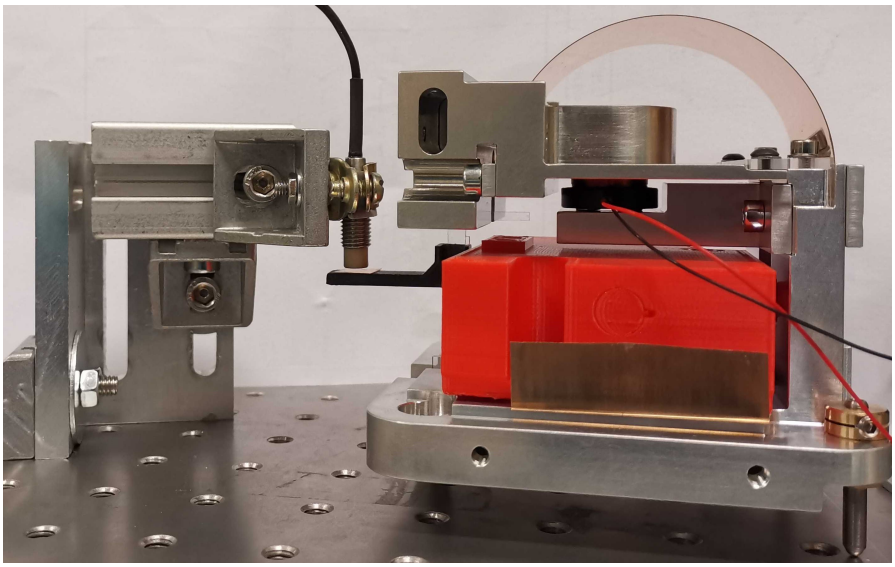

Figure 4.18: The compact vertical inertial sensor open-air configuration includes an Eddy-current sensor as the readout

4.1.7 Compliance and Transmissibility

To verify the predicted performance of the sensor to isolate a plant, its Compliance and Transmissibility are obtained. The Compliance is obtained by using the sensor's voice coil as the excitation source. The signal sent to the voice coil actuator is a sinusoidal sweep excitation $F_{\mathrm{a}}(s)$ from 0.01 Hz to 1 kHz during 60 s cyclically during 600 s. The Transmissibility is obtained by measuring the Ground motion both with the µVINS and the reference sensor Guralp GS13 during 600 s. The sensors are placed close to each other, on the ground. The Ground motion $W(\mathrm{s})$ is extracted by multiplying the Guralp signal by the inverse of its transmissibility in the Laplace domain.

The results are shown in the figure 4.19. The phase is flat from its resonance frequency up to more than 100 Hz. There are no spurious resonances in the operating range of the sensor. It validates the analytical and numerical predictions stated in the previous section. Regarding the low-frequency domain, it can be seen on the Transmissibility graph that the signal of the µVINS is coherent from 200 mHz in its current open-loop configuration.

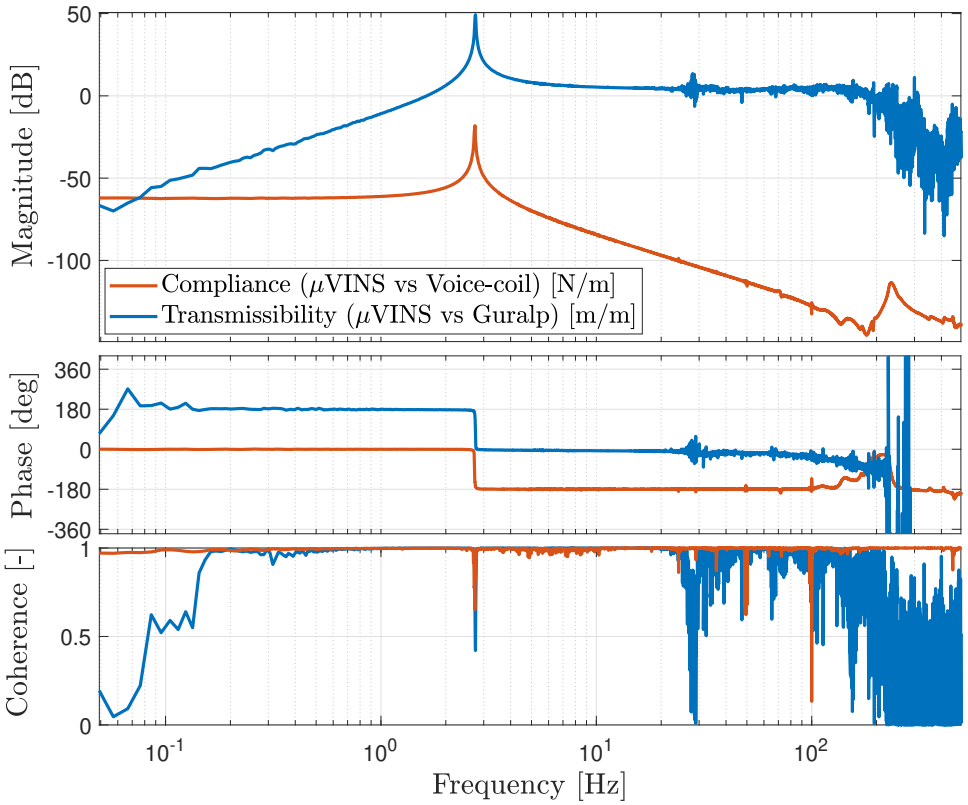

Figure 4.19: Compliance and Transmissibility of the µVINS. The voice coil of the sensor is used as the excitation to obtain compliance. The transmissibility is obtained using the Guralp GS13 as the Ground vibration reference sensor.

4.1.8 Discussion

To enlarge the operating range of this sensor in the low-frequency domain, A. Amorosi is studying active control strategies. The inertial mass can be actuated using its VCA. Although active control can improve its performance in the low-frequency domain, lowering its resonance frequency eases the method. A study with M. Zeoli (Master thesis student at PML) reported that negative stiffness can be applied to the structure depending on the position of the clamping point of the astatic leaf-spring suspension from the hinge of the inertial mass. Figure 4.20 shows the testbench designed to experiment with different clamping point configurations. The next iteration of the inertial sensor design will consider the results of this study as well as the results of the thermo-elastic damping characterization of the fused silica experiment mentioned earlier.

4.2 Experimental Optimization of a Suspension Mechanism for a Low-Frequency Vertical Inertial Sensor

A specificity and limitation of vertical inertial sensors is that they require a suspension. Being on Earth, a massive object, a gravitational force is present at its surface attracting the object towards its centre. So, to maintain the equilibrium of an oscillating mass, a suspension mechanism is used to compensate for the gravity. It shall then compensate the gravity preventing adding stiffness to the oscillating mass. And, it shall respect the dimension of the sensor specification. Depending on the selected suspension mechanism, the sensor could become quite bulky.

First, the mass can be suspended by a very long soft spring to limit its stiffness. However, it is not compact at all. As depicted by Collette [25], various strategies have been explored in the past using a zero-length spring mechanism. The first design was done by Lacoste [47]. Then, a more compact version was presented by Wielandt and Streckeisen [90], called the astatic leaf spring suspension. Other interesting gravity compensation strategies have been presented such as using an anti-spring [13] or using a permanent magnet [64]. For the sake of compactness and feasibility, the astatic leaf spring suspension has been selected for our vertical inertial sensor solutions. As the leaf spring is a three Degrees of Freedom flexure joint, this type of suspension adds spurious resonances to the oscillating mass. This is mitigated in our case by the proof mass flexure joint selected in the last section. Then, the oscillating mass is constrained except in its specific Degree of Freedom. Concerning the spurious resonances, the internal mode of the leaf spring can be a problem. As the leaf spring undergoes a very large deflection, its modal analysis is difficult. The assumption of the small deflection to simplify the resolution of the Bernoulli-Euler equation cannot be stated. Howell [40] presented a method to analyze large deflection for a simple case. However, as the modal analysis depends a lot on the extremity conditions, our setup cannot be resolved easily. Also, the conditions at the extremities of the leaf springs are not defined. They need to be defined to minimize the resonance frequency of the mechanism. So, a test bench was designed to define these conditions experimentally.

4.2.1 Suspension Tuning Experiment Tested With the µVINS proof mass

The first test bench built for this purpose was designed for the µVINS sensor suspension optimization (figure 4.20). This is the sensor designed in the last section for an absolute quantum gravimeter hybridization. The proof mass is guided using a double parallel short Copper Beryllium leaf spring flexure joint. The test bench allows for variation in the position of the fixed clamping point of the astatic leaf spring suspension and its angulation. The length of the leaf spring suspension was increased to allow a wider position range testing. Its length in the original µVINS sensor is $L = 105$ mm. Its length in the suspension testing configuration is

L = 140 mm. Its thickness is 240 µm and its width is 46 mm.

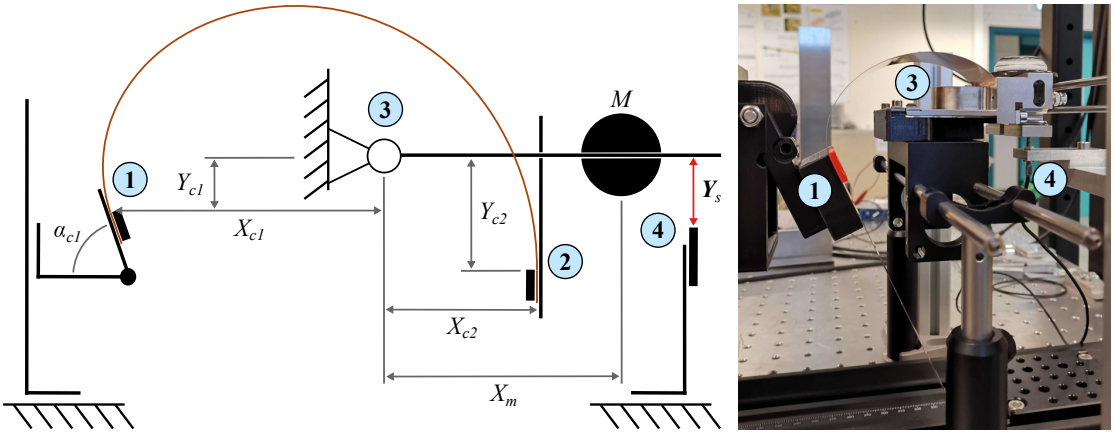

Figure 4.20: The µVINS astatic leaf-spring suspension test bench. It is composed of the µVINS proof mass, a Copper-Beryllium leaf-spring astatic suspension clamped to the fixed frame (1) and to the proof mass (2), a Copper-Beryllium leaf-spring hinge (3), a 3-axis redundant moving platform at the clamp position (1) (2 translations and 1 rotation) and an Eddy current displacement sensor (4). In this configuration, a resonance frequency of 240 mHz was attained.

Results Figure 4.21 shows the resonance frequency of the µVINS proof mass for different clamping positions and inclinations. It has been observed that the resonance frequency decreases when the clamping position is lowered than the hinge position. There is a vertical position from which the equilibrium becomes unstable. It is therefore not an acceptable configuration for a robust sensor. Introducing an inclination of the clamping points allows pushing the limit of this instability. A configuration was found which allows to lower the resonance frequency from the nominal design of one order of magnitude. However, the horizontal equilibrium becomes unstable. A slight excitation of the proof mass can result in pushing the oscillator out of equilibrium. A numerical analysis was also designed to simulate this setup by Morgane Zeoli using the Metafor software toolbox. It will then be useful for further design analysis limiting the need for experimental work. Then, only experimental validation will be required.

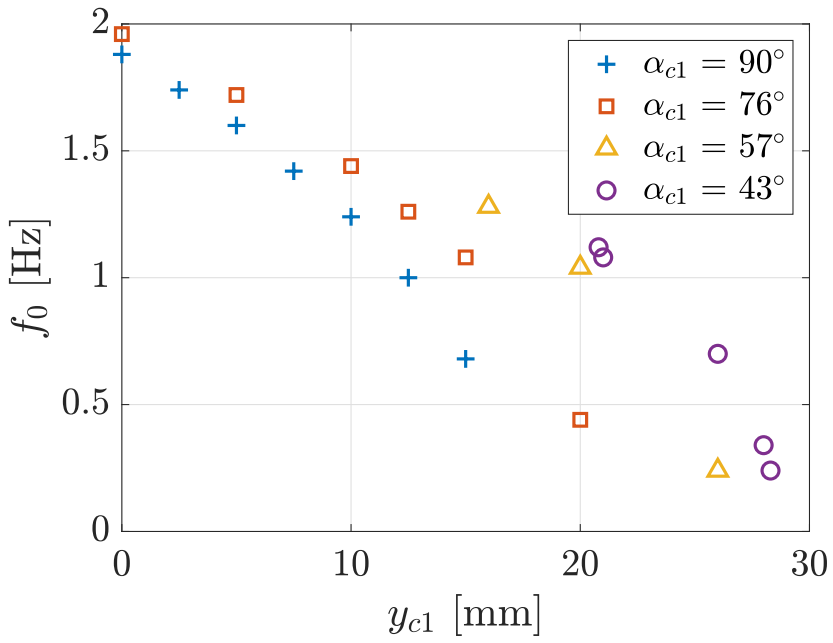

Figure 4.21: Resonance frequency dependence on the astatic suspension clamp (1) vertical position and its inclination.

4.2.2 Suspension Tuning Used for The Conception of a New Vertical Inertial Sensor

From the previous test bench designed to tune the suspension of the µVINS sensor, a second project has been undertaken. The control team of the Precision Mechatronics Laboratory needs a low-frequency vertical inertial sensor for the active isolation of a platform used to isolate a 100 kg mirror from the Ground vibrations. As the proof mass design is free, the clamping point of the suspension can be chosen. The suspension test bench was then used to define the position of the clamps and the inertia of the proof mass. The goal is to design a sensor with the lowest possible resonance frequency keeping a stable horizontal equilibrium. A new plastic part has been designed to allow tuning the position of the suspension clamp on the proof mass side and its centre of mass position. For the sake of simplicity, the inclination of both clampings was fixed to 90°. The new test bench is illustrated in figure 4.22.

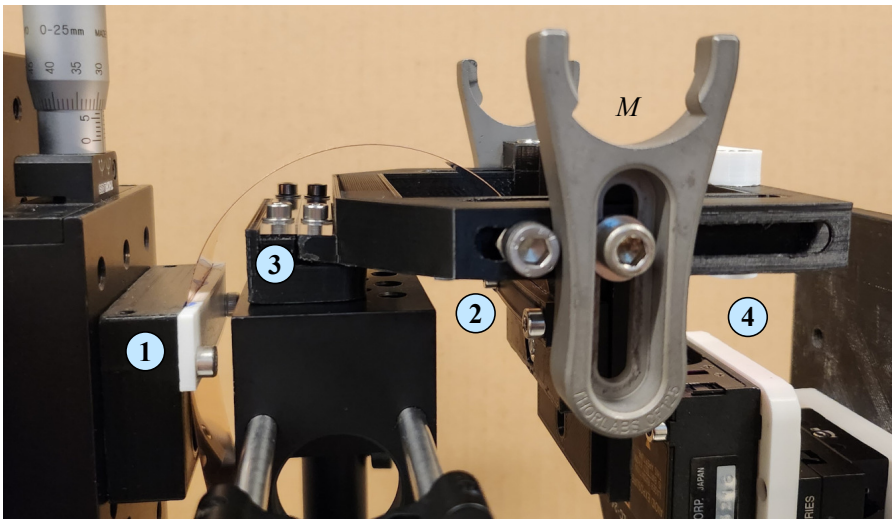

Figure 4.22: The E-VINS astatic leaf-spring suspension test bench. The scheme is similar to the one presented in figure 4.20. It is composed of an adjustable proof mass M, a Copper-Beryllium leaf-spring astatic suspension clamped to the fixed frame (1) and the proof mass (2), a fused silica leaf-spring hinge (3), a 2-axis redundant moving platform at the clamp position (1) (2 translations), a 2-axis moving platform at the clamp position (2) (2 translations) and a laser displacement sensor (4). The inclination of the clamp (1) is kept at 90°.

A test campaign is performed in three rounds. The different configurations of the sensor mechanics are listed in table 4.2. The inputs of the experiment are the positions of the suspension leaf spring clamping points x_{c1}, y_{c1}, x_{c2} and y_{c2}, the position of the proof mass x_m and the length of the leaf spring L. The outputs are the length of the suspension mechanism d_{size}, the resonance frequency of the oscillator and a parameter representing the stretching of the leaf spring suspension. They are obtained as below:

1. The horizontal size of the sensor mechanics d_{size}. It corresponds to the space required in the inertial sensor design required by the proof mass and its suspension.

$$d_{size} = x_{c1} + max(x_{c2}; x_m) + 30 \text{ mm} \tag{4.23}$$

   with 30 mm being the size of the clamps and other mounting features;

2. The natural resonance frequency of the proof mass f_0 obtained from a ring-down test using a Keyence LC-2440 laser displacement sensor to measure the oscillation amplitude;

3. The parameter describing the stretching of the suspension blade

$$c_{stretch} = 100 \times \frac{D_{circle} - (x_{c1} + x_{c2})}{D_{circle}} \tag{4.24}$$

with D_{circle} the diameter of a half circle of length L.

The experiments performed during the three rounds are listed in table 4.2 separated into three blocks by a horizontal line. The first block of rows corresponds to a test campaign with a Copper-Berrylium parallel leaf-springs hinge. The next block composed of two rows corresponds to a validation test campaign using a fused silica monolithic parallel leaf-springs hinge. For the sensor design, Copper-Berrylium will be used but the fused silica version is useful as a validation hinge. As it is monolithic, the length of the parallel leaf springs does not depend on the clamp mounting. Their length is 500 µm, their thickness is 50 µm. The last block composed of three rows corresponds to a second test campaign with Copper-Berrylium parallel leaf springs. The goal is to verify the repeatability of the mounting.

The first round is exploratory. It means that no output parameter was selected to define the following test. It studies the overall range of the tuning possibilities of the test bench. Then, to select the interesting configurations, some limits are defined. They are listed as the following:

1. d_{size} must be lower than 125 mm to limit the sensor's horizontal size. This limit was defined according to the available space for the sensor mechanics.
2. f_0 must be lower than 1.6 Hz as the value communicated to the end users of the sensor was 1.5 Hz.
3. c_{stretch} must be lower than 12. It has been observed that with a $c_{\text{stretch}} > 12$, the equilibrium is getting unstable.

The results that exceed those limits are shown in red in table 4.2.

Results The acceptable configurations are highlighted in grey in table 4.2. The length L of 114 mm instead of 121 mm was kept to limit the resonance frequency of the internal modes of the suspension blade. Those configurations were selected as the starting configurations for the tests using the fused silica hinge joint. Then the last tests were performed by placing the Copper-Berrylium hinge joint. A slight difference was observed in the resulting resonance frequency. It is probably due to the mounting length of the hinge joint. Finally, a configuration with the smallest suspension length was selected and tested. It will limit the resonance frequency of the suspension's internal modes. As there was no fully defined specification of the sensor length, it has been defined to allow the integration of this sensor mechanics configuration. This last configuration result was then used to design the inertial sensor called E-VINS (figure 4.23).

Observations To minimize the natural resonance frequency and to keep the stability, it has been observed that the best configuration of the suspension blade is the following: the clamping points must be as low as possible (y_{c1} and y_{c2} must be maximized) and the shape

Table 4.2: E-VINS astatic suspension configurations

x_{c1} [mm]	y_{c1} [mm]	x_{c2} [mm]	y_{c2} [mm]	x_m [mm]	L [mm]	d_{size} [mm]	f_0 [Hz]	$c_{stretch}$
23	17.9	56	17	63	114	116	1.64	9
31	17	58	19	63	121	124	1.14	15
30	17	58	16	63	121	123	1.24	14
30	19	58	16	58	121	118	1.26	14
27.5	18	58	16	58	121	115.5	1.44	11
26.5	17	58	16	58	121	114.5	1.54	10
18.5	17	58	16	58	114	106.5	1.82	5
16	17	69	16	58	114	117	1.78	17
19	17	59	16	62	114	109	1.60	7
26	19	59	16	62	114	116	1.10	17
27	19	48	16	62	114	117	1.62	3
31.5	21	48	18.5	62	114	121.5	1.30	9
27	20	53	18.5	62	114	117	1.42	10
24.5	19	53	18.5	62	114	114.5	1.56	7
27	24	46.5	20.5	73	106.5	130	1.46	8
30	24	40	22	79	107.5	139	1.46	2
24	17.5	53	16	62	114	116	1.44	6
25.5	18	53	16	62	114	117.5	1.38	8
25.5	18	53	16	62	114	117.5	1.24	8
32	24	40	17	75	107.5	137	1.40	5
32	22	40	19	75	107.5	137	1.34	5

of the blade must be close to a half circle slightly stretched horizontally. When y_{c1} and y_{c2} are increased, x_{c1} and/or x_{c2} must be increased as well to maintain the equilibrium. At some point, when the blade is stretched horizontally, the equilibrium becomes highly unstable.

4.3 Conclusion

Two distinct vertical inertial sensors were designed and manufactured. The first sensor, with a resonance frequency of 2.8 Hz, fits within a $10 \times 10 \times 10$ cm^3 box. The second, which is larger, has a 1.2 Hz frequency features an adjustable readout orientation and is easier to assemble with detachable subsystems. The first sensor uses fused silica flexure joints combined with aluminium and stainless steel parts, though assembly is challenging. Alternative materials like Copper-Beryllium or Titanium for the flexure joints were proposed for robustness. Optimization experiments determined ideal flexure joint dimensions. The first sensor's open-loop transfer function was compared to a Guralp GS13, showing good coherence between 200 mHz and 100 Hz. An astatic leaf-spring suspension for the proof mass was experimentally optimized, revealing that lowering the clamping points minimizes the resonance.

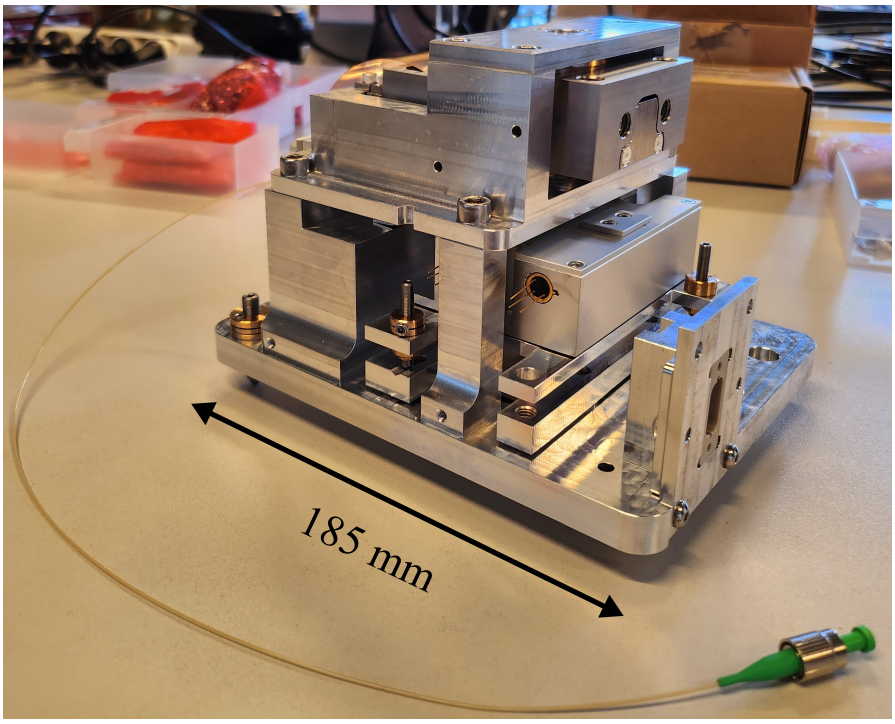

Figure 4.23: The E-VINS sensor. The inertial mass is kept at equilibrium using an astatic leaf spring suspension and guided in rotation by a Copper Beryllium parallel leaf spring joint. It is composed of a long-range Michelson interferometric readout. The interferometer position from the corner cube fixed on the proof mass can be adjusted in 4 axes (2 rotations and 2 translations). It can be mounted with a voice-coil actuator. It is vacuum-compatible. A lid is available and the proof mass can be blocked for transport. The drawings are available in the appendix 7.

5 Bragg Grating Sensor

Material Introduction The Bragg grating sensors as well as the mechanical specimen manufacturing are obtained using a femtosecond laser included in a machine which is called FEMTOprint. This machine features a three-axis precision moving platform (100 nm resolution) on which the glass substrate is fixed. The UV-grade fused silica glass substrate is provided by Siegert Wafers GmbH. A Thorlabs LMH-20x-1064 objective is used to focus the laser. The voxel waist is 1.5 μm in diameter and its height is 24 μm. To define the laser toolpath, a modified version of Alphacam by FEMTOprint SA is used. Each parameter of the laser can be tuned independently. After the laser exposition, the substrate is placed in a 12 M KOH bath at 85°C for wet etching.

Methodology Bragg gratings written with a femtosecond laser in fused silica are sensitive to temperature and axial strain. This type of sensor can be inscribed inside a flexible glass structure to measure a mechanical load. This technology allows including the sensing faculty in the structure during its manufacturing. It uses the same femtosecond laser to illuminate the shape of the structure that will be etched and to inscribe the optical sensor in this structure. So, the structure can be fully monolithic mitigating assembly complexity. As an example, figure 5.1 represents the scheme of a basic force sensor.

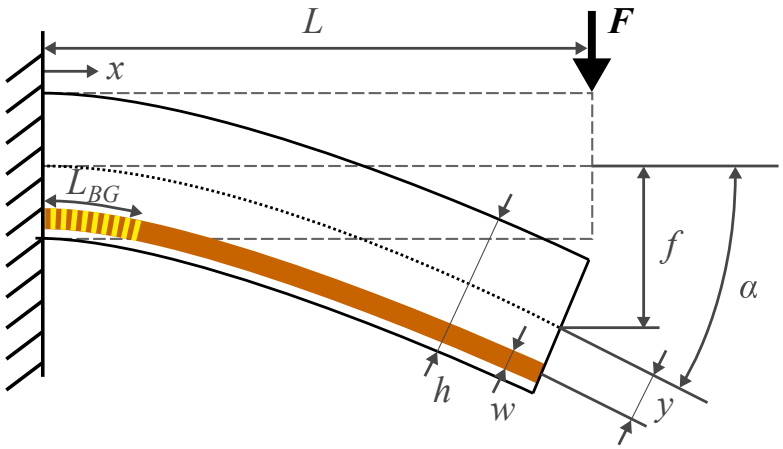

Figure 5.1: Scheme of a cantilever beam including a Bragg grating sensor of length L_{BG} in a waveguide of width w placed at a distance y from the neutral axis. The beam has a length L, a thickness h and a width b. When a force F is applied at the tip of the beam, it bends at an angle α. f is the vertical deflection of the tip.

The Bragg grating sensor is placed at the clamping point of a cantilever beam, closed to its surface. This location is the most sensitive since the strain is maximum (equation 5.1). When the tip of the cantilever beam is loaded, the beam structure is deformed. The strain in the beam material is maximum at the clamping point, at the top and bottom surfaces of the beam. The top surface is in traction and the bottom surface is in compression when a load F is applied at the tip of the beam. The strain inside the flexure can be obtained from the Euler-Bernoulli equation as:

$$\epsilon(x) = \frac{\Delta L}{L} = \frac{\alpha\rho(x) - \alpha(\rho(x)+y)}{\alpha\rho(x)} = \frac{y}{\rho(x)} = \frac{M(x)y}{EI} \tag{5.1}$$

using L, the length of the beam, α, the bending angle, ρ, the bending radius, y, the position of the centre of the Bragg grating sensor from the neutral axis, M, the bending moment, E, the Young modulus of fused silica (72 GPa) and I, the inertia of the considered beam section. Considering the beam is thin enough (its thickness h is much smaller than its length L), shear stress can be neglected with respect to normal stress. Therefore, the Euler-Bernoulli equation relates the loading of the beam expressed in terms of bending moment M to the geometrical deformation expressed by a local curvature radius ρ ($\frac{1}{\rho} = \frac{M}{EI}$). The bending moment in the beam of length L at a position x from the cantilever can be expressed as $M(x) = F(L-x) \qquad x \in [0;L]$ by applying a force F at its tip. So, by placing the Bragg grating close to the embedding, the strain can be estimated as $\epsilon \approx \frac{FLy}{EI}$, the Bragg grating length L_{BG} being negligible next to the beam length. By considering the inertia of the beam section, $I = \frac{bh^3}{12}$ with b, the beam width and h, the beam thickness, and $\frac{\epsilon}{\Delta\lambda_{\mathrm{BG}}}$, the strain sensitivity of

the Bragg grating, the force applied at the tip of the beam can be obtained as:

$$F = \frac{EI}{Ly}\epsilon = \frac{Ebh^3}{12Ly}\frac{\epsilon}{\Delta\lambda_{\mathrm{BG}}}\lambda_{\mathrm{BG}} \tag{5.2}$$

with λ_{BG}, the Bragg grating wavelength shift that can be measured using an Optical Spectrum Analyzer (OSA).

There are different steps explained in this chapter to obtain a Bragg grating sensor. First, the optical path needs to be defined. A waveguide is inscribed in the fused silica bulk (section 5.1). Then, the Bragg grating is written at the selected strain-sensitive location (section 5.2). To interface the waveguide containing the sensor to the OSA, an optical fibre connection is added (section 5.3). Finally, the shape of the structure is defined. The first part of this chapter lists the design rules obtained by my colleague, Matéo Tunon de Lara, during his work optimizing the femtosecond laser parameters to write waveguides and Bragg gratings inside bulk fused silica. This work was presented for the first time during the SPIE Photonics Europe conference [83]. Then, section 5.4 presents the first characterization of the sensitivity of our Bragg grating sensor inside tensile specimens. It is published in [84]. It also explains the interface of Bragg grating sensors including the method to extract the Bragg grating wavelength from the OSA. Then, the Bragg grating sensor was characterized in bending specimens (section 5.5). It is published in [1]. Finally, the method to characterize a Bragg grating in a torsion specimen is described in 5.6.

5.1 Waveguide Inscription

To write optical structures, the setup described in Chapter 3 is also used (figure 3.1). From the optical structure design, the laser toolpath is defined using the Alphacam software. All the laser parameters are defined using this software. These parameters are dependent on the laser objective of the machine. For the optical structure writing, the laser objective Thorlabs 20X is used. The tool size corresponds to the laser voxel. It is 24 µm high and has a 1.5 µm diameter (figure 3.1e). A machine command file is generated after defining the refractive index of the material (n = 1.45 for fused silica at λ = 1030 nm, the wavelength of the laser). Then, the previously selected laser objective is mounted. Next, the fused silica substrate is placed on its holder and fixed to the 3D translation moving platform of the Femtoprint machine. The position and orientation of the substrate are measured using the microscope of the machine. Finally, the command file is loaded to the machine and the machining program is started.

The purpose of the waveguide is to guide the light inside a transparent material. To do so, the core of the waveguide is defined by increasing the refractive index of fused silica along its designed path. The cross-section is defined such that it matches the interfacing single-mode optical fibre. The fibre has a diameter of 125 µm and its core has a diameter of 8 µm. To limit birefringence, the waveguide cross-section has to be as symmetric as possible. It also needs to be large enough to allow an easy connection with the fibre but not too large preventing it from becoming multi-modal. The selected design is a squared cross-section with 10 µm sides. Figure 5.2 shows the scheme of the toolpath defined as the following: for its height, only one height of voxel is enough; for its width, 500 nm spaced parallel lines are written. This spacing has been selected to optimize the homogeneity of the waveguide. IR visualization was used to verify that the waveguide section has a diameter of ≈ 10 µm. The most efficient laser parameters are the following: a pulse energy of 130 nJ, a moving speed of 20 mm/min and a repetition rate of 1 MHz.

5.2 Bragg Grating Inscription

The Bragg grating inscription process is similar to the waveguide inscription. Instead of defining parallel lines as the toolpath of the femtosecond laser along the waveguide length, they are defined perpendicular to the length of the waveguide. Their position is defined according to the selected structure-sensitive area as in the example of figure 5.1. The length of the Bragg grating depends also on the application but it should be greater than 1 mm. The longer the length of the Bragg grating, the more there will be cyclic defects, and then, the more the light will be reflected at the wavelength corresponding to the period of the defect. It affects the contrast of the Bragg grating spectrum. The distance between the lines is chosen to define the wavelength of the Bragg grating spectrum. It corresponds to Λ, the period of the defect.

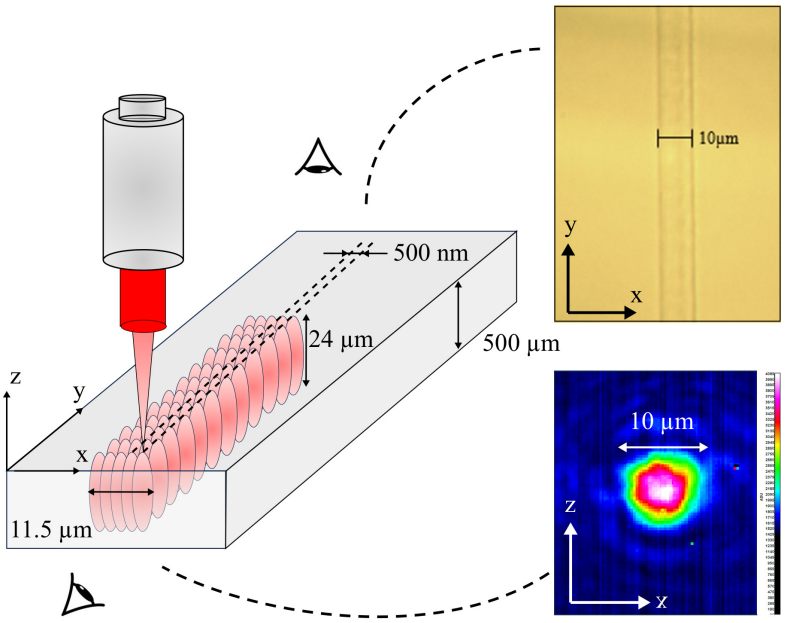

Figure 5.2: Scheme of the laser toolpath for a waveguide inscription. On top, a microscope top view of the inscribed waveguide. On the bottom, an IR microscope section view of the waveguide.

The wavelength of the Bragg grating is then:

$$\lambda_{BG} = 2n_{eff}\frac{\Lambda}{m} \tag{5.3}$$

with n_{eff}, the effective refractive index of the mode transmitted in the waveguide (~1.45) and m, the order of the mode. The most efficient laser parameters to inscribe Bragg gratings are the following: a pulse energy of 150 nJ, a moving speed of 15 mm/min and a repetition rate of 1 MHz. An example of a Bragg grating reflected spectrum is shown in figure 5.3. It shows also a view of the cyclic pattern seen from the top of the glass planar substrate.

5.3 Optical Fibre Interface

To complete the sensor, a mechanical connection is required between the waveguide containing the Bragg grating and the optical fibre of the optical spectrum analyzer. The proposed solution is to etch a hole to guide the 125 µm diameter optical fibre and a flat surface perpendicular to the waveguide to mitigate reflection losses at the interface. To ease the toolpath design, the cross-section of this hole is a square of 126 µm sides. After the wet etching step of 7 h in 12 M KOH at 85 °C, the average square side length is 130 µm. Figure 5.4 shows the interface in which an optical fibre is inserted. The large passing through holes has three roles: an entry for the etchant to the guiding hole to reduce the etching time and enhance homogeneity; access to ease the etched waste material removal; etch a clean flat surface to connect the fibre

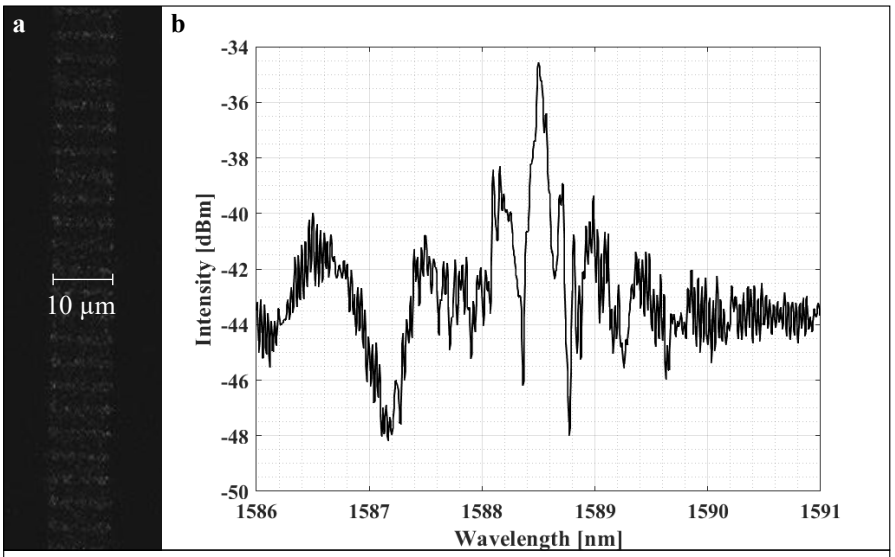

Figure 5.3: First Bragg grating obtained at our laboratory inscribed with a femtosecond laser in a fused silica plate. **a** Microscope picture of the top view of the laser cyclic pattern inscribed in the fused silica substrate. **b** Bragg grating reflected spectrum obtained with an optical spectrum analyzer.

to the waveguide. Index gel is used at the interface to enhance the coupling. To maintain the fibre, it must be placed in a fibre clamp close to the entrance of the guiding hole or glued to the structure.

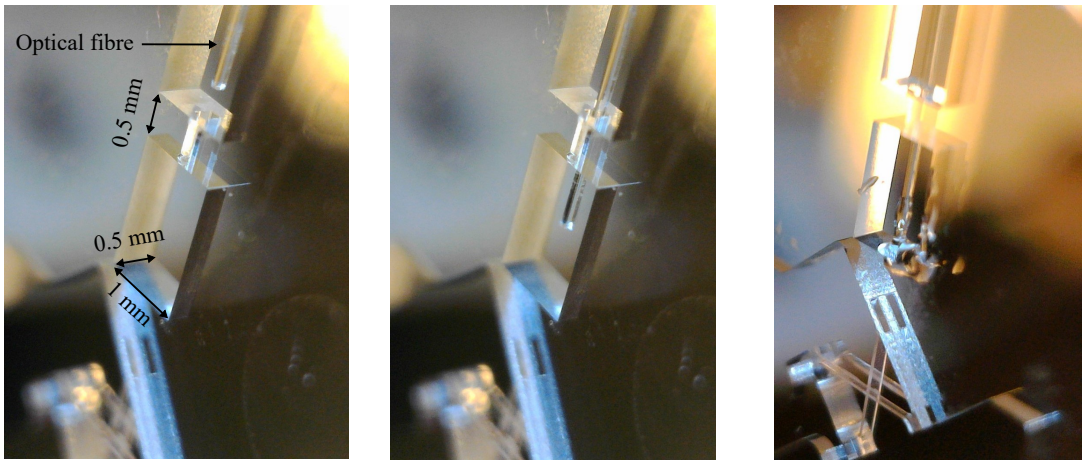

Figure 5.4: Insertion of the optical fibre through the mechanical interface specimens to connect the optical fibre with the waveguide written inside the fused silica bulk. The 125 µm diameter fibre is guided by the 130 µm side squared holes. In the right figure, the refractive index gel is added to the surface to enhance the coupling between the fibre and the specimen waveguide.

Inserting an optical fibre in this hole can be difficult. Thanks to new functionality in our Alphacam software, it is now easier to prepare the laser toolpath for curvy shapes. So, the guiding hole for the fibre can be circular and a funnel at their entrance is defined. Figure 5.5 shows the result of this new guiding structure. The insertion of the fibre is very easy and can be performed quickly by hand. However, the optical coupling is limited. It can be due to an increase in the friction in the circular cross-section hole. I suggest returning to the squared cross-section holes but adding the funnel to ease the fibre insertion. So, it will have the funnel to ease the insertion of the fibre and the hole that guides the fibre at the end of the funnel will have a squared cross-section.

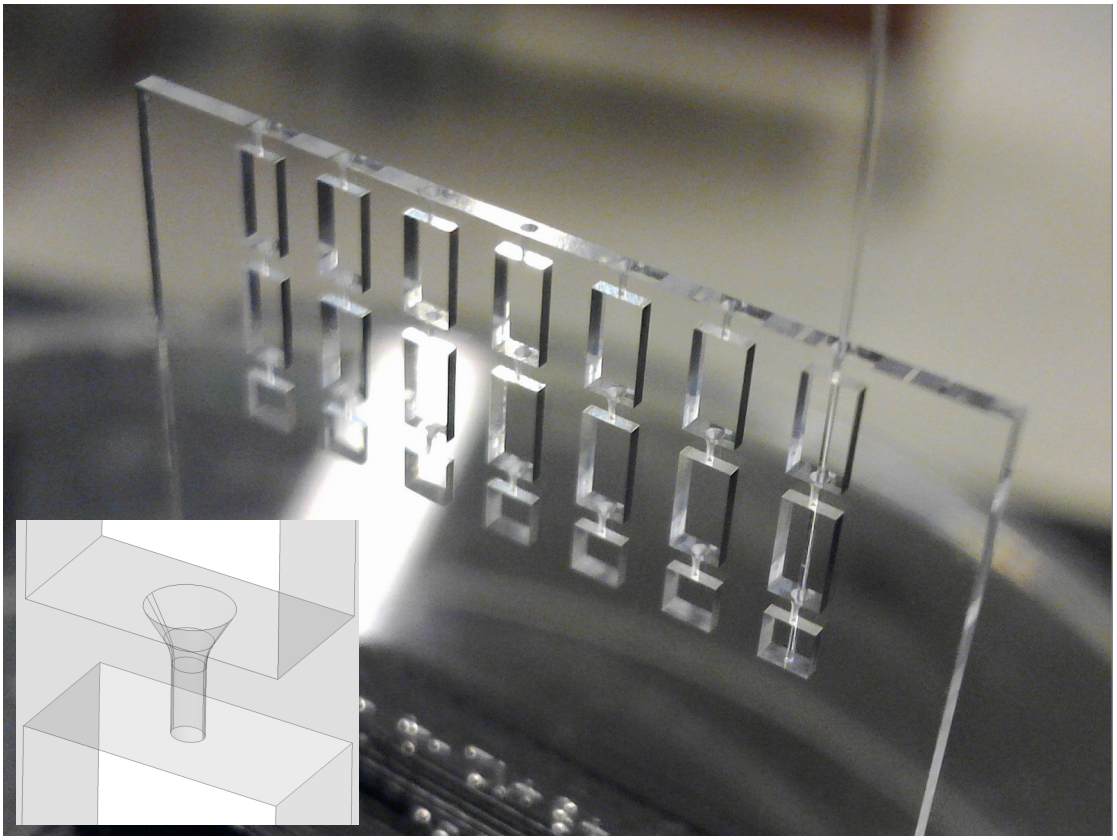

Figure 5.5: Mechanical interface specimens to connect the optical fibre with the waveguide written inside the fused silica bulk. This interface specimen contains guiding funnels to help the optical fibre insertion.

5.4 Tensile Characterization

To verify that the strain sensitivity model of FBG applies to Bragg gratings engraved in a glass substrate using a femtosecond laser, a 1-D experiment is designed. To measure axial strain, a Bragg grating is engraved at the centre of a tensile specimen along its length (figure 5.6). The tensile specimen is a well-known design used to extract the stress-strain characteristics of a material. It is a rectangular-shaped beam with rounded edges at both its larger extremities. Thus, it can be pulled inducing homogeneous strain in the beam. Here, the tensile specimen is linked in a monolithic structure to a translation flexure guiding to transfer of the applied load in the axial direction of the specimen. Figure 5.6 shows the geometry of the tensile specimen. It has been chosen as it can also be used to analyze bending strain:

- Its thickness should be significantly thinner than the other dimensions to consider it a flexure;
- Its thickness should be large enough to place a waveguide including a BG close to its surface; In the bending experiment, the wave-guide including a BG shall be close to the surface to maximize the BG axial strain;
- Its length shall be long enough to get a good contrast of the BG;
- It shall be as similar as possible to the flexure future application;
- The translation flexure guiding stiffness shall be negligible compared to the tensile specimen stiffness in the axial direction;
- The translation flexure guiding shall be stiffer in the other direction than the tensile specimen to transfer the load only in the axial direction;
- The rigid link of the monolithic structure to a fixed frame shall not affect the experiment.

Figure 5.6 shows the manufactured fused silica monolithic structure.

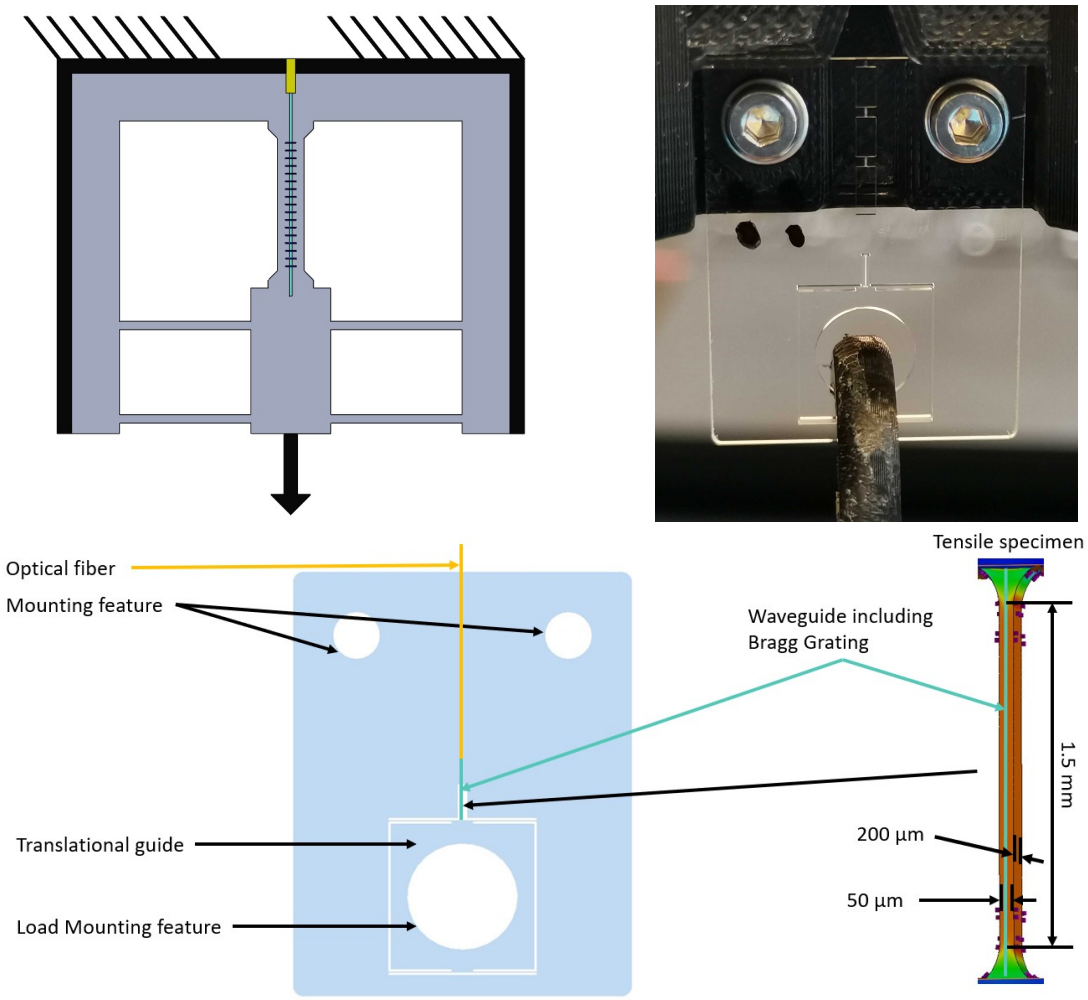

Figure 5.6: Tensile specimen including a wave-guide with Bragg gratings. At the top left, the scheme of the guiding to load the tensile specimen is inspired by [3]. On the top right, the manufactured monolithic mechanism hanging on two screws on a rigid 3D printed PLA frame. At the bottom, is the construction scheme of the mechanism.

Figure 5.7 shows a closer view of the specimen and how the optical fibre is interfaced with the Bragg grating sensor. The waveguide containing the Bragg grating is straight continuing after the tensile specimen up to the flat where the optical fibre is apposed. A space of 10 µm is left between the end of the waveguide and the flat surface. It prevents the waveguide from being etched by the KOH.

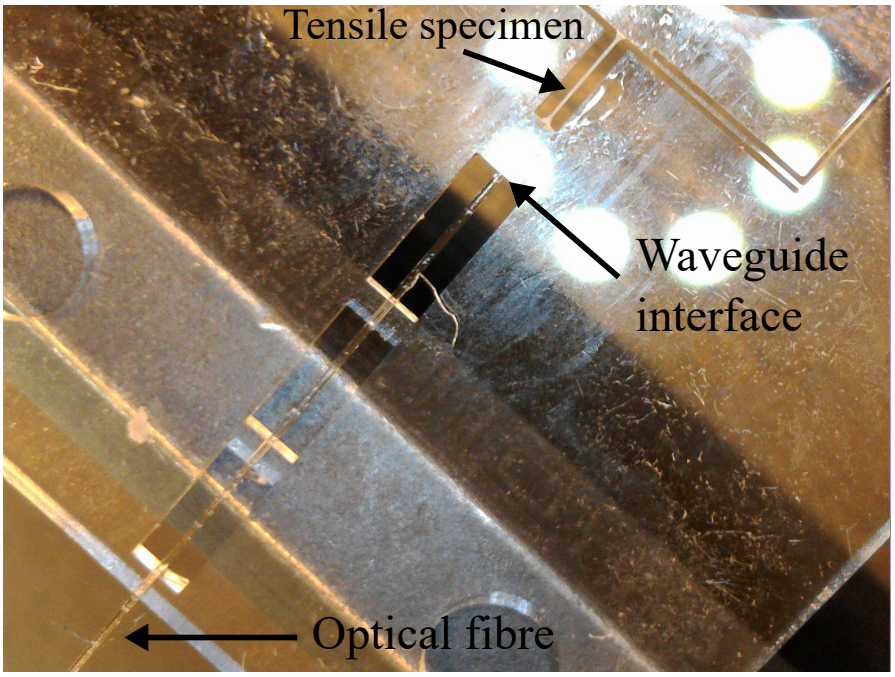

Figure 5.7: Optical fibre is inserted in the monolithic structure and connected by contact to the integrated waveguide containing the Bragg grating. Index gel is used to enhance the connection between the fibre and the integrated waveguide.

The test bench is detailed in the figure 5.8. The monolithic structure containing the tensile specimen is screwed to a frame made of PLA plastic by FDM manufacturing (orange rectangle and close view in figure 5.6). Optical fibre links the tensile specimen's waveguide to an Optical Spectrum Analyzer (OSA) FibreSensing FS2200 Industrial BraggMETER. The load is applied to the tensile specimen hanging a basket full of nuts to its translation flexure guiding. Adding or removing nuts inside the basket varies the load applied to the tensile specimen.

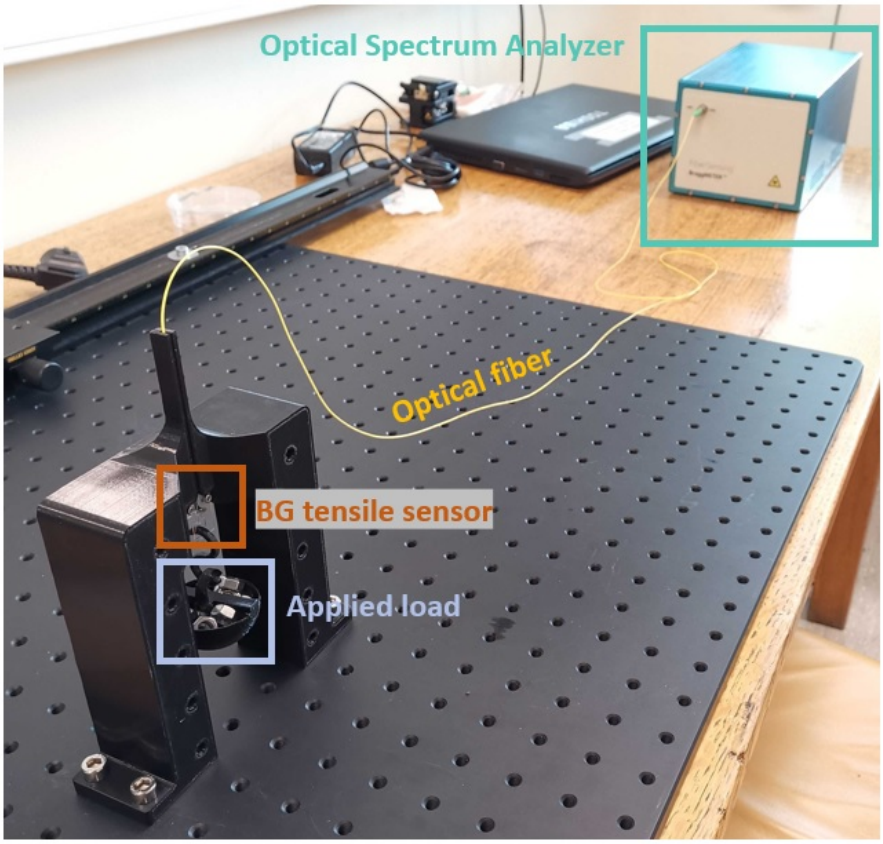

Figure 5.8: Testbench for the Bragg grating tensile strain sensing characterization. The strain is applied by hanging known weights to the specimen.

The load applied to the specimen can be expressed in strain to compare the obtained sensor sensibility to the model described by Equation (2.4). Hook's law for axial stress in a tensile specimen is

$$\sigma = E_{\text{fs}}\epsilon \tag{5.4}$$

With E_{fs}, Young's modulus of fused silica ($E_{fs} \approx 72$ GPa). The stress applied to the tensile specimen is obtained by:

$$\sigma = \frac{F_{\text{load}}}{S_{\text{specimen}}} \tag{5.5}$$

With S_{specimen}, the section of the tensile specimen ($50 \times 200\ \mu\text{m}^2$) and F_{load}, the applied load expressed as:

$$F_{\text{load}} = g(m_{\text{Basket}} + N_{\text{Nuts}}\, m_{\text{Nut}}) \tag{5.6}$$

With g, Earth's surface gravity (9.81 m/s^2), $m_{\text{Basket}} = 3$ g, $m_{\text{Nut}} = 1.3$ g and N_{Nuts}, the number of

Nuts in the basket.

The minimal load applicable is the mass of the basket. Then, according to the theoretical sensibility, to obtain a sufficient sensitivity curve the maximum strain should be at least two orders of magnitude higher than the theoretical resolution of the sensor. Taking the resolution of the OSA (≈ 5 pm) and the theoretical sensitivity of the Bragg grating given by Equation (2.5) (≈ 1.24 pm/με) the maximum strain should be higher than 200 με. Figure 5.9 shows the load-strain model obtained by combining Equations (5.4) and (5.5). Filling the basket of nuts applies more than 600 με to the tensile specimen.

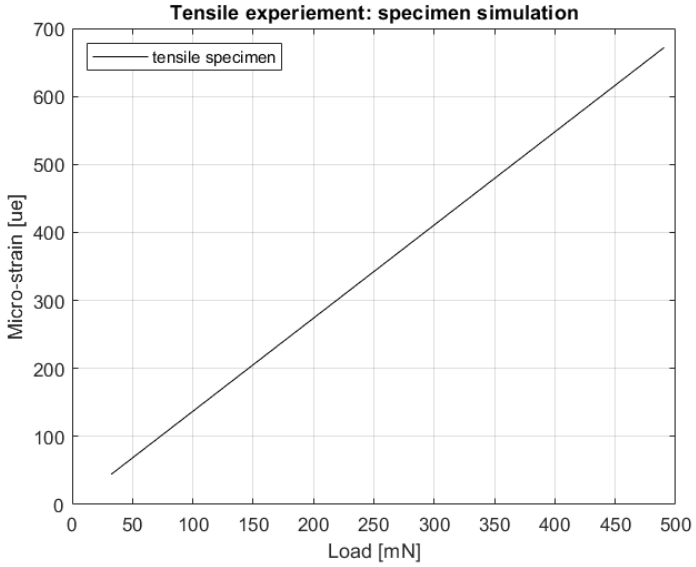

Figure 5.9: Tensile specimen load-strain model

Initially, the experiment was fully manual. The weights were measured using a precision scale and the Bragg wavelength was reported using the BraggSensing dedicated software. Then, the test bench was automated. The weight basket was replaced by a guided voice-coil actuator (VCA) (figure 5.10) and a LabVIEW platform was developed to acquire the VCA command and the reflectivity spectrum.

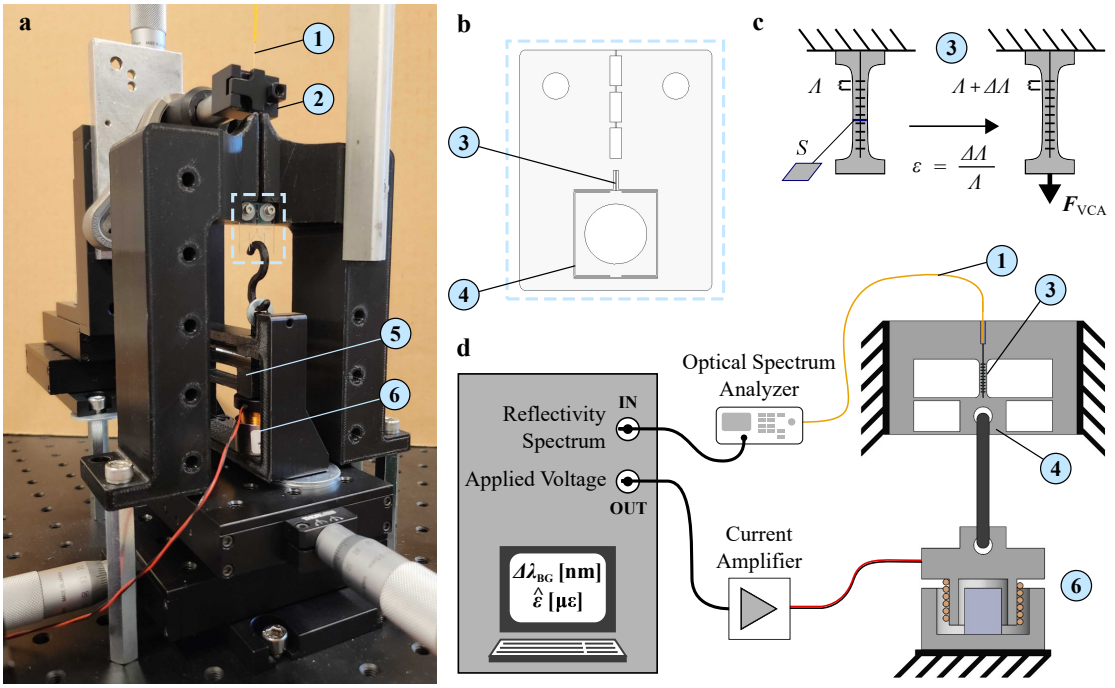

Figure 5.10: Testbench developed to characterize the axial strain sensitivity of a Bragg Grating sensor inscribed in a fused silica tensile specimen. **a** The tensile specimen (in the blue square) is hanging fixed by two screws. The optical fibre (1) connected to the Bragg interrogator is placed at the top. A fibre clamp (2) is used to position the fibre. **b** The tensile specimen (3) is included in a monolithic structure. **c** The tensile specimen contains a Bragg grating which undergoes a strain ε when the force $\boldsymbol{F}_{VCA}$ is applied at its free end (4). **d** Experimental scheme: the optical fibre (1) is guided to interface with the tensile specimen (3); the load is applied with a Voice-Coil Actuator (VCA) (6); the moving coil is guided in translation using a monolithic 3D printed flexure mechanism (5); A LabVIEW platform records the reflected spectrum from the interrogator and the applied voltage commanding the VCA; the estimated applied axial strain $\hat{\varepsilon}$ and its resulting Bragg grating wavelength shift $\Delta\lambda_{BG}$ are obtained by post-processing with Matlab.

Results First, figure 5.11 shows a comparison of the tensile tests using the nut basket and the guided voice-coil actuator. The wavelength of the Bragg grating is selected as the maximum of the reflectivity spectrum. The data follows the theoretical sensitivity. However, the repeatability is not good with the nut baskets. Also, besides the repeatability being stable using the VCA, the sensitivity is lower than the theoretical sensitivity and there are jumps. It seems that it follows the theoretical sensitivity but needs to be investigated.

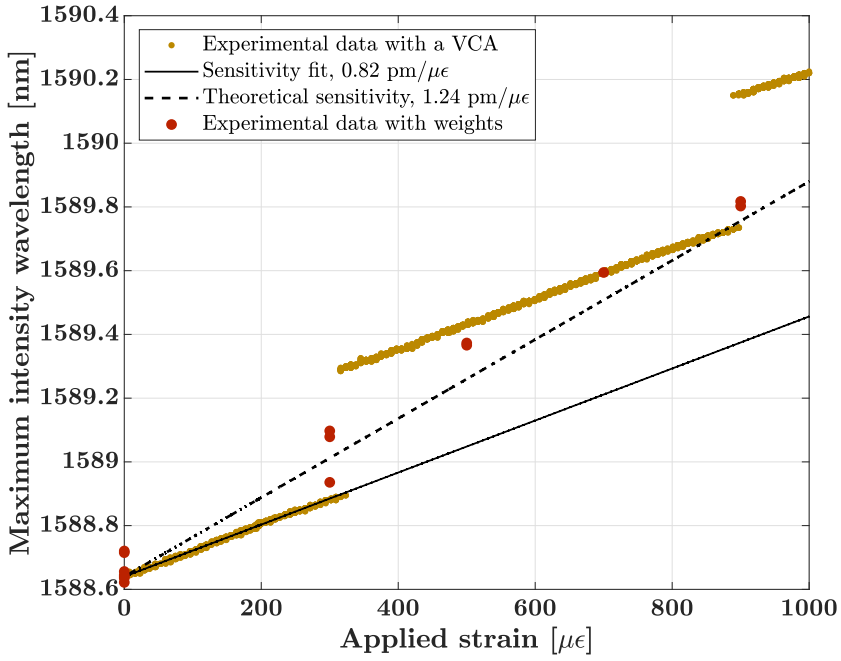

Figure 5.11: Comparison of the Bragg grating sensitivity of the tensile specimen c obtained using a VCA and hanging known weights of 0, 300, 500, 700 and 900 με

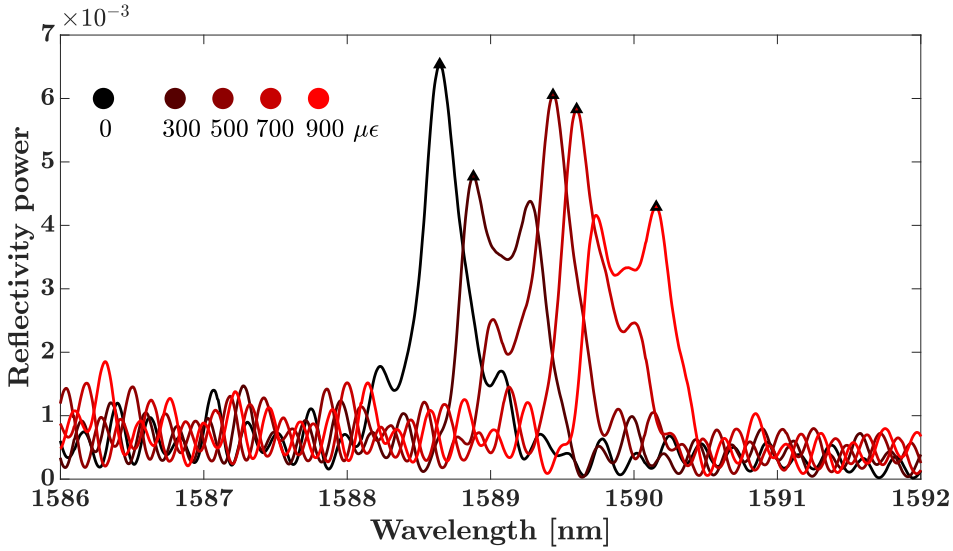

Figure 5.12: 5 reflectivity power spectrum of the specimen c measurement at 0, 300, 500, 700 and 900 με. Strain is applied to the tensile specimen using a VCA. The maximum of the reflectivity of each spectrum is indicated with a triangle. They correspond to 5 points of the "Experimental data with VCA" in figure 5.11.

Figure 5.12 shows the reflectivity power spectrum of the sensor specimen c for 5 different

loading states (0, 300, 500, 700 and 900 με). The maximum reflectivity wavelength jump can be explained by looking at the reflectivity power spectrum of the specimen loaded with 300 and 900 με. Loading the tensile specimen, the Bragg peak is moving, its magnitude is decreasing while another peak magnitude is increasing. At some point, the magnitude of the following peak is greater than the original Bragg wavelength peak.

Reflectivity Spectrum Post-Processing Approach To obtain a better estimation of the Bragg grating wavelength, a new post-processing approach is defined (Figure 5.13). Instead of selecting the maximum of the reflectivity spectrum, the reflectivity centroid is extracted by integrating the spectrum in the wavelength window of interest.

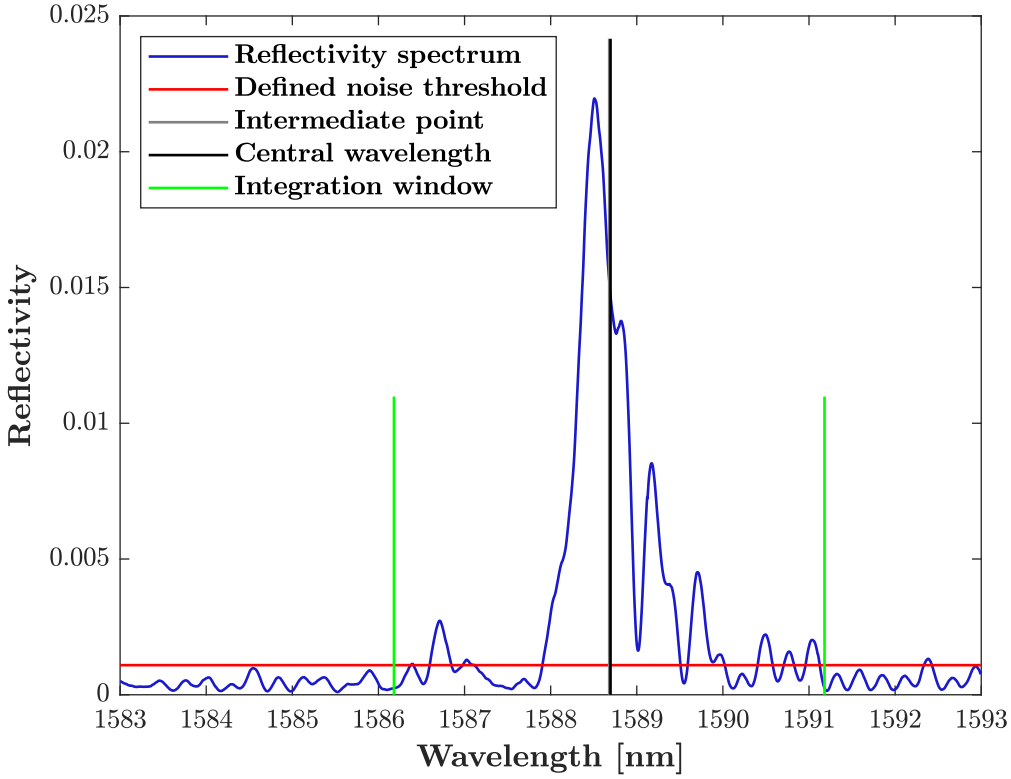

Figure 5.13: Reflectivity spectrum of the Bragg grating used in the flexure pivot joint lever experiment. The central wavelength is obtained by integrating the spectrum in two steps. The first time, the integration is done on the entire measurement window (from 1583 nm to 1593 nm) and above the defined noise threshold (For this sensor, 0.0011 is used). Then, a second integration is performed in the same way but in a reduced integration window (5 nm) centred on the previously obtained central wavelength (the intermediate point). This two-step integration does not change substantially the result but is kept for robustness.

Then, the loading experiment was performed on 3 different tensile specimens (a, b, c) using

the guided VCA. The results are presented in figure 5.14. The reported experimental data is obtained following the maximum of the acquired reflectivity spectrum and using the new centroid post-processing approach. The sensitivity of the 3 sensors is quite similar. There are multiple wavelength jumps of the maximum peaks. Using the centroid approach, no more jumps are observed in the $\Delta\lambda_{BG}$ - applied strain characteristics. Their sensitivity is ranged from 1.1 pm/με to 1.4 pm/με. It compares with the theoretical sensitivity of 1.24 pm/με and the standard deviation for each specimen is in the range of 10 pm to 20 pm. The resolution of the OSA being ±5 pm, it is reasonable to say that the OSA limits the resolution of the Bragg grating sensor.

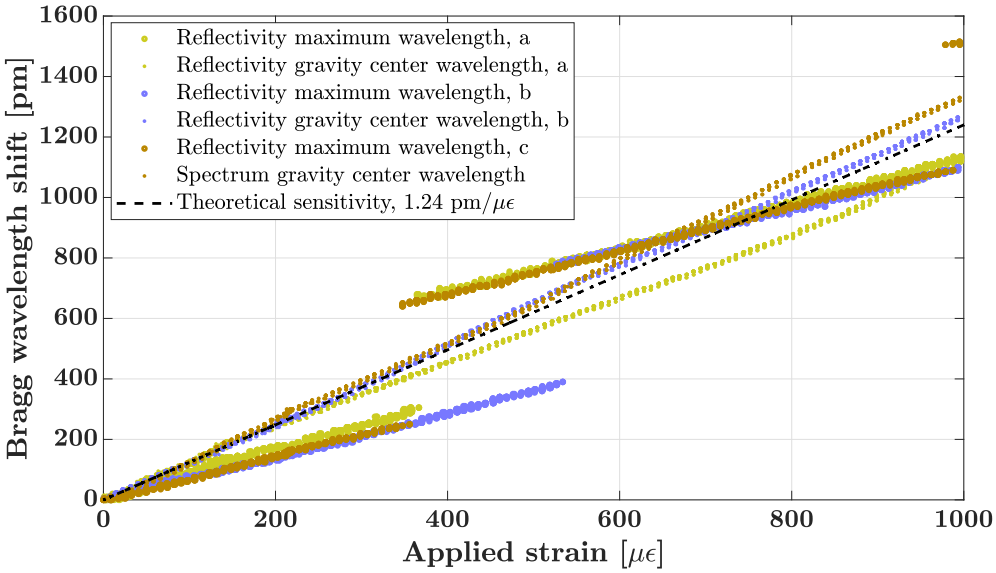

Figure 5.14: Bragg grating sensitivity to the axial strain of three different specimens of tensile strain sensors. Strain is applied using a VCA. The VCA command is set such that the strain applied varies from 0 to 1000 με.

Discussion To verify that the test bench design does not influence the sensitivity, the same setup was used to strain a reference Fiber Bragg Grating (FBG) sensor. This reference FBG is manufactured in a single-mode optical fibre at the University of Mons using a manufacturing system designed for producing Fiber Bragg Gratings Noria by NorthLab Photonics. The spectrum of the FBG under different strains is shown in figure 5.15 and the sensitivity in figure 5.16. Comparing these results to figure 5.12 and to figure 5.14, it confirms that the deformation of the reflectivity spectrum is caused by the manufacturing and/or the assembly of our specimens.

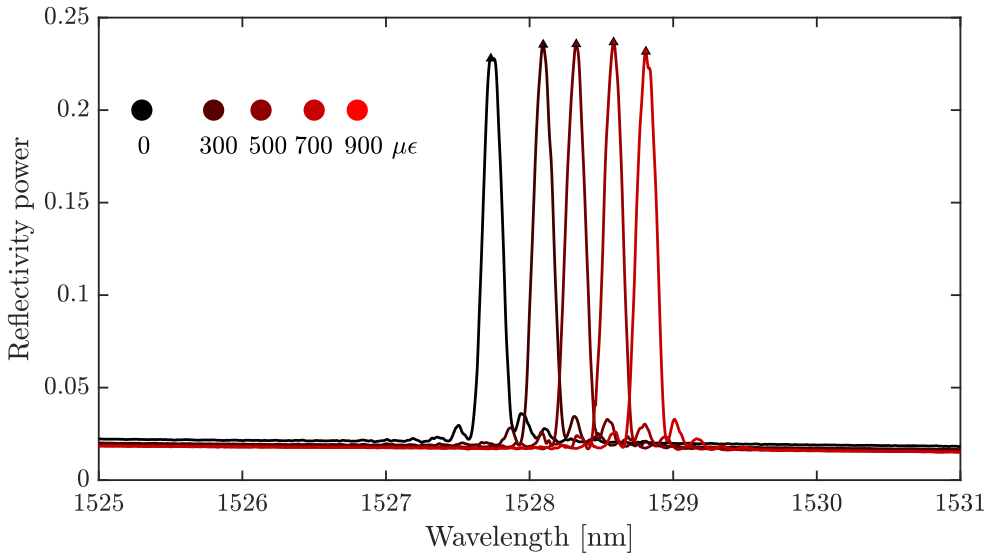

Figure 5.15: 5 reflectivity power spectrum of the reference Fiber Bragg Grating (FBG) at 0, 300, 500, 700 and 900 με. Strain is applied to the tensile specimen using a VCA.

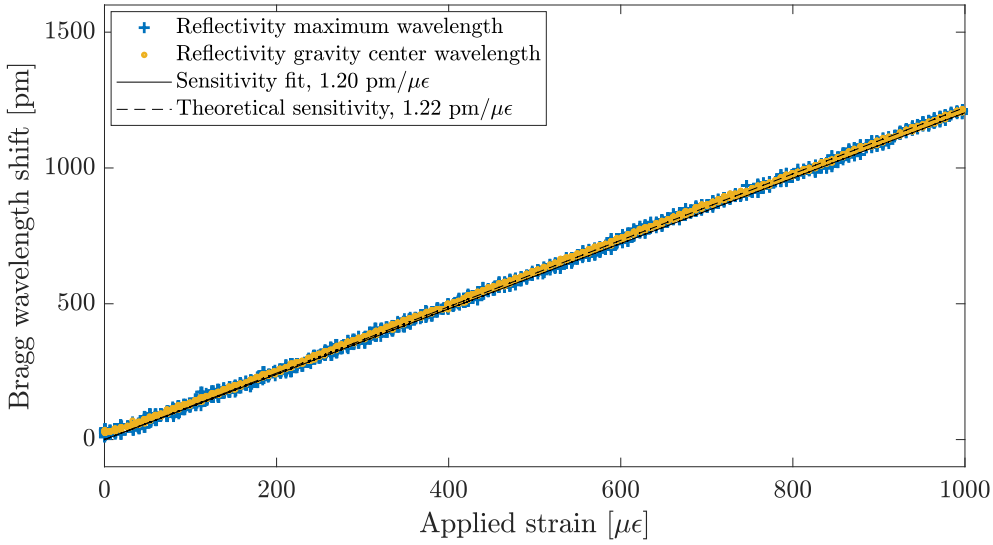

Figure 5.16: Bragg grating sensitivity to the axial strain of the reference Fiber Bragg Grating (FBG). Strain is applied using a VCA. The VCA command is set such that the strain applied varies from 0 to 1000 με.

Regarding the loading of specimen c with weights, the sensor sensitivity is close to the theoretical one. However, the variance of the experiment is significant. When removing, and hanging a weight on the specimen, there is a variation in the magnitude and wavelength of the reflectivity power spectrum maximum. It could be explained by the fact the optical fibre

connected to the specimen waveguide is not attached. It is guided by holes in the monolithic structure (visible in figure 5.7) and stays still by friction. It is possible that this optical fibre moves when the structure is touched. Then, some parasitic effects at the fibre waveguide interface may influence the acquired reflectivity power spectrum. When using the VCA, there is less vibration and thus less variance regarding the sensitivity. However, this does not explain the wavelength jump behaviour observed while loading the specimen with the guided VCA. There are multiple hypotheses to explain this behaviour and they may all be connected:

- As the wave-guide is not symmetrical due to the laser voxel shape, significant birefringence could occur. M. Tunon de Lara reported that a Bragg grating wavelength shift of 142 pm was observed depending on the polarization angle. It corresponds to a birefringence of 1.34×10^{-4} (journal paper under review). This could explain the behaviour of our sensor in figure 5.12. However, we did not manage to prove this assumption using a polarizer.
- The numerical aperture (NA) of the waveguide could be large enough so multiple modes can pass through; M. Tunon de Lara could deduce an NA of 0.04. Being < 0.4, the waveguide is a single-mode [42]. However, it has been tested with a red wavelength only. So, the NA characterization should be performed for IR wavelengths.
- The application of the force is not perfectly axial to the tensile specimen. This could result in shear of the specimen which is significant enough to change the maximum of the reflectivity power spectrum. A translation platform below the VCA on the test bench was installed (figure 5.10). No influence on the sensitivity was observed by moving the VCA ± 2 mm in the 4 directions.

Then, another experiment is designed and detailed in the following section to characterize the specimen in bending. The geometry of the studied specimen allows us to directly use the outputs of this experiment for our current potential experimental applications.

5.5 Bending Characterization

The waveguide and the Bragg grating are inscribed at first. The Bragg grating shall be placed as far away as possible from the neutral beam axis to maximize its sensitivity to the beam bending. The neutral beam length, located at the centre thickness (dotted line in Figure 5.17 (c)), is constant during bending. For further notation, the length of the Bragg grating is noted L_s and the length of the neutral axis in the portion of the beam where the Bragg grating is present is noted L_0. According to Euler Bernoulli's theory, the strain applied to the Bragg grating in a horizontal portion of the beam at a horizontal position x can be estimated as:

$$\epsilon(x) = \frac{\Delta L}{L} = \frac{\alpha\rho(x) - \alpha(\rho(x) + y)}{\alpha\rho(x)} = \frac{y}{\rho(x)} = \frac{M(x)y}{EI} \tag{5.7}$$

using L, the length of the portion of the beam (1.5 mm), α, the bending angle, ρ, the bending radius, y, the position of the centre of the Bragg grating sensor from the neutral axis (10 µm),

M, the bending moment, E, the Young modulus of fused silica (72 GPa) and I, the inertia of the considered beam section. Considering the beam is thin enough (its thickness h = 50 µm is much smaller than its length L), shear stress can be neglected concerning normal stress. Therefore, the Euler-Bernoulli equation relates the loading of the beam expressed in terms of bending moment M to the geometrical deformation expressed by a local curvature radius ρ ($\frac{1}{\rho} = \frac{M}{EI}$).

The Bragg grating is fabricated in the substrate by inducing a periodic defect plane-by-plane with the femtosecond laser. The planes are perpendicular to the inscribed waveguide. They are made of lines with the femtosecond laser. Its translation speed is 15 mm/min and the pulse energy is 150 nJ with a repetition rate of 1 MHz. The Bragg grating wavelength is the centre of gravity of the reflected spectrum defined as:

$$\lambda_{\mathrm{BG}} = 2 n_{\mathrm{eff}} \frac{\Lambda}{\mathrm{m}} = 1595 \text{ nm} \tag{5.8}$$

with n_{eff}, the effective refractive index of the mode transmitted in the waveguide (~1.45), Λ, the period of the defect (~1.1 µm) and m, the order of the mode (2).

The Bragg grating is sensitive to axial strain and to the temperature gradient. The shift of the central wavelength of the Bragg grating reflected amplitude spectrum can be expressed in equation 2.1. For this study, the temperature gradient is considered negligible compared to the applied strain during the experiments. As described in [20], the sensitivity to axial strain can be expressed as:

$$\frac{\Delta \lambda_{\mathrm{BG}}}{\Delta \epsilon} = \lambda_{\mathrm{BG}} (1 - p_{\mathrm{e}}) \tag{5.9}$$

with p_{e}, the strain-optic constant of the material (equation 2.5).

With the defined $\lambda_{\mathrm{BG}} \approx 1595$ nm, it gives a theoretical sensitivity to an axial strain of 1.24 pm/µϵ. µϵ corresponds to a strain of 10^{-6}. It is suited to express typical strain values for Bragg grating sensors.

This sensitivity is then compared to the characterized sensitivity deduced from the following experiments by estimating the applied strain from mechanical assumptions. The Bragg grating shift is measured by interfacing the Bragg grating of the specimen to the data acquisition system FiberSensing BraggMETER FS 2100 with an optical fibre.

To verify the operating principle of our Bragg grating bending sensor, three experiments are performed. These tests allow us to characterize the strain sensitivity of the sensor. The first one, the Three-point flexural test, is a conventional test to obtain the stress-strain response of a material. The second test, the cantilever beam bending test, verifies the conventional beam deflection model in structural engineering. Finally, the third test, the flexure pivot joint lever, verifies the sensor integration in a micro-scale flexure to validate its use in monolithic micro-scale mechanism design.

Three-point flexural test In this first experiment detailed in Figure 5.17, the load is applied at the centre of the beam. The beam is horizontal and sits on two fixed rods. The bending moment can be expressed as:

$$M(x) = \frac{F}{2}x \qquad x \in [0; \frac{L}{2}] \tag{5.10}$$

with F, the loading at the center of the beam, x, the position from one fixed point and L, the distance between the two fixed points.

The force is applied with a stainless steel cantilever beam clamped on a vertical translation moving stage. A ceramic ball is glued at the tip of this cantilever beam to apply the load at a precise position on the glass beam. The displacement of the vertical stage f_1 and the depth at the ball location f_2 are measured using two laser displacement sensors Keyence LC-2440. The stiffness K_{fF} of the stainless steel cantilever beam is obtained experimentally. This calibration is performed by placing a fixed precision scale (OHAUS YA102) under the ceramic ball and applying load by translating the vertical stage.

$$K_{\text{fF}} = \frac{F_{\text{scale}}}{f_1} \tag{5.11}$$

Then, the load applied on the glass beam can be expressed as:

$$F = K_{\text{fF}}(f_1 - f_2) \tag{5.12}$$

The Bragg grating is located at the horizontal centre of the beam ($x = \frac{L}{2}$) at a distance y from the neutral axis (83 µm). Its length being much smaller than L (30 mm), we can assume:

$$\epsilon = \frac{K_{\text{fF}} L y}{4EI}(f_1 - f_2) \tag{5.13}$$

with I, the inertia of the considered beam section, $I = \frac{bh^3}{12}$ with b, the beam width (4 mm) and h, the beam thickness (0.5 mm).

To allow for characterizing the sensitivity of the Bragg grating to strain in traction and compression, the beam can be flipped so the Bragg grating is in the opposite direction from the neutral axis.

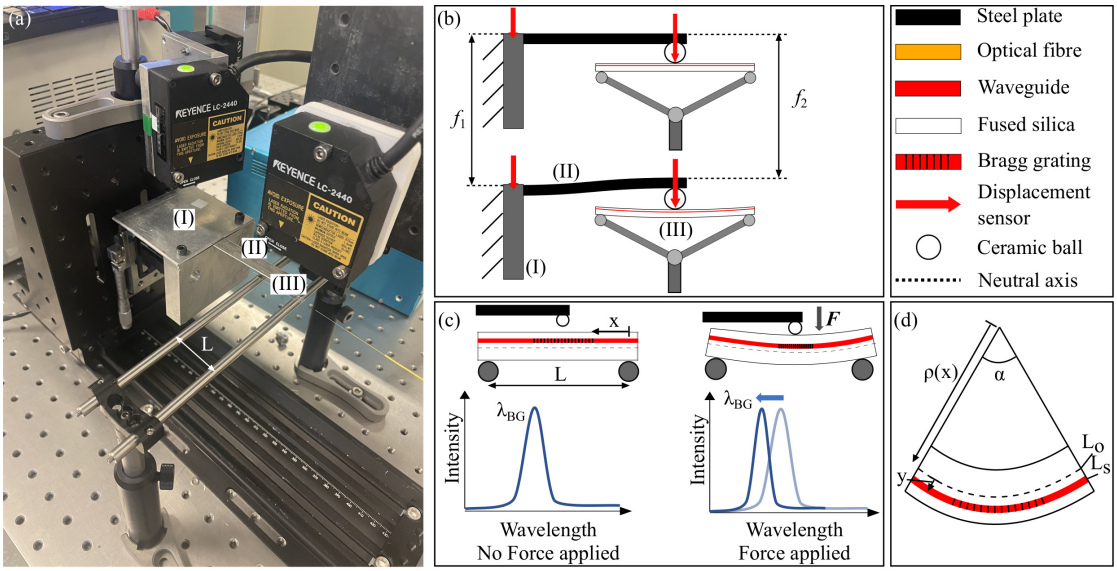

Figure 5.17: (**a**) Three-point flexural test bench. (**b**) A stainless steel beam with a ceramic ball loads the glass test beam. Two displacement sensors are used to monitor the stainless steel clamped side displacement f_1 and its ball end displacement f_2. (**c**) The test beam is placed on two fixed rods. The load is applied from the top at the centre of the beam. The Bragg grating sensor is placed close to the top surface of the beam, the applied strain is in compression. Therefore, the Bragg grating wavelength shift is negative. (**d**) It is a close view of the centre of the beam showing where the Bragg grating is inscribed.

Cantilever beam In this experiment detailed in Figure 5.18, the load is applied at the tip of the cantilever beam. The beam is horizontal and clamped on one side. The bending moment can be expressed as:

$$M(x) = F(L-x) \qquad x \in [0;L] \tag{5.14}$$

with F, the loading at the tip of the beam, x, the position from the clamp and L, the distance between the clamp and the position where the load is applied.

The loading is applied in the same way as the three-point flexural test. To allow for characterizing the sensitivity of the Bragg grating to strain in traction and compression, the beam can be returned so the Bragg grating is in the opposite direction from the neutral axis. The Bragg grating is located close to the clamp position ($x = 0$) at a distance y from the neutral axis (83 µm). Its length being much small than L (~ 24 mm), we can assume:

$$\epsilon = \frac{K_{fF} L y}{EI}(f_1 - f_2) \tag{5.15}$$

with I, the inertia of the considered beam section, $I = \frac{bh^3}{12}$ with b, the beam width (4 mm) and h, the beam thickness (0.5 mm).

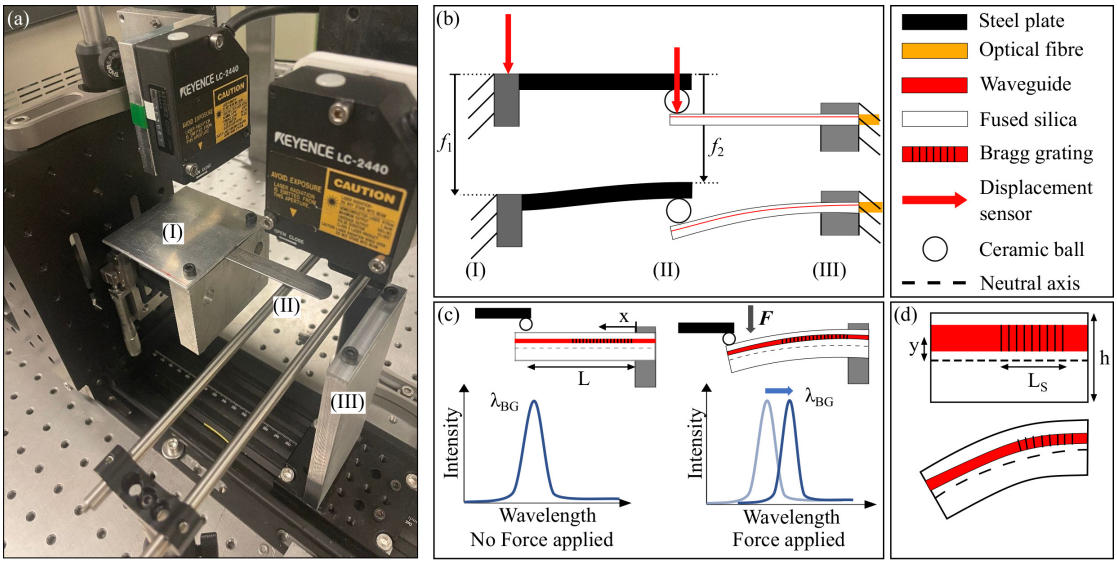

Figure 5.18: (**a**) Glass cantilever beam test bench. (**b**) A stainless steel beam with a ceramic ball loads the glass test beam. Two displacement sensors are used to monitor the stainless steel clamped side displacement f_1 and its ball end displacement f_2. (**c**) The test beam is clamped on the optical fibre side. The load is applied from the top at the tip of the cantilever beam. The Bragg grating sensor is placed close to the top surface of the beam, and the applied strain is in compression. Therefore, the Bragg grating wavelength shift is negative. (**d**) It is a close view of the beam showing where the Bragg grating is inscribed close to the beam clamp position.

Flexure pivot joint lever In this experiment detailed in Figure 5.19, the load is applied at a distance r from the centre of the pivot on a needle on the free end of the flexure joint. This pivot is a cross-spring hinge. It is composed of 3 beams of length L. The central beam has a width of b. The other two beams are perpendicular to the central one and have a width of $b/2$. The Bragg grating is written along the whole length of the centre beam at a distance y from its neutral axis. The lever arm r being much larger than the beam length, the bending moment along the beam can be considered constant. Therefore, the radius of curvature can be expressed as $\rho = L/\alpha$, α being the bending angle, and the strain as:

$$\epsilon = \frac{\Delta L}{L} = \frac{\alpha\rho - \alpha(\rho + y)}{\alpha\rho} = \frac{y}{\rho} = \frac{y}{L}\alpha \tag{5.16}$$

The pin used to load the specimen is a leg of a through-hole electronic component attached to a translation stage perpendicular to the needle at its rest position. To characterise the sensitivity of the Bragg grating to strain in traction and compression, the pin can push or pull the needle. The bending angle can be expressed as:

$$\alpha \approx \tan\alpha \approx \frac{d}{r} \tag{5.17}$$

with d, the displacement of the translation stage. r value is calibrated using the graduation on the fixed part of the specimen close to the tip of the needle. d is measured using a laser displacement sensor Keyence LK-H022 placed in front of the translation stage. The data are recorded using an NI USB-6002 analogic input connected to a laptop with a dedicated LabVIEW platform. The Bragg grating reflected spectrum is recorded synchronously with the same LabVIEW platform using a serial ethernet connection.

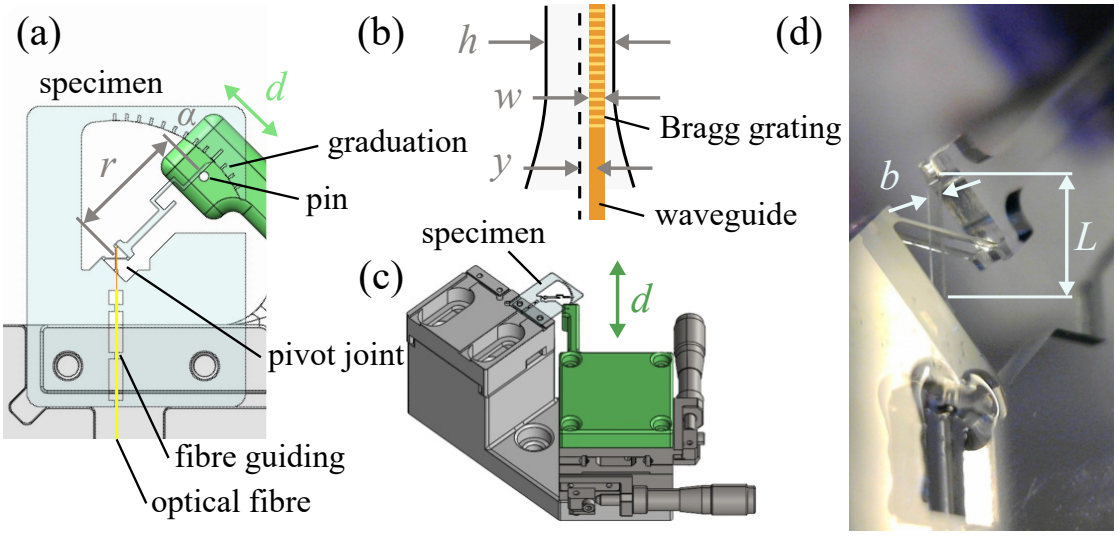

Figure 5.19: (**a**) Flexure specimen containing a cross-spring pivot hinge which has a needle being part of its moving end. A pin is applied perpendicular to the needle at a distance r from the pivot's centre. The graduation monitors the bending angle α. (**b**) The Bragg grating is included in a waveguide of width w and is placed at a distance y from the neutral axis of the central beam. The beam has a thickness of h. (**c**) The specimen is placed on a test bench such as the pin facing the needle. The needle is pushed by the pin by moving the translation stage manually. The displacement of the pin is expressed as d. (**d**) The close view represents the glass pivot joint lever. Its central beam has a width $b = 200$ µm and a length $L = 1.5$ mm.

5.5.1 Results

The sensitivity characterization experiments of the Bragg grating of our different setups are reported in Figure 5.20. Depending on the experiment, the strain testing range is different. It was chosen for each to limit the probability of breakage. The characterized sensitivities of the Bragg grating of the three designs are in good agreement with the theoretical sensitivity (1.24 pm/µε). The sensor manufacturing is therefore validated and further tests can be organized in different configurations and various environments depending on the application.

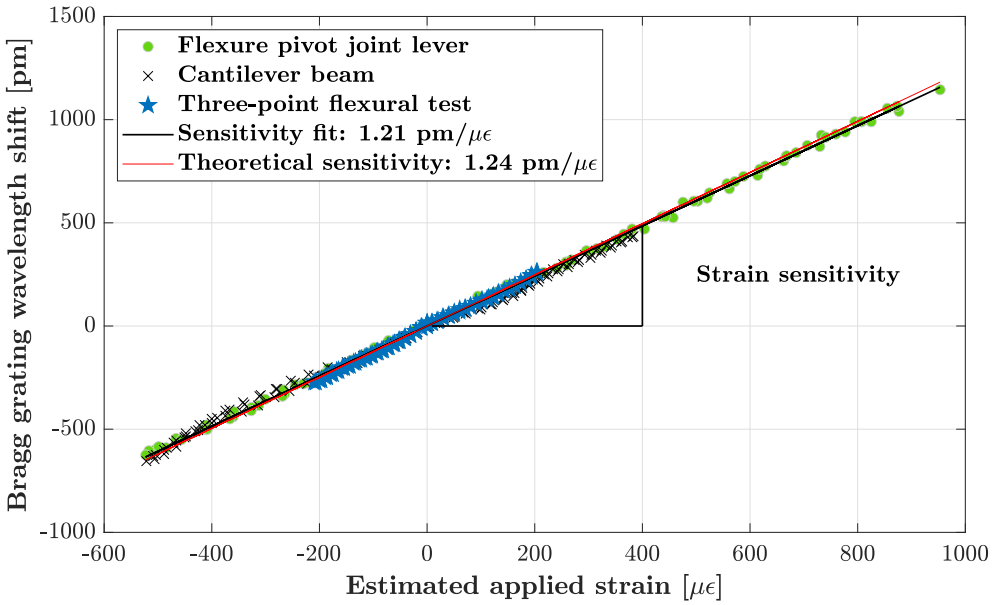

Figure 5.20: Results of the characterized Bragg grating sensitivity to strain for the three specimen designs that are detailed in Figures 5.17,5.18,5.19. Each experiment has been performed 4 times. The standard deviation of the experiments from the linear fit is 10 με.

5.5.2 Discussion

This study has demonstrated a method to design instrumented glass structures. In terms of application, it can improve the solutions where a fibre Bragg grating sensor needs to be integrated into a structure. The possibility to write the sensor inside the structure allows to reduce the size of the sensitive structure, and thus, its stiffness. It is also a gain in terms of production and assembly complexity as the sensor is fully monolithic. Besides this application, it is now also possible to instrument existing glass flexure mechanisms such as the constant-force surgical tool presented by Tissot-Daguette et al. [81]. It would enable estimating the displacement of the tip of the tool through the instrument.

As an example of a force sensor, our structure presented in Figure 5.19 can be used. By the bending angle Bragg grating strain relationship from Equation 5.16 ($\alpha = \frac{L}{y}\epsilon$), a force measured perpendicularly to the needle at its tip (at r = 10 mm) can be estimated as:

$$F = \frac{M}{r} = \frac{K_{\alpha \mathrm{M}}\alpha}{r} = \frac{Ebh^3}{6ry}\epsilon \tag{5.18}$$

with M, the bending moment of the pivot joint and $K_{\alpha \mathrm{M}} = \frac{Ebh^3}{6L}$, its bending stiffness with b, the width of the central beam (200 μm), the other two beams have both a width of $b/2$ and h, the thickness of the beam (50 μm).

From the theoretical strain sensitivity of the Bragg grating $\frac{\epsilon}{\Delta\lambda_{BG}}$ = 1.24 pm/$\mu\epsilon$, the force sensitivity can be expressed as:

$$\frac{F}{\Delta\lambda_{BG}} = \frac{Ebh^3}{6ry}\frac{\epsilon}{\Delta\lambda_{BG}} = 2.4\ \mu\text{N/pm} \tag{5.19}$$

Considering that the resolution of our optical spectrum analyzer is $\Delta\lambda_{BG,min}$ = 5 pm, the force resolution of this sensor could reach ΔF_{min} = 12 μN. By taking into account the standard deviation of the experiment, the force resolution is limited to ΔF_{min} = 30 μN. It is close to the theoretical limit of the spectrum analyzer. To improve this resolution, the Bragg grating can be placed closer to the surface of the beam. Being 10 μm width, and by placing it at 5 μm from the surface instead of 10 μm, its position from the centre y could be increased by a factor of 1.5. Also, it is possible to select an optical spectrum analyzer with a better wavelength resolution (existing down to 1 fm). By taking into account the fused silica strength (> 1 GPa), the force measurement range is > 10 mN. This sensor has three orders of magnitudes between its measurement range and its resolution.

Further studies that could validate this sensor technology for industrial application need to focus on the use and characterization of this type of sensor in harsh environments such as in water and with temperature gradients. The decoupling of the temperature and strain sensitivities is then the point of interest of these studies.

5.6 Torsion Characterization Perspective

Torsion characterization has not been executed in this work. An experiment considering the previous lessons learned is proposed. A Bragg grating sensor could be used to monitor torsion in a structure. Let's consider a square cross-section beam as in figure 5.21. To maximize the measurement sensitivity, the waveguide containing the Bragg grating should be helicoidal along the neutral axis of the beam and with the helix as close as possible to the surface with as many turns as possible. Unfortunately, we are not able to manufacture a waveguide with a curvature. Then, we propose to place the waveguide diagonally with the largest angle possible and as close to the surface as possible like in figure 5.21. When torsion is applied to the beam, the length L of the waveguide containing the Bragg grating varies. So, the period of the Bragg grating varies and it may be possible to monitor a wavelength shift using the OSA.

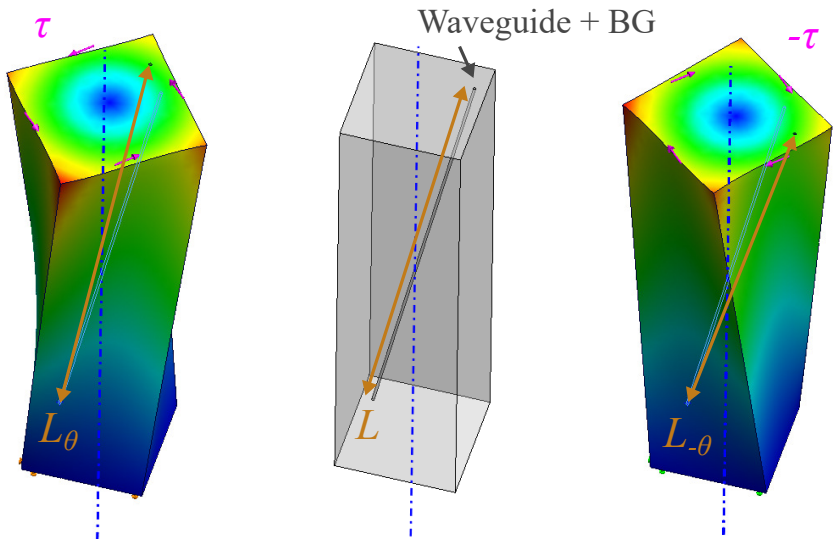

Figure 5.21: Simulation of a square cross-section beam in torsion containing a waveguide with a Bragg Grating along its length.

A test bench is proposed and has been manufactured (figure 5.22. The torsion is applied using a translation manual stage. The translation is then converted to rotation centred on the neutral axis of the mounted specimen using a flexure mechanism. The mount containing the compliant mechanism is monolithic and 3D printed in PLA. The displacement can be recorded using a laser displacement sensor Keyence LK-H022. So, the displacement measurement can be synchronized with the Bragg grating wavelength shift measurement through the same LabVIEW platform used in the previous experiments.

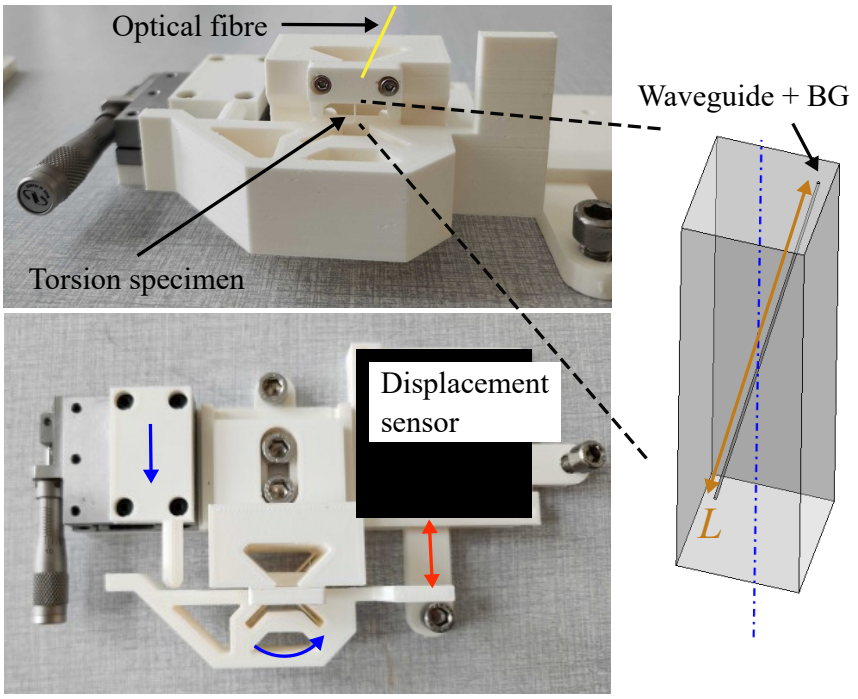

Figure 5.22: Test bench proposed to analyze if torsion can be monitored using a Bragg grating sensor inscribed inside a fused silica square cross-section beam.

5.7 Conclusion

To the best of our knowledge, instrumenting a glass flexure with an inscribed Bragg grating sensor was demonstrated for the first time. The same femtosecond laser has been used to manufacture the monolithic mechanism and the sensor. The correlation of our Bragg grating sensors' strain sensitivity with the theoretical sensitivity validates our designs and the manufacturing method. This technology is then available to instrument glass mechanisms.

The next step is to assess the operating range of such kinds of sensors according to the outstanding properties of fused silica glass.

6 Bragg Grating Sensors Perspectives for Application Opportunities

Benefiting from the biocompatibility of fused silica, femtosecond laser-assisted etching can be used to manufacture surgical instruments as [94] and [81]. Furthermore, as explained in Chapter 5, Bragg grating sensors can be inscribed in flexible structures. So, the surgical instrument manufactured by femtosecond laser-assisted etching can be instrumented. For example, the force applied by a surgical tool on the tissues could be monitored.

This chapter opens the perspective to using instrumented flexible glass structures for the design of medical tools. First, section 6.1 presents two environmental conditions encountered by the device: liquid water and temperature gradients. Then, section 6.2 discusses the possibility of engraving an instrumented flexible glass structure in a multimode optical fibre that could be inserted into a catheter.

6.1 Bragg Grating Sensor Environmental Conditions

This section studies the impact of liquid water and temperature gradients on the bending flexure specimen presented in Chapter 5.

6.1.1 Operation in Liquid Water

To assume that water does not influence the Bragg grating sensitivity of our proposed specimens, an experiment is defined to verify this assumption. The test bench presented in figure 5.19 is modified such that the specimen can be placed underwater (figure 6.1). Then, the experiment is performed like the "Flexure pivot joint lever" experiment described in Section 5.

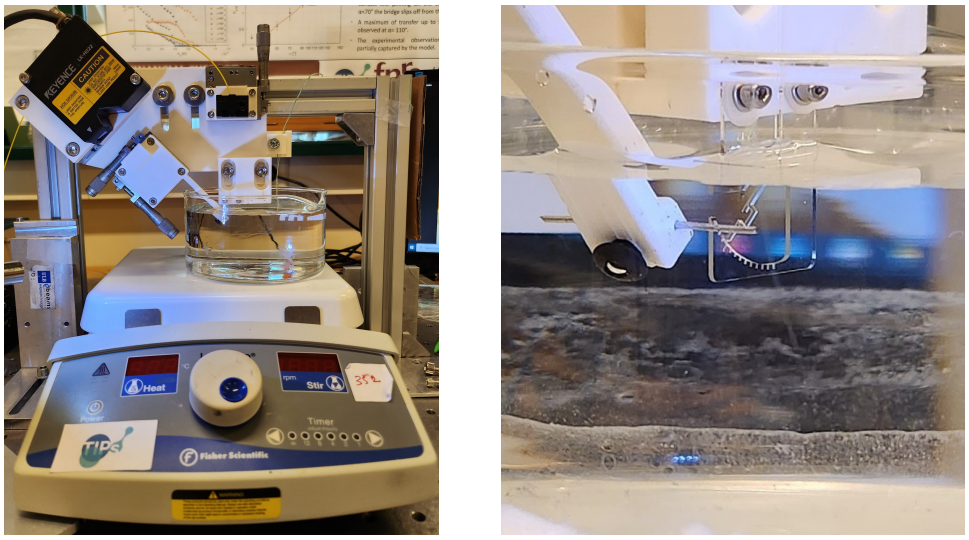

Figure 6.1: Test bench to characterize the Bragg Grating bending specimens inside water. In the left picture, a water recipient is placed on a heating plate to analyze the specimens with temperature gradients. In the right picture, is a view of the Bragg Grating bending specimen inside water.

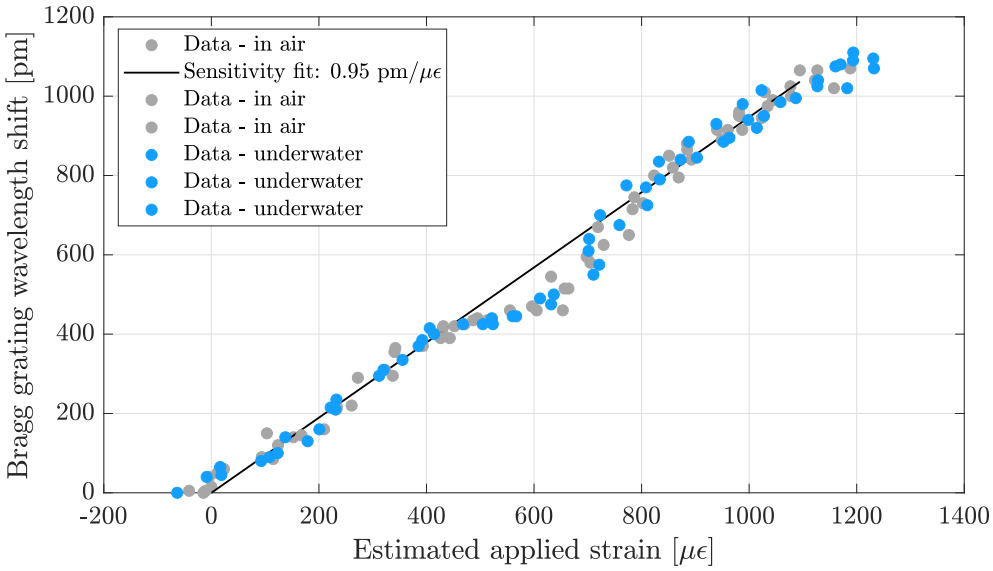

Figure 6.2: Results of the characterized Bragg grating sensitivity to strain for the specimen placed on the test bench described in figures 6.1. The experiment was performed 3 times in the air and 3 times underwater.

Results Figure 6.2 shows the result of the Bragg grating bending sensitivity in air and underwater using the test bench described in figure 6.1. The assumption that the water does not influence the sensitivity is verified. The data obtained in the air correlates with the data

obtained underwater. The sensitivity of 0.95 pm/με is lower than the expected sensitivity of 1.2 pm/με obtained with the other experiments in 5. No explanation is available yet.

A bump is visible in the centre of the plot. This effect occurs due to post-processing issues when the contrast of the reflectivity spectrum is not optimum. This could be affected by the coupling between the optical fibre and the waveguide of the specimen. In figure 6.3, the spectrum above the average noise threshold for the Bragg grating strain of 724 με is wider than the others. This is a problem because the algorithm presented in figure 5.13 uses a window to prevent taking noise into account. This has to be further investigated. Note that the power also decreases more than with the specimen in figure 5.12 when the applied strain increases.

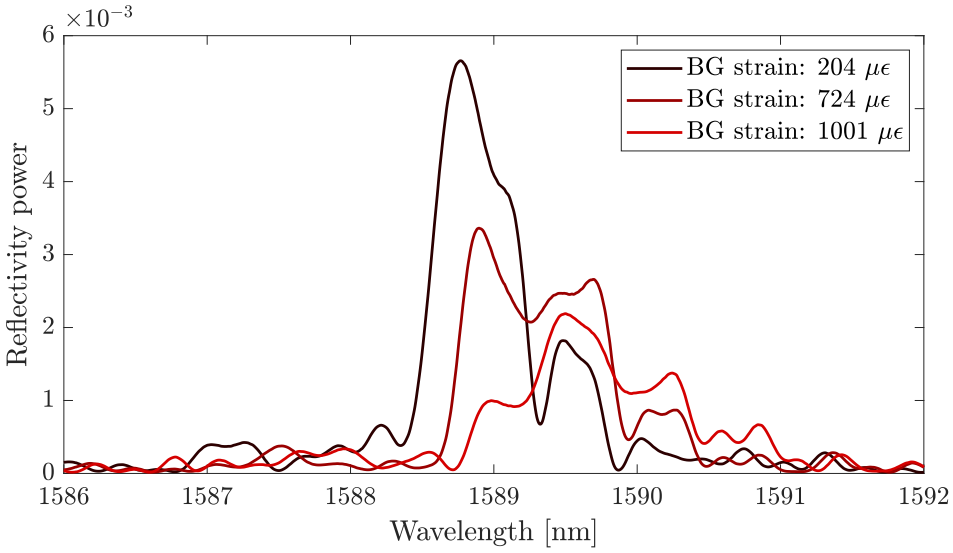

Figure 6.3: 3 Reflectivity power spectrum of the specimen for 3 different strain states. The state at 724 με being in the bump in figure 6.2, due to post-processing issues, is compared to other states.

6.1.2 Operation with Temperature Gradients

As presented in the State of The Art through equation 2.1, Bragg gratings are sensitive to mechanical axial strain and temperature gradients. As an example of an application for surgery, the instrument's temperature fluctuates between the room's temperature and the body's temperature. Then, if an instrument like the one described in [81] contains a Bragg grating to monitor the force applied by the instrument, the Bragg grating could be subject to a temperature gradient of about 20 °C. Matéo Tunon de Lara experimented to quantify the sensitivity to the temperature gradient of such a Bragg grating (figure 6.4). Considering the obtained sensitivity of 10.5 pm/°C, the wavelength shift caused by the temperature gradient could attain about 210 pm. This value could be taken into account as a security margin in designing the instrument. However, compensating for this effect could improve the precision of the force sensing.

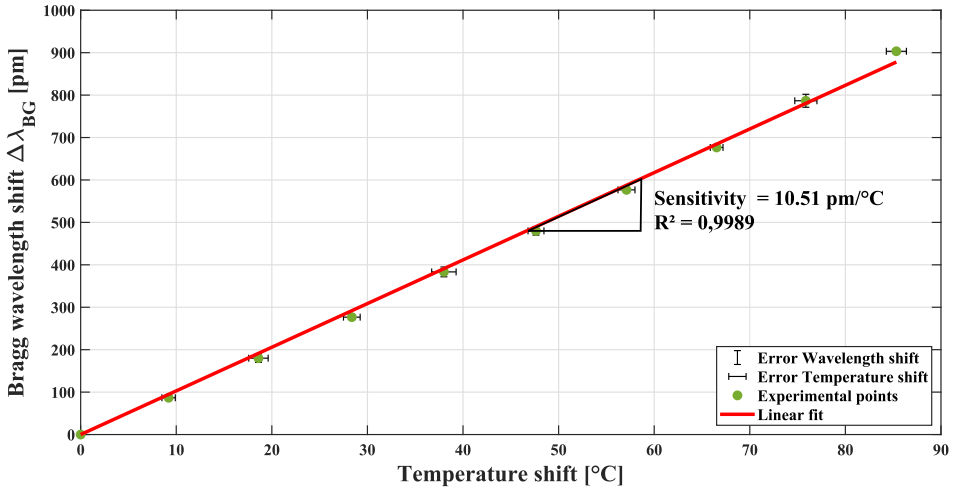

Figure 6.4: Temperature gradient sensibility characteristics of a Bragg grating inscribed with a femtosecond laser in a fused silica planar substrate heated using a Peltier module driven using a thermocouple.

Method The test bench described in figure 6.1 is used to test the temperature compensation. The device is operated underwater using the manual pin actuator to push the needle. The operation principle is the same as the test bench described in figure 5.19 The water is heated during the experiment using a Fisher Scientific heating plate. The temperature is recorded through the thermocouple placed under water. The temperature value is extracted using the thermocouple module NI USB-TC01. The sensibility obtained in the experiment reported in figure 6.4 is used to compensate for the Bragg grating wavelength shift caused by the temperature gradient. The compensation is performed on the LabVIEW platform which extracts the Bragg grating reflectivity spectrum through the OSA and the temperature through the thermocouple simultaneously.

Discussion Unfortunately, the Bragg grating reflectivity wavelength shift measured was not coherent with the pin actuator displacement. Different issues were identified. First, the experiment was not quick enough to perform measurements before the plastic mounts were deformed due to the heat. Then, for this experiment, manufacturing metallic mounts are required. Also, the quality of the coupling between the optical fibre and the specimen was degrading. The optical fibre must be glued with heat-resistant glue to the specimen to prevent any movement of the fibre during the experiment.
The following procedure would be to include the temperature sensing in the specimen. For that purpose, a second Bragg grating can be added along the waveguide of the specimen. Matéo Tunon de Lara showed that two Bragg gratings can be inscribed using the femtosecond laser and monitored through the specimen waveguide reflectivity spectrum (figure 6.5). Figure 6.6 shows an example where this Bragg grating can be placed to be sensitive only to the

temperature gradient. By subtracting the wavelength shift obtained through the static Bragg grating from the bent Bragg grating, the mechanical strain can be isolated.

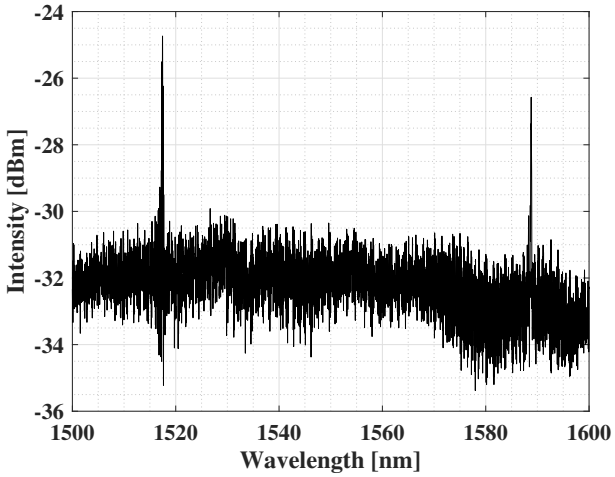

Figure 6.5: Reflectivity spectrum of the waveguide inscribed with a femtosecond laser in a fused silica planar substrate including two Bragg grating inscribed with two different periods.

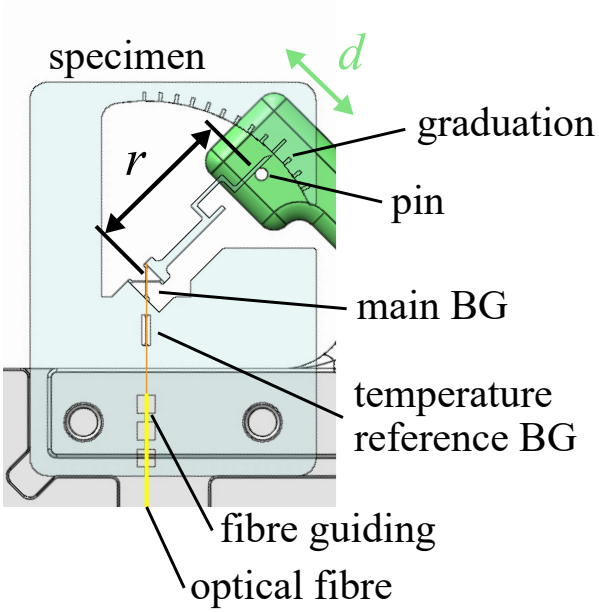

Figure 6.6: Flexure bending specimen scheme containing a Bragg grating sensitive to mechanical deformation and temperature gradients and a second Bragg grating sensitive only to the temperature gradients

6.2 Optical Fibre Mechanical Sensor

Accurate force measurement plays a vital role in numerous medical scenarios. Detecting cancers in critical access areas like the lungs, prostate, or brain during their early stages significantly enhances the effectiveness of therapy. Research indicates that healthy and tumorous tissues exhibit distinct mechanical responses, highlighting the potential for discrimination. However, there's a scarcity of techniques suitable for integration into the operating channels of endoscopes or bronchoscopes for real-time, in vivo diagnosis. Additionally, there's a demand for a force measurement tool that can be safely inserted into the middle ear.
Therefore, a prototype of an instrumented flexible structure at the tip of an optical fibre is proposed in figure 6.7. It eases the device assembly preventing the coupling issues between the optical fibre and the specimen. Furthermore, to benefit from the industrial quality of the optical fibre, the sensor can be designed such that the Bragg grating can be inscribed directly into the optical fibre waveguide or core. A prototype to study this method is presented in figure 6.7. By considering the bending of the beam under the force F, this force can be monitored through the wavelength shift of the reflected Bragg grating spectrum, using equation 5.1 and the sensitivity obtained in figure 5.20:

$$F = \frac{Ebh^3}{12ry} \frac{\epsilon}{\Delta\lambda_{\mathrm{BG}}} \Delta\lambda_{\mathrm{BG}} \tag{6.1}$$

with E, the Young modulus of fused silica (72 GPa), b, approximately the diameter of the optical fibre, h, the thickness of the beam, r, the distance between the centre of the beam (its neutral axis) and the parallel axis at the tip of the fibre where the force F is applied, y, the position of the centre of the Bragg grating sensor from the neutral axis and $\Delta\lambda_{\mathrm{BG}}$, the Bragg grating wavelength shift that can be measured using an Optical Spectrum Analyzer (OSA). So, the force resolution highly depends on the selected cantilever beam thickness h.

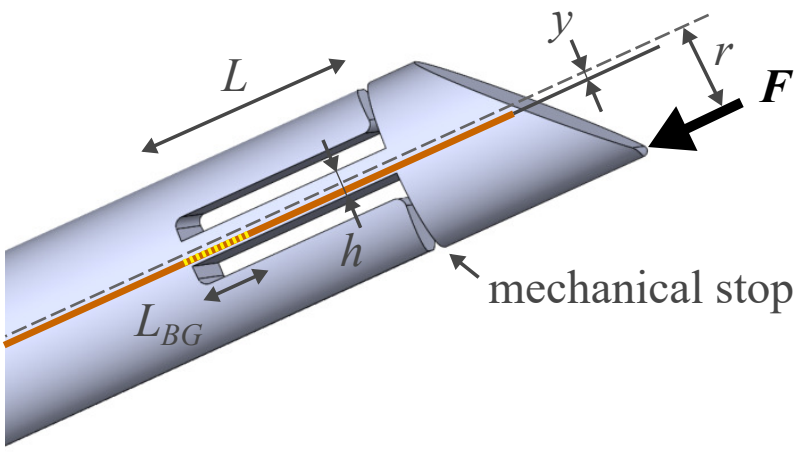

Figure 6.7: Instrumented flexible glass structure at the tip of an optical fibre.

6.2.1 Manufacturing

To perform the structure manufacturing at the tip of the optical fibre, a fibre mount is designed that can be mounted in the Femtoprint machine. To do so, a V-groove and a hole are manufactured through femtosecond laser-assisted etching on a 2 mm fused silica plate. So, the fibre can be placed in the V-groove of the plate and fixed using tape (figure 6.8). Finally, the structure is manufactured through femtosecond laser-assisted etching. As a new project recently proposed would benefit from large-diameter optical fibre etching, a multimode optical fibre of 400 µm diameter is selected. The toolpath to obtain the design presented in figure 6.7 is then defined.

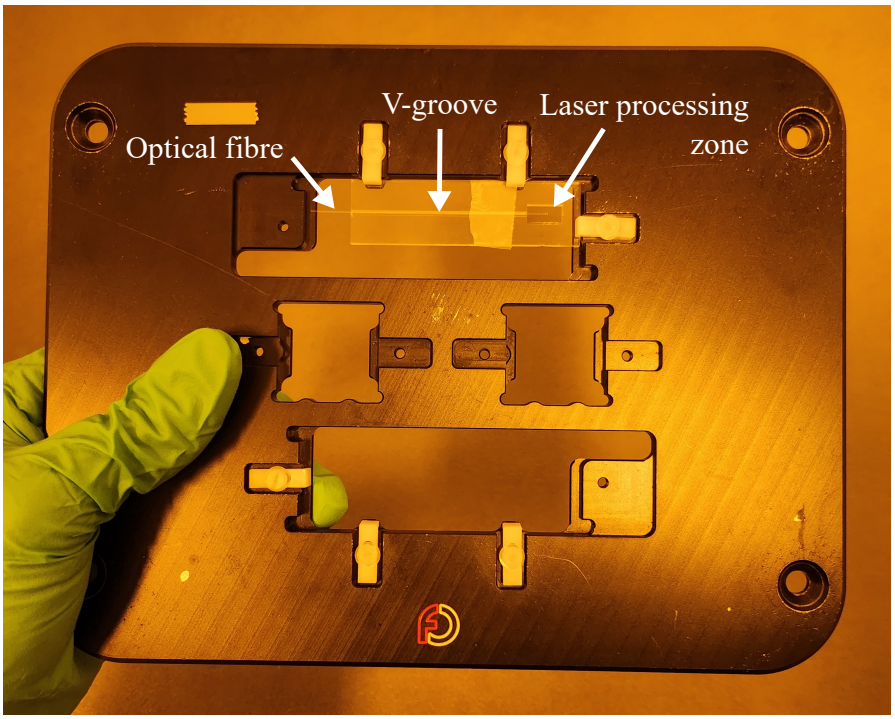

Figure 6.8: Fibre Bragg Grating sensor mount. The multimode optical fibre is placed on a custom fused silica mount containing a V-groove. This mount is then placed on the FEMTOprint mount for the femtosecond laser processing.

Results Unfortunately, the manufacturing was not a success. Figure 6.9 shows that only the centre of the fibre at its surface is etched. It could be explained by the fact a part of the laser light is reflected by the non-flat surface of the fibre. So, at its centre, the nanograting can be performed. And then, from a certain distance from the centre of the fibre, the tilt angle of the surface is too important and most of the laser energy is lost by reflection. An investigation is required to define if there could be a way to perform this etching on large-diameter fibres. In the meantime, this process could be tried on a smaller diameter fibre such as the conventional 125 µm diameter single-mode fibres.

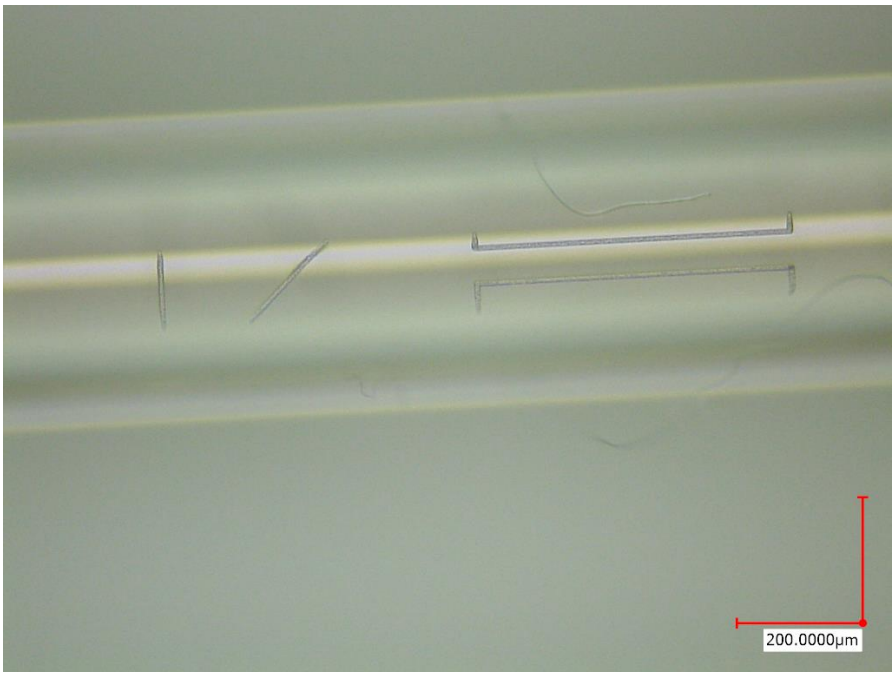

Figure 6.9: Fibre Bragg Grating sensor structure at the tip of an optical fibre. The structure was not etched completely. It was etched only at the surface of the fibre.

6.3 Conclusion

In this chapter, some perspectives to open our sensor technology for medical applications are presented. The use of our specimen underwater is validated. It shows the same bending strain sensitivity characteristics as in the air. An investigation to explain the variation of the sensitivity value that differs from the one found in 5 could be interesting. While the first test about the temperature compensation was not successful, it should be resolved by using heat-resistant materials such as Aluminum instead of 3D-printed PLA. Nevertheless, the manufacturing of structures in optical fibre needs extended investigation.

7 Conclusion

Flexible Glass Structure Manufacturing Our laboratory's new manufacturing technique, femtosecond laser-assisted wet etching, enables the production of diverse flexible structures from glass. With this process, we can create complex three-dimensional monolithic structures with thicknesses as small as 10 µm. In terms of vertical axis machining, almost all structures obtained in this work were straight-angle shaped. Thanks to the recent software update that facilitates the manufacturing of curve-shaped structures, more complex structures were realized. The first contribution is the funnel manufacturing for the optical fibre insertion for the Bragg grating sensors. An attempt to manufacture a transverse cross-spring hinge joint was executed. This could allow new options for inertial sensor design or other large structures. The machining range being limited vertically, the orientation of the flexure elements in the thickest substrate (5 mm) is critical to widen the monolithic design possibilities. The attempt is not a success yet, it is a matter of continuous understanding and experimentation on the process that will succeed.

Fused Silica Bending Strength at the Micro-Scale For flexure specimens at the micro-scale, the experiments demonstrated that a maximum bending stress of 1 GPa can be considered for conception. The bending strength of fused silica specimens has been estimated, yielding a maximum stress of 2.6 GPa. While the executed annealing attempts did not show improvement in the bending strength, this approach should still be studied. The proper annealing recipe has not been found yet. The only attempt that showed results was the one with a 4h step at 1200 °C. The result was only visual. As the monolithic structure was deformed, trying a shorter step at this temperature could be an option. Also, increasing the length of the step at a lower temperature could be considered.

Thermoelastic Damping of Fused Silica Ring-down experiments were conducted on resonators utilizing fused silica flexure joints to evaluate the internal damping properties, as fused silica is known for its low-damping behaviour. Two separate experiments were carried out. The first examined a micro-scale monolithic resonator and revealed that the quality factor

was constrained by the air pressure in the vacuum tank, with an estimated quality factor of approximately 185'000 at a pressure of 2×10^{-3} mbar. The second experiment focused on an aluminium pendulum suspended on a fused silica flexure joint, where the quality factor was limited to about 25'000 at pressures below 1 mbar. Unfortunately, none of these experiments allowed us to quantify the thermoelastic damping in fused silica. However, the first experiment is encouraging since the quality factor follows the model and is not saturating. To continue the experiment, a test bench at a lower pressure than 10^{-3} mbar shall be designed. This experiment can be carried out in the vacuum chamber at the Precision Mechatronics Laboratory, the one used for the second experiment with the Aluminum pendulum. An actuator shall be installed in the chamber to excite the resonator to start the ring-down measurement. This vacuum test bench can be maintained at a pressure lower than 10^{-5} mbar. Concerning the second experiment, further investigation should be followed to explain the saturation below 1 mbar. Tilting the pendulum and even testing it horizontally could be considered. This would permit us to study if gravity influences the damping characteristics.

Vertical Inertial Sensor Mechanics The mechanisms for two distinct vertical inertial sensors were designed and manufactured. The first sensor has its natural resonance frequency at 2.8 Hz and fits within a $10 \times 10 \times 10$ cm³ box, while the second, larger sensor has its natural frequency at 1.2 Hz and allows for adjustable orientation of its readout. The second sensor also has a simpler assembly, with some detachable parts that don't require full disassembly. The first sensor is mounted with fused silica flexure joints demonstrating that glass flexure joints can be combined with aluminium and stainless steel components, though their assembly can be challenging. As a backup for robustness, other flexure parts were proposed using different materials, such as Copper-Beryllium or Titanium. An optimization experiment was conducted to determine the ideal dimensions for these flexure joints based on the first sensor proof mass hinge joint. The open-loop transfer function of the first sensor was compared to a reference sensor, the Guralp GS13, showing good coherence in the frequency range between 200 mHz and 100 Hz. The astatic leaf-spring suspension, used to hang the proof mass, underwent experimental optimization. The results indicate that, given a constant inertia for the proof mass and a fixed length for the leaf-spring suspension, the location of the clamping points affects the natural resonance frequency of the mechanism. To minimize this resonance, the clamping points should be placed as low as possible relative to the hinge of the proof mass. The perspective for future inertial sensor mechanics design could be to benefit from the fused silica properties. So, designing a full-glass monolithic sensor could be considered. To do that, first, the experiment about thermoelastic damping assessment of fused silica must be completed. This would allow assessing what gain of performance can be considered using fused silica. Then, the flexible glass structure manufacturing process should be further mastered. This will prevent to discarding of original complex ideas at the beginning of the conception of a new sensor.

Monolithic Structure Instrumented by Bragg Grating Sensor Bragg grating sensors were inscribed into flexure specimens and their sensitivity was evaluated through tensile and bending experiments. The sensitivity of these sensors was compared to theoretical predictions, yielding a sensitivity of approximately 1.2 picometers per microstrain (pm/με), with a standard deviation of around 10 picometers, limited by the optical spectrum analyzer's accuracy. The Bragg grating wavelength was determined by analyzing the centroid of the reflected light spectrum. This type of sensor was demonstrated in a 50 µm thickness flexure. This thickness being half smaller than a single-mode optical fibre (125 µm diameter), showed the integration opportunity of such a sensor. Also, thanks to the three-axis machining of the FEMTOprint, this sensor technology is versatile regarding the placement of the Bragg grating. This sensor technology can now be used for the conception of monolithic glass instruments.

Application Perspectives for Bragg Grating Sensors A Bragg grating sensor was tested both in the air and underwater, showing no detectable variation in performance. A method was proposed to compensate for the temperature gradient effects on Bragg grating sensors. However, the test bench required to perform comprehensive characterization is not yet ready. Further work is required to build the test bench and perform the assessment of the temperature compensation during a deformation measurement. Then, to guarantee the robustness of the sensor, an investigation should be planned to define the proper optical fibre fixation method. As the coupling between the optical fibre and the waveguide in the specimen containing the Bragg grating is critical when the Bragg grating contrast is larger than 10 dBm, the optical fibre must be fixed to maintain the performance during operation. For the experiments, a fibre clamp was used. Then, it could be glued if suitable for the application. Otherwise, a clamping mechanism or another fixation must be designed.

Bibliography

[1] Loïc Amez-Droz et al. “Instrumented Flexible Glass Structure: A Bragg Grating Inscribed with Femtosecond Laser Used as a Bending Sensor”. In: *Sensors* 23.19 (2023), p. 8018. ISSN: 1424-8220.

[2] Anthony Amorosi et al. “High resolution compact vertical inertial sensor for atomic quantum gravimeter hybridization”. In: *ISMA-USD Noise and Vibration Engineering Conference*. 2022.

[3] Christos-Edward Athanasiou and Yves Bellouard. “A monolithic micro-tensile tester for investigating silicon dioxide polymorph micromechanics, fabricated and operated using a femtosecond laser”. In: *Micromachines* 6.9 (2015), pp. 1365–1386.

[4] Christos-Edward Athanasiou and Yves Bellouard. “Investigation of the micro-mechanical properties of femtosecond laser-induced phases in amorphous silica”. In: *Frontiers in Ultrafast Optics: Biomedical, Scientific, and Industrial Applications XVI*. Vol. 9740. SPIE, pp. 176–182.

[5] Christos-Edward Athanasiou, Max-Olivier Hongler, and Yves Bellouard. “Unraveling brittle-fracture statistics from intermittent patterns formed during femtosecond laser exposure”. In: *Physical Review Applied* 8.5 (2017), p. 054013.

[6] Minhang Bao et al. “Energy transfer model for squeeze-film air damping in low vacuum”. In: *Journal of Micromechanics and Microengineering* 12.3 (2002), p. 341. ISSN: 0960-1317.

[7] Y Bellouard et al. “The femtoprint project”. In: *Journal of Laser Micro/Nanoengineering* 7.1 (2012), pp. 1–10.

[8] Yves Bellouard. “On the bending strength of fused silica flexures fabricated by ultrafast lasers”. In: *Optical Materials Express* 1.5 (2011), pp. 816–831. ISSN: 2159-3930.

[9] Yves Bellouard, Ali A Said, and Philippe Bado. “Integrating optics and micro-mechanics in a single substrate: a step toward monolithic integration in fused silica”. In: *Optics Express* 13.17 (2005), pp. 6635–6644. ISSN: 1094-4087.

[10] Yves Bellouard et al. “Fabrication of high-aspect ratio, micro-fluidic channels and tunnels using femtosecond laser pulses and chemical etching”. In: *Optics Express* 12.10 (2004), pp. 2120–2129. ISSN: 1094-4087.

[11] Martynas Beresna, Mindaugas Gecevičius, and Peter G Kazansky. "Ultrafast laser direct writing and nanostructuring in transparent materials". In: *Advances in Optics and Photonics* 6.3 (2014), pp. 293–339.

[12] Martynas Beresna and Peter G Kazansky. "Polarization diffraction grating produced by femtosecond laser nanostructuring in glass". In: *Optics letters* 35.10 (2010), pp. 1662–1664. ISSN: 1539-4794.

[13] Alessandro Bertolini et al. "Geometric anti-spring vertical accelerometers for seismic monitoring". In: *Nuclear Instruments and Methods in Physics Research Section A: Accelerators, Spectrometers, Detectors and Associated Equipment* 518.1-2 (2004), pp. 233–235. ISSN: 0168-9002.

[14] Stefano Bianco et al. "Silicon resonant microcantilevers for absolute pressure measurement". In: *Journal of Vacuum Science & Technology B: Microelectronics and Nanometer Structures Processing, Measurement, and Phenomena* 24.4 (2006), pp. 1803–1809. ISSN: 1071-1023.

[15] Q. Bodart et al. "A cold atom pyramidal gravimeter with a single laser beam". In: *Applied Physics Letters* 96.13 (Mar. 2010), p. 134101. DOI: 10.1063/1.3373917.

[16] BA Boom. "Acceleration sensing at the nano-g level: Development and characterisation of low-noise microseismometers for next generation gravitational wave detectors". In: (2020).

[17] Carlo Edoardo Campanella et al. "Fibre Bragg grating based strain sensors: review of technology and applications". In: *Sensors* 18.9 (2018), p. 3115.

[18] J Canning et al. "Anatomy of a femtosecond laser processed silica waveguide". In: *Optical Materials Express* 1.5 (2011), pp. 998–1008.

[19] Enrico Casamenti, Sacha Pollonghini, and Yves Bellouard. "Few pulses femtosecond laser exposure for high efficiency 3D glass micromachining". In: *Optics Express* 29.22 (2021), pp. 35054–35066. ISSN: 1094-4087.

[20] Christophe Caucheteur. "Realization of mechanical and chemical sensors based on the fiber Bragg gratings technology". In: *PhD, Faculté polytechnique de Mons, Mons, Belgium* (2007).

[21] Karima Chah et al. "Femtosecond-laser-induced highly birefringent Bragg gratings in standard optical fiber". In: *Optics Letters* 38.4 (2013), pp. 594–596.

[22] Pierrick Cheiney et al. "Demonstration of a Robust Hybrid Classical/Quantum Accelerometer". In: *2019 IEEE International Symposium on Inertial Sensors and Systems (INERTIAL)*. IEEE, Apr. 2019. DOI: 10.1109/isiss.2019.8739762.

[23] RG Christian. "The theory of oscillating-vane vacuum gauges". In: *Vacuum* 16.4 (1966), pp. 175–178. ISSN: 0042-207X.

[24] C. Collette et al. "Prototype of interferometric absolute motion sensor". In: *Sensors and Actuators A: Physical* 224 (Apr. 2015), pp. 72–77. DOI: 10.1016/j.sna.2015.01.019.

[25] C. Collette et al. “Review: Inertial Sensors for Low-Frequency Seismic Vibration Measurement”. In: *Bulletin of the Seismological Society of America* 102.4 (Aug. 2012), pp. 1289–1300. DOI: 10.1785/0120110223.

[26] Christophe Collette, Stef Janssens, and Kurt Artoos. “Review of active vibration isolation strategies”. In: *Recent patents on Mechanical engineering* 4.3 (2011), pp. 212–219. ISSN: 2212-7976.

[27] Christophe Collette et al. “Prototype of interferometric absolute motion sensor”. In: *Sensors and Actuators A: Physical* 224 (2015), pp. 72–77. ISSN: 0924-4247.

[28] S J Cooper et al. “Interferometric sensing of a commercial geophone”. In: *Classical and Quantum Gravity* 39.7 (Mar. 2022), p. 075023. DOI: 10.1088/1361-6382/ac595c.

[29] Binlei Ding. “Development of High Resolution Interferometric Inertial Sensors ”. PhD thesis. Université Libre de Bruxelles, 2021.

[30] Rokas Drevinskas et al. “Tailored surface birefringence by femtosecond laser assisted wet etching”. In: *Optics Express* 23.2 (2015), pp. 1428–1437. ISSN: 1094-4087.

[31] Rafael R Gattass and Eric Mazur. “Femtosecond laser micromachining in transparent materials”. In: *Nature Photonics* 2.4 (2008), pp. 219–225.

[32] Wenbin Gong et al. “Effects and Prospects of the Vibration Isolation Methods for an Atomic Interference Gravimeter”. In: *Sensors* 22.2 (Jan. 2022), p. 583. DOI: 10.3390/s22020583.

[33] J. L. Gouët et al. “Limits to the sensitivity of a low noise compact atomic gravimeter”. In: *Applied Physics B* 92.2 (June 2008), pp. 133–144. DOI: 10.1007/s00340-008-3088-1.

[34] Zhili Hao, Ahmet Erbil, and Farrokh Ayazi. “An analytical model for support loss in micromachined beam resonators with in-plane flexural vibrations”. In: *Sensors and Actuators A: Physical* 109.1-2 (2003), pp. 156–164. ISSN: 0924-4247.

[35] J. V. van Heijningen, A. Bertolini, and J. F. J. van den Brand. “A novel interferometrically read out inertial sensor for future gravitational wave detectors”. In: *2018 IEEE Sensors Applications Symposium (SAS)*. IEEE, Mar. 2018. DOI: 10.1109/sas.2018.8336722.

[36] Sylvain Hellegouarch et al. “Linear encoder based low frequency inertial sensor”. In: *International Journal of Optomechatronics* 10.3-4 (2016), pp. 120–129. ISSN: 1559-9612.

[37] Simon Henein. *Conception des structures articulées à guidages flexibles de haute précision*. Report. EPFL, 2000.

[38] Cyril Hnatovsky et al. “Pulse duration dependence of femtosecond-laser-fabricated nanogratings in fused silica”. In: *Applied Physics Letters* 87.1 (2005), p. 014104. ISSN: 0003-6951.

[39] Hiroshi Hosaka, Kiyoshi Itao, and Susumu Kuroda. “Damping characteristics of beam-shaped micro-oscillators”. In: *Sensors and Actuators A: Physical* 49.1-2 (1995), pp. 87–95. ISSN: 0924-4247.

[40] Larry L Howell. *Compliant Mechanisms*. John Wiley & Sons, 2001. ISBN: 047138478X.

[41] YL Huang and Peter R Saulson. "Dissipation mechanisms in pendulums and their implications for gravitational wave interferometers". In: *Review of scientific instruments* 69.2 (1998), pp. 544–553. ISSN: 0034-6748.

[42] Nader A Issa. "High numerical aperture in multimode microstructured optical fibers". In: *Applied Optics* 43.33 (2004), pp. 6191–6197. ISSN: 2155-3165.

[43] Ajit P Joglekar et al. "A study of the deterministic character of optical damage by femtosecond laser pulses and applications to nanomachining". In: *Applied Physics B* 77.1 (2003), pp. 25–30.

[44] Raman Kashyap. *Fiber Bragg gratings*. Academic press, 2009.

[45] Peter G Kazansky et al. ""Quill" writing with ultrashort light pulses in transparent materials". In: *Applied physics letters* 90.15 (2007), p. 151120.

[46] S Kumar and MA Haque. "Reduction of thermo-elastic damping with a secondary elastic field". In: *Journal of sound and vibration* 318.3 (2008), pp. 423–427. ISSN: 0022-460X.

[47] Lucien Lacoste, Neal Clarkson, and George Hamilton. "LaCoste and Romberg stabilized platform shipboard gravity meter". In: *Geophysics* 32.1 (1967), pp. 99–109. ISSN: 0016-8033.

[48] Guillaume Laffont et al. "Temperature resistant fiber Bragg gratings for on-line and structural health monitoring of the next-generation of nuclear reactors". In: *Sensors* 18.6 (2018), p. 1791.

[49] J. Lautier et al. "Hybridizing matter-wave and classical accelerometers". In: *Applied Physics Letters* 105.14 (Oct. 2014), p. 144102. DOI: 10.1063/1.4897358.

[50] Bo Lenssen and Yves Bellouard. "Optically transparent glass micro-actuator fabricated by femtosecond laser exposure and chemical etching". In: *Applied Physics Letters* 101.10 (2012), p. 103503. ISSN: 0003-6951.

[51] Ron Lifshitz and Michael L Roukes. "Thermoelastic damping in micro-and nanomechanical systems". In: *Physical review B* 61.8 (2000), p. 5600.

[52] X Liu, D Du, and G Mourou. "Laser ablation and micromachining with ultrashort laser pulses". In: *IEEE Journal of Quantum Electronics* 33.10 (1997), pp. 1706–1716.

[53] Mangirdas Malinauskas et al. "Ultrafast laser processing of materials: from science to industry". In: *Light: Science & Applications* 5.8 (2016), e16133–e16133.

[54] Christian Martin et al. "Detrimental effect of alkaline impurities on fused silica crucible during multi-crystalline ingot growth". In: *Proceedings of the 3rd International Workshop on Crystalline Silicon Solar Cells (CSSC-3)*.

[55] Amos Martinez, Igor Y Khrushchev, and Ian Bennion. "Direct inscription of Bragg gratings in coated fibers by an infrared femtosecond laser". In: *Optics Letters* 31.11 (2006), pp. 1603–1605.

[56] Vincent Ménoret et al. “Gravity measurements below 10-9 g with a transportable absolute quantum gravimeter”. In: *Scientific Reports* 8.1 (Aug. 2018). DOI: 10.1038/s41598-018-30608-1.

[57] S Merlet et al. “Operating an atom interferometer beyond its linear range”. In: *Metrologia* 46.1 (Jan. 2009), pp. 87–94. DOI: 10.1088/0026-1394/46/1/011.

[58] Stephen J Mihailov et al. “Extreme environment sensing using femtosecond laser-inscribed fiber Bragg gratings”. In: *Sensors* 17.12 (2017), p. 2909.

[59] Douglas C Montgomery. *Design and analysis of experiments*. John wiley & sons, 2017. ISBN: 1119113474.

[60] Saood Ibni Nazir, Christos E. Athanasiou, and Yves Bellouard. “On the behavior of uniaxial static stress loaded micro-scale fused silica beams at room temperature”. In: *Journal of Non-Crystalline Solids: X* 14 (2022). ISSN: 25901591. DOI: 10.1016/j.nocx.2022.100083.

[61] Saood Ibni Nazir, Christos E. Athanasiou, and Yves Bellouard. “On the behavior of uniaxial static stress loaded micro-scale fused silica beams at room temperature”. In: *Journal of Non-Crystalline Solids: X* 14 (2022). ISSN: 25901591. DOI: 10.1016/j.nocx.2022.100083.

[62] Saood Ibni Nazir and Yves Bellouard. “Contactless Optical Packaging Concept for Laser to Fiber Coupling”. In: *IEEE Transactions on Components, Packaging and Manufacturing Technology* 11.6 (2021), pp. 1035–1043. ISSN: 2156-3950.

[63] Kenji Numata et al. “Intrinsic losses in various kinds of fused silica”. In: *Classical and Quantum Gravity* 19.7 (2002), p. 1697. ISSN: 0264-9381.

[64] AJJA Oome et al. “Modeling of an electromagnetic geophone with passive magnetic spring”. In: *Sensors and Actuators A: Physical* 153.2 (2009), pp. 142–154. ISSN: 0924-4247.

[65] Achim Peters, Keng Yeow Chung, and Steven Chu. “Measurement of gravitational acceleration by dropping atoms”. In: *Nature* 400.6747 (Aug. 1999), pp. 849–852. DOI: 10.1038/23655.

[66] Arunkrishnan Radhakrishnan et al. “Femtosecond laser-shockwave induced densification in fused silica”. In: *Optical Materials Express* 12.7 (2022), pp. 2886–2898. ISSN: 2159-3930.

[67] Sheeba Rajesh and Yves Bellouard. “Towards fast femtosecond laser micromachining of fused silica: The effect of deposited energy”. In: *Optics Express* 18.20 (2010), pp. 21490–21497. ISSN: 1094-4087.

[68] Sören Richter et al. “Nanogratings in fused silica: Formation, control, and applications”. In: *Journal of Laser Applications* 24.4 (2012), p. 042008. ISSN: 1042-346X.

[69] M Rosenberger et al. “Polymer planar Bragg grating sensor for static strain measurements”. In: *Optics letters* 38.5 (2013), pp. 772–774. ISSN: 1539-4794.

[70] Manuel Rosenberger, Bernhard Schmauss, and Ralf Hellmann. “UV-writing of a superstructure waveguide Bragg grating in a planar polymer substrate”. In: *Sensors* 17.9 (2017), p. 1964.

[71] Masaaki Sakakura et al. “Ultralow-loss geometric phase and polarization shaping by ultrafast laser writing in silica glass”. In: *Light: Science & Applications* 9.1 (2020), pp. 1–10.

[72] Peter R. Saulson. “Thermal noise in mechanical experiments”. In: *Physical Review D* 42.8 (Oct. 1990), pp. 2437–2445. DOI: 10.1103/physrevd.42.2437.

[73] Ameer Sider et al. “E-TEST prototype design report”. In: *arXiv preprint arXiv:2212.10083* (2022).

[74] Ameer Sider et al. “E-TEST: a compact low-frequency isolator for a large cryogenic mirror”. In: *Classical and Quantum Gravity* 40.16 (2023), p. 165002. ISSN: 0264-9381.

[75] Ik-Bu Sohn et al. “Laser assisted fabrication of micro-lens array and characterization of their beam shaping property”. In: *Applied Surface Science* 479 (2019), pp. 375–385.

[76] Dezhi Tan, Xiaoyu Sun, and Jianrong Qiu. “Femtosecond laser writing low-loss waveguides in silica glass: highly symmetrical mode field and mechanism of refractive index change”. In: *Optical Materials Express* 11.3 (2021), pp. 848–857.

[77] Antreas Theodosiou et al. “Plane-by-plane femtosecond laser inscription method for single-peak Bragg gratings in multimode CYTOP polymer optical fiber”. In: *Journal of Lightwave Technology* 35.24 (2017), pp. 5404–5410.

[78] Markus Thiel, Günter Flachenecker, and Wolfgang Schade. “Femtosecond laser writing of Bragg grating waveguide bundles in bulk glass”. In: *Optics Letters* 40.7 (2015), pp. 1266–1269.

[79] Viktor Tielen and Yves Bellouard. “Three-dimensional glass monolithic micro-flexure fabricated by femtosecond laser exposure and chemical etching”. In: *Micromachines* 5.3 (2014), pp. 697–710.

[80] An-Chun Tien et al. “Short-pulse laser damage in transparent materials as a function of pulse duration”. In: *Physical Review Letters* 82.19 (1999), p. 3883.

[81] Loïc Tissot-Daguette et al. “Design and modelling of a compliant constant-force surgical tool for objective assessment of ossicular chain mobility”. In: *2021 21st International Conference on Solid-State Sensors, Actuators and Microsystems (Transducers)*. IEEE, 2021, pp. 1299–1302. ISBN: 1665412674.

[82] Joseph T Toombs et al. “Volumetric additive manufacturing of silica glass with microscale computed axial lithography”. In: *Science* 376.6590 (2022), pp. 308–312. ISSN: 0036-8075.

[83] M Tunon de Lara et al. “Production of optical waveguide in planar glass substrate fabricated with femtoprint”. In: *Fiber Lasers and Glass Photonics: Materials through Applications III*. Vol. 12142. SPIE, 2022, pp. 371–378.

[84] Mateo Tunon de Lara et al. “Femtosecond pulse laser-engineered glass flexible structures instrumented with an in-built Bragg grating sensor”. In: *Optics Express* (2023). in press.

[85] Armin Saeedi Vahdat and Ghader Rezazadeh. “Effects of axial and residual stresses on thermoelastic damping in capacitive micro-beam resonators”. In: *Journal of the Franklin Institute* 348.4 (2011), pp. 622–639. ISSN: 0016-0032.

[86] Pieter Vlugter and Yves Bellouard. “Abnormal temperature dependent elastic properties of fused silica irradiated by ultrafast lasers”. In: *Physical Review Materials* 6.3 (2022), p. 033602.

[87] Xiaoduo Wang et al. “Femtosecond laser-based processing methods and their applications in optical device manufacturing: A review”. In: *Optics & Laser Technology* 135 (2021), p. 106687.

[88] Waloddi Weibull. “A statistical distribution function of wide applicability”. In: *Journal of applied mechanics* (1951).

[89] Remo N Widmer et al. “Smooth or not: Robust fused silica micro-components by femtosecond-laser-assisted etching”. In: *Materials & Design* 204 (2021), p. 109670. ISSN: 0264-1275.

[90] E Wielandt and G Streckeisen. “The leaf-spring seismometer: Design and performance”. In: *Bulletin of the Seismological Society of America* 72.6A (1982), pp. 2349–2367. ISSN: 1943-3573.

[91] Erhard Wielandt. “Seismometry”. In: *International Geophysics*. Vol. 81. Elsevier, 2002, pp. 283–304. ISBN: 0074-6142.

[92] Matthias Will et al. “Optical properties of waveguides fabricated in fused silica by femtosecond laser pulses”. In: *Applied Optics* 41.21 (2002), pp. 4360–4364.

[93] Amnon Yariv and Pochi Yeh. *Optical waves in crystals*. Vol. 5. Wiley New York, 1984.

[94] Mohamed Zanaty et al. “Programmable multistable mechanisms for safe surgical puncturing”. In: *Journal of Medical Devices* 13.2 (2019). ISSN: 1932-6181.

[95] Haibin Zhang et al. “Three-dimensional optical sensing network written in fused silica glass with femtosecond laser”. In: *Optics express* 16.18 (2008), pp. 14015–14023. ISSN: 1094-4087.

[96] Kaiming Zhou et al. “Line-by-line fiber Bragg grating made by femtosecond laser”. In: *IEEE Photonics Technology Letters* 22.16 (2010), pp. 1190–1192.

[97] Min-Kang Zhou et al. “Performance of a cold-atom gravimeter with an active vibration isolator”. In: *Physical Review A* 86.4 (Oct. 2012). DOI: 10.1103/physreva.86.043630.

[98] M. Zumberge et al. “An Optical Seismometer without Force Feedback”. In: *Bulletin of the Seismological Society of America* 100.2 (Mar. 2010), pp. 598–605. DOI: 10.1785/0120090136.

Common Flexure Material Properties

Table 1 shows the material properties found in the literature used in figure 1.1.

Table 1: Material properties for flexure mechanism manufacturing

Material	E [GPa]	σ_Y [GPa]	aspect ratio $\frac{L}{h}$	typical h_{min} [µm]
IP-L780	4.5	0.025	10	1
Glass	72	0.15	1000	20
Silicon	160	0.17	20	2
Steel	210	0.75	220	25
Titanium	100	0.7	220	25
Copper-Beryllium	130	0.7	1000	40
Invar	140	0.5	220	25

E-VINS - Assembly drawings

This appendix contains the assembly drawings of the vertical inertial sensor E-VINS mentioned in section 4.2.2.
the scales mentioned in these drawings are not correct. These drawings were converted to A4 pages for their inclusion in this document. As they are in a vector format, you can zoom in using the digital version of this document.
This appendix contains the following files:

- The E-VINS assembly;
- The E-VINS Bill of Materials;
- The oscillator stage assembly;
- The interferometer tilt stage assembly;
- The oscillator stage assembly;
- The inertial mass assembly;
- The corner cube assembly;
- The custom voice-coil actuator assembly;
- The mechanical footprint of the E-VINS.

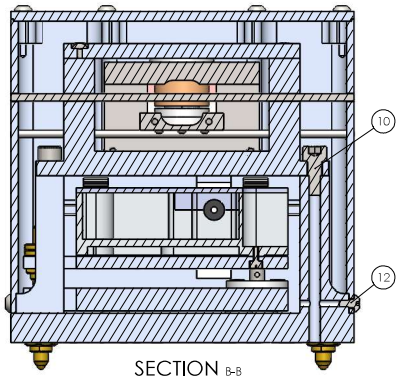

SECTION B-B

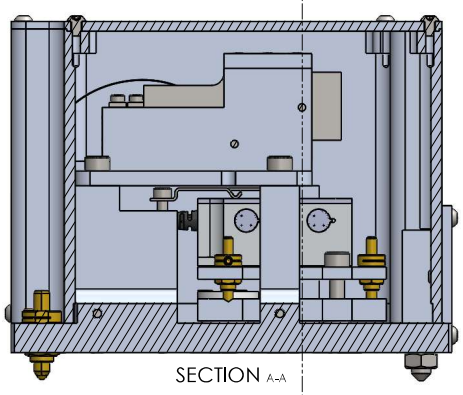

SECTION A-A

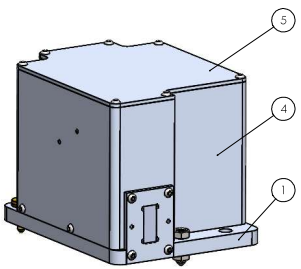

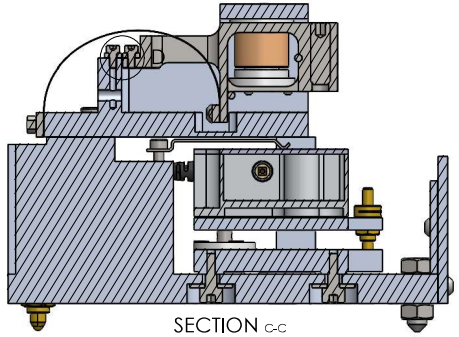

SECTION C-C

ITEM NO.	PART NUMBER	QTY.
1	2.1 Interferometer stage	1
2	2.2 Oscillator stage	1
3	2.3 VCA stage	1
4	2.4 Lid side	1
5	2.5 Lid cover	1
6	Newport-AJS100-0_5H-V6	2
7	2.6 Blocking rod	2
8	BN 115 1089064 hex nut M8.stp	2
9	BN 618 1237098 hexagon socket set screw M8x30.stp	1
10	BN 3 1004298 hex socket head cap screw M6x14.stp	4
11	BN 30102 3167670 hex socket button head screw M4x10.stp	3
12	BN 30102 3167668 hexagon socket button head screw M4x6.stp	14

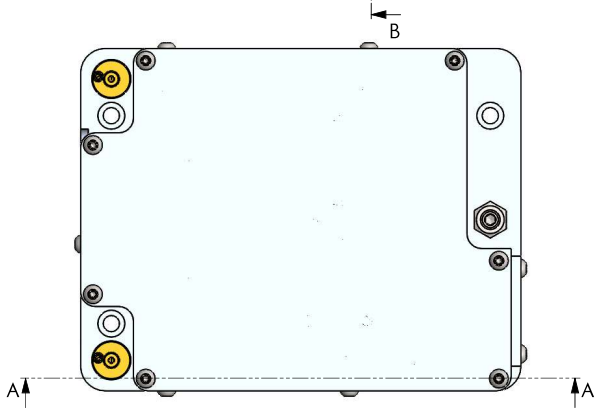

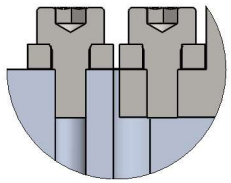

DETAIL D

SCALE 5 : 1

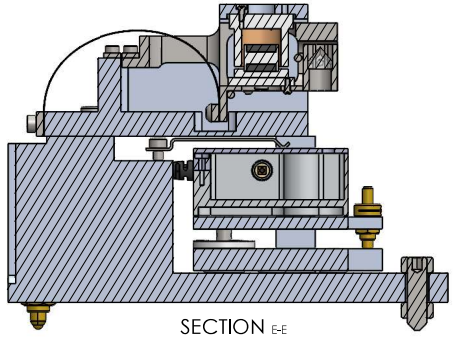

SECTION E-E

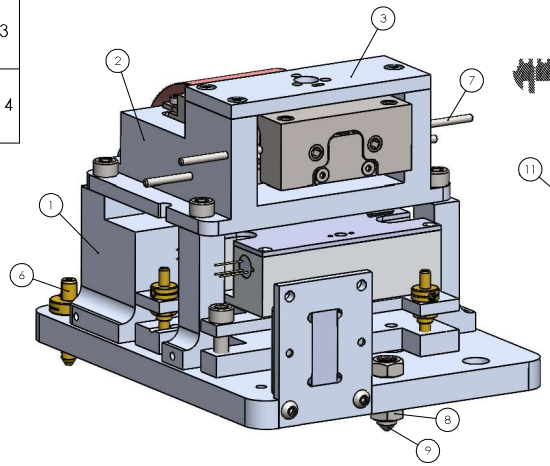

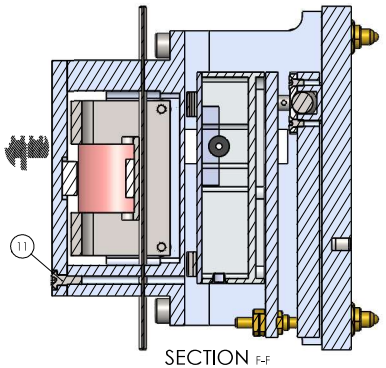

SECTION F-F

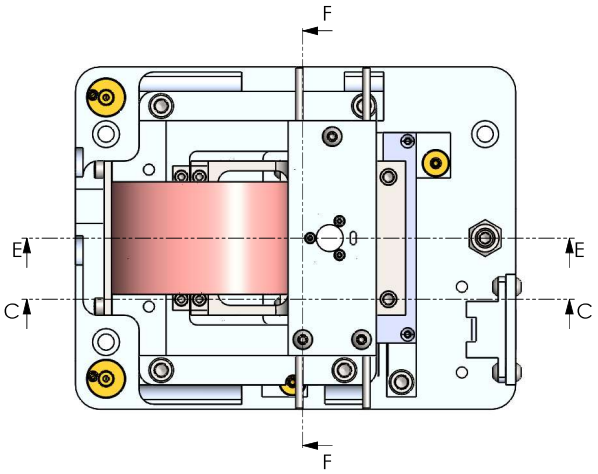

UNLESS OTHERWISE SPECIFIED: DIMENSIONS ARE IN MILLIMETERS SURFACE FINISH: TOLERANCES: LINEAR: ANGULAR:					DEBURR AND BREAK SHARP EDGES	DO NOT SCALE DRAWING	REVISION
	NAME	SIGNATURE	DATE			TITLE:	
DRAWN	L. Arnaud		06-Feb-23				
CHK'D							
APP'D							
MFG							
Q.A				MATERIAL		DWG NO.	A1
						2 E-VINS	
				WEIGHT:		SCALE:1:1	SHEET 1 OF 1

ITEM NO.	PART NUMBER	QTY.
1	2.1.1 Base mount	1
2	2.1.2.1 Connector clamp	1
3	2.1.2.2 Connector plate	1
4	BN 30102 3167668 hexagon socket button head screw M4x6.stp	18
5	DB9 Connector AME	1
6	2.1.3.1 Ball	1
7	2.1.3.2 Ball clamp	1
8	2.1.3.3 Bottom platform	1
9	2.1.3.4 Spacer	1
10	2.1.3.5 Top platform	1
11	AJS8-100-0.5H-V6	2
18	BN 3 1003755 hexagon socket head cap screw M3x6.stp	7
19	BN 3 1004301 hex socket head cap screw M6x16.stp	1
20	BN 616 1076450 hex socket flat countersunk head screw M3x6.stp	5
21	BN 3 1003771 hexagon socket head cap screw M3x10.stp	1
22	2.1.3.6 Short spring	1
23	2.1.3.7 Long spring	1
24	BN 3 1003917 hexagon socket head cap screw M4x10.stp	4
25	BN 1356 1117157 flat washer M6.stp	4
26	BN 3 1004298 hex socket head cap screw M6x14.stp	8
27	BN 30102 3167670 hex socket button head screw M4x10.stp	5
28	2.2.1.1 Inertial mass	1
29	S-12-03-N.stp	2
30	2.2.1.2.2 Vertical support	1
31	2.2.1.2.3 Adapter plate	1

32	BN 272 1000004 hexagon socket head cap screw M3x4.stp	2
33	2.2.1.2.1 Magnet holder	1
34	BN 19 1805576 hexagon socket button head screw M2x5.stp	6
35	2.2.1.3 Suspension clamp	1
36	BN 1424 1204807 hexagon socket set screw M8x25.stp	2
37	2.2.1.4.1 Corner Cube mount	1
38	PS974_withAFlatSide.step	1
39	BN 28 1034286 hexagon socket set screw M3x3.stp	1
40	BN 621 1115324 hexagon socket set screw M8x12.stp	2
41	2.2.2 Inertial Mass Base mount	1
42	2.2.3 Fixed Suspension clamp	1
43	2.2.5 Leafspring hinge	1
44	2.2.4 Leafspring clamp	2
45	2.2.6 Suspension blade	1
46	2.3.1 Coil mount	1
47	2.3.2 Coil	1
48	2.4 Lid side	1
49	2.5 Lid cover	1
50	Newport-AJS100-0_5H-V6	2
51	2.6 Blocking rod	2
52	BN 115 1089064 hex nut M8.stp	2
53	BN 618 1237098 hexagon socket set screw M8x30.stp	1

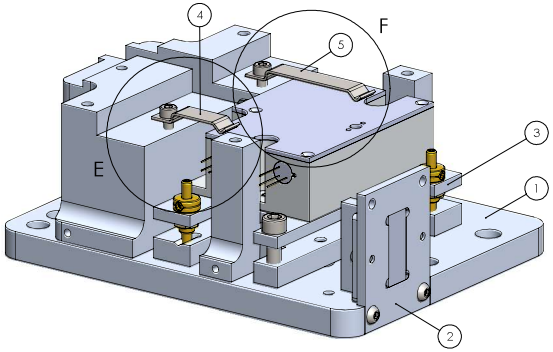

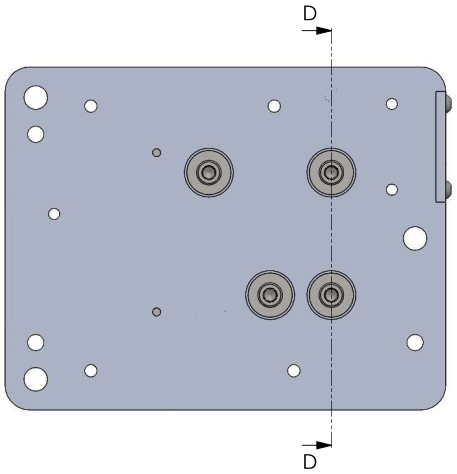

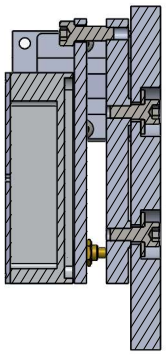

SECTION D-D

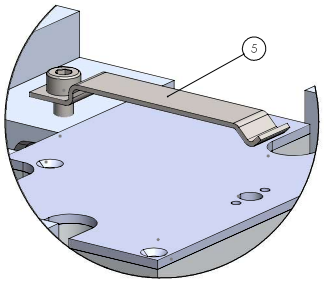

DETAIL F
SCALE 2 : 1

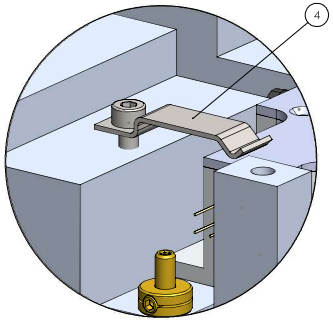

DETAIL E
SCALE 2 : 1

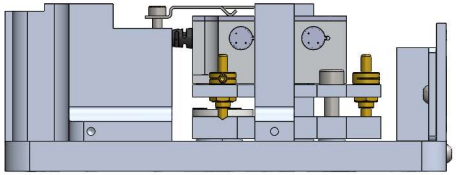

ITEM NO.	PART NUMBER	QTY.
1	2.1.1 Base mount	1
2	2.1.2 DB9 Connector stage	1
3	2.1.3 Tilt stage	1
4	2.1.3.6 Short spring	1
5	2.1.3.7 Long spring	1
6	BN 3 1003917 hexagon socket head cap screw M4x10.stp	2
7	BN 1356 1117157 flat washer M6.stp	4
8	BN 3 1004298 hex socket head cap screw M6x14.stp	4
9	BN 30102 3167670 hex socket button head screw M4x10.stp	2

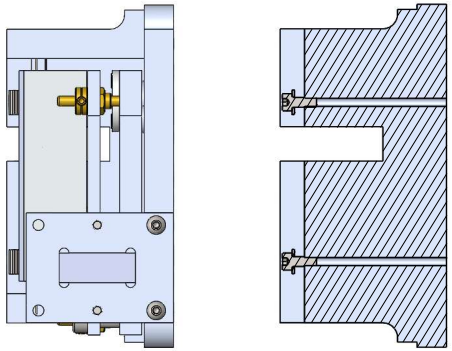

SECTION C-C

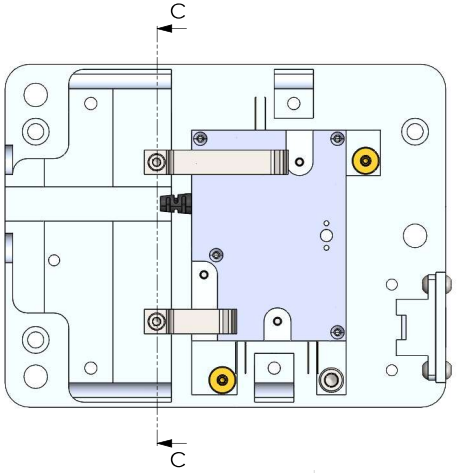

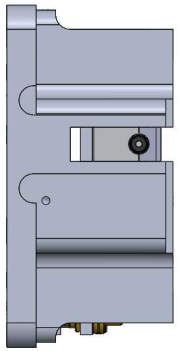

UNLESS OTHERWISE SPECIFIED: DIMENSIONS ARE IN MILLIMETERS SURFACE FINISH: TOLERANCES: LINEAR: ANGULAR:				DEBURR AND BREAK SHARP EDGES	DO NOT SCALE DRAWING	REVISION
	NAME	SIGNATURE	DATE		TITLE:	
DRAWN	L. Anne-Dee		04-04-23			
CHK'D						
APP'D						
MFG						
Q.A				MATERIAL	DWG NO. 2.1 Interferometer stage	A1
				WEIGHT:	SCALE:1:1	SHEET 1 OF 1

ITEM NO.	PART NUMBER	QTY.
1	2.1.3.1 Ball	1
2	2.1.3.2 Ball clamp	1
3	2.1.3.3 Bottom platform	1
4	2.1.3.4 Spacer	1
5	2.1.3.5 Top platform	1
6	AJS8-100-0.5H-V6	2
7	Interferometer_A220006A	1
8	BN 3 1003755 hexagon socket head cap screw M3x6.stp	3
9	BN 3 1004301 hex socket head cap screw M6x16.stp	1
10	BN 616 1076450 hex socket flat countersunk head screw M3x6.stp	3
11	BN 3 1003771 hexagon socket head cap screw M3x10.stp	1

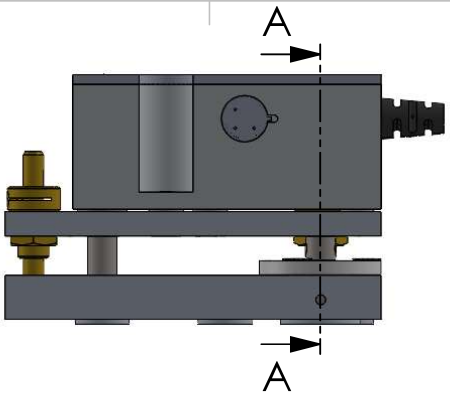

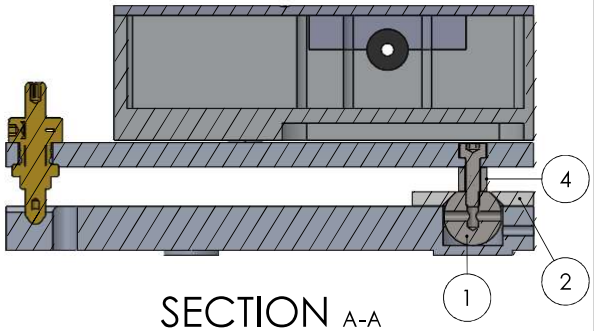

SECTION A-A

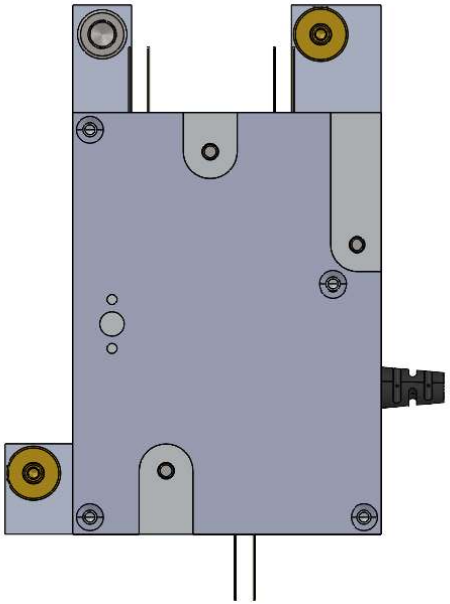

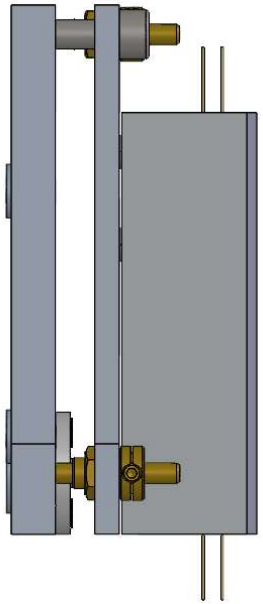

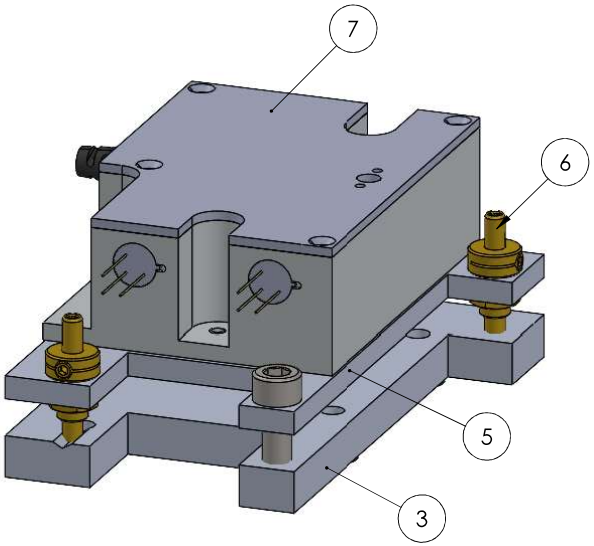

UNLESS OTHERWISE SPECIFIED: DIMENSIONS ARE IN MILLIMETERS SURFACE FINISH: TOLERANCES: LINEAR: ANGULAR:		FINISH:		DEBURR AND BREAK SHARP EDGES	DO NOT SCALE DRAWING	REVISION
	NAME	SIGNATURE	DATE		TITLE:	
DRAWN	L. Amez-Droz		06-04-23			
CHK'D						
APPV'D						
MFG						
Q.A				MATERIAL:	DWG NO. 2.1.3 Tilt stage	A3
				WEIGHT:	SCALE:1:1	SHEET 1 OF 1

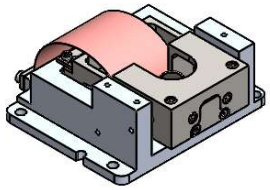

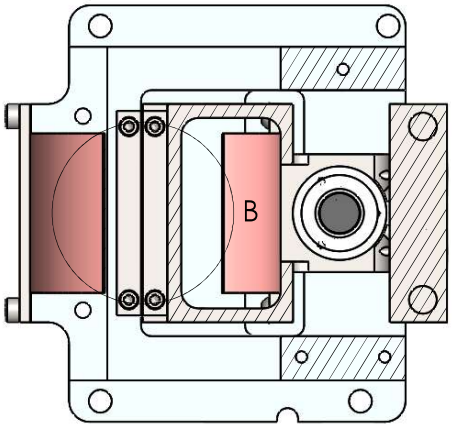

SECTION A-A

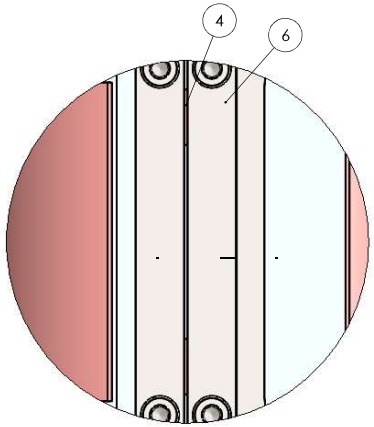

DETAIL B

SCALE 2 : 1

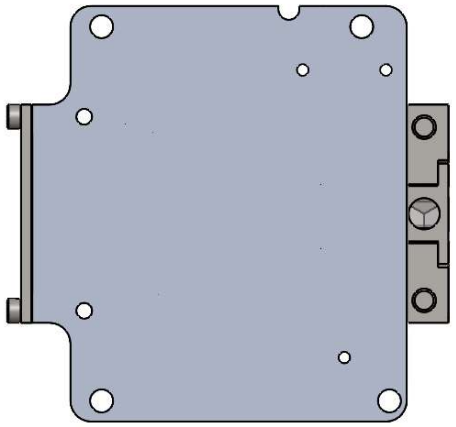

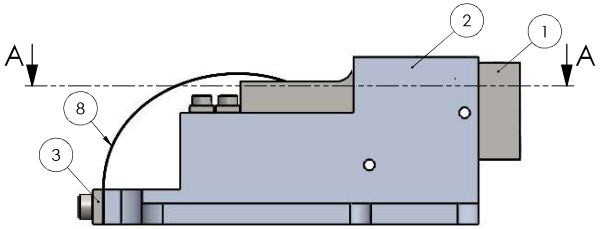

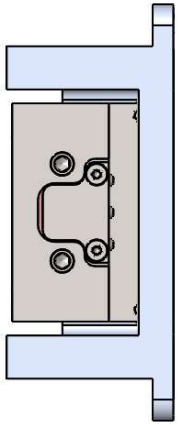

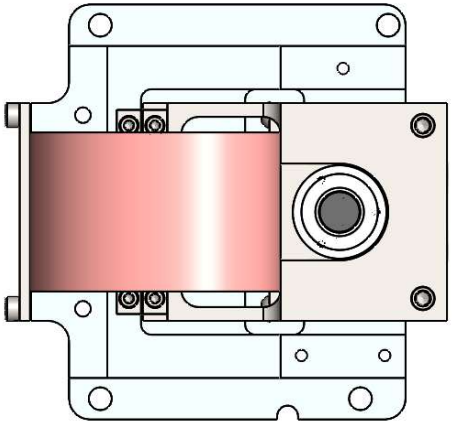

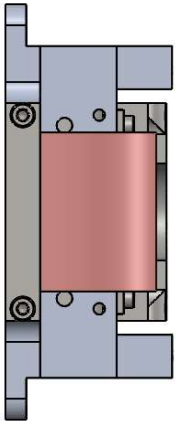

ITEM NO.	PART NUMBER	QTY.
1	2.2.1 Inertial Mass assembly	1
2	2.2.2 Inertial Mass Base mount	1
3	2.2.3 Fixed Suspension clamp	1
4	2.2.5 Leafspring hinge	1
5	BN 3 1003917 hexagon socket head cap screw M4x10.stp	2
6	2.2.4 Leafspring clamp	2
7	BN 3 1003755 hexagon socket head cap screw M3x6.stp	4
8	2.2.6 Suspension blade	1

UNLESS OTHERWISE SPECIFIED: DIMENSIONS ARE IN MILLIMETERS SURFACE FINISH: TOLERANCES: LINEAR: ANGULAR:		FINISH:		DEBURR AND BREAK SHARP EDGES	DO NOT SCALE DRAWING
	NAME	SIGNATURE	DATE		TITLE:
DRAWN	L. Ames-Diroz		06-04-23		
CHK'D					
APPV'D					
MFG					
Q.A				MATERIAL:	DWG NO. 2.2 Oscillator stage
				WEIGHT:	SCALE:1:1

A2

SHEET 1 OF 1

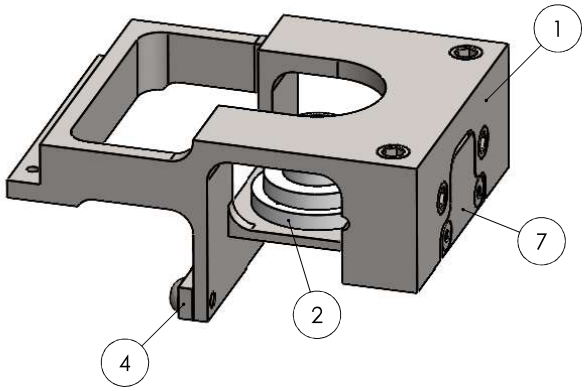

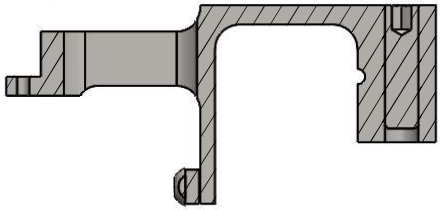

SECTION C-C

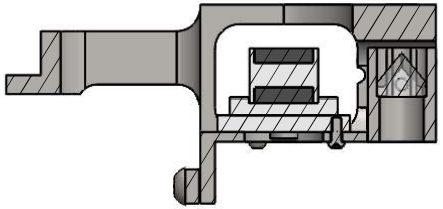

SECTION A-A

ITEM NO.	PART NUMBER	QTY.
1	2.2.1.1 Inertial mass	1
2	2.2.1.2 VCA magnet	1
3	BN 19 1805576 hexagon socket button head screw M2x5.stp	3
4	2.2.1.3 Suspension clamp	1
5	BN 30102 3167668 hexagon socket button head screw M4x6.stp	2
6	BN 1424 1204807 hexagon socket set screw M8x25.stp	2
7	2.2.1.4 Reflector	1
8	BN 616 1076450 hex socket flat countersunk head screw M3x6.stp	2
9	BN 621 1115324 hexagon socket set screw M8x12.stp	2

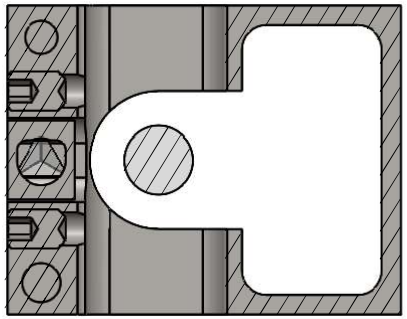

SECTION B-B

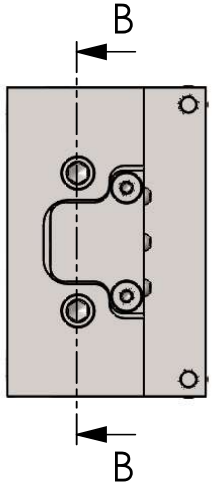

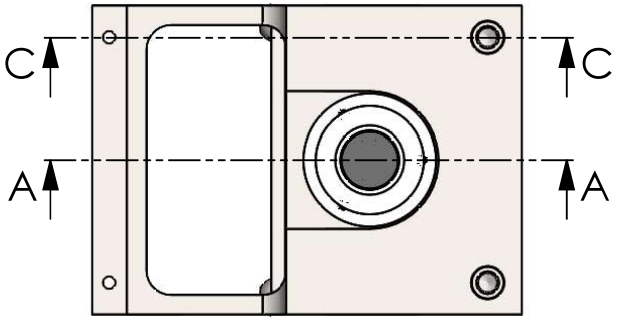

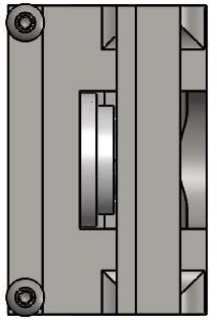

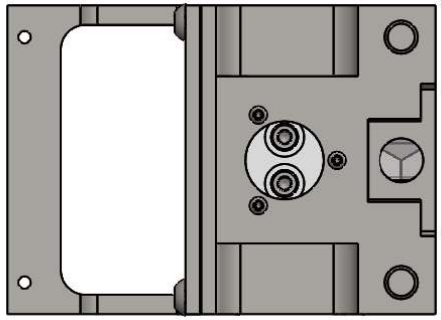

UNLESS OTHERWISE SPECIFIED: DIMENSIONS ARE IN MILLIMETERS SURFACE FINISH: TOLERANCES: LINEAR: ANGULAR:		FINISH:			DEBURR AND BREAK SHARP EDGES	DO NOT SCALE DRAWING	REVISION
	NAME	SIGNATURE	DATE			TITLE:	
DRAWN	L. Amez-Droz		06-04-23				
CHK'D							
APPV'D							
MFG							
Q.A				MATERIAL:		DWG NO. 2.2.1 Inertial Mass assembly	A3
				WEIGHT:		SCALE:1:1	SHEET 1 OF 1

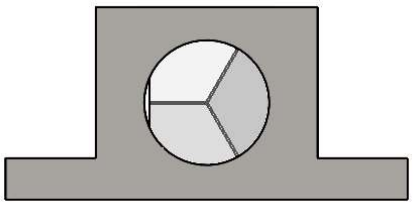

ITEM NO.	PART NUMBER	QTY.
1	2.2.1.4.1 Corner Cube mount	1
2	PS974_withAFlatSide.step	1
3	BN 28 1034286 hexagon socket set screw M3x3.stp	1

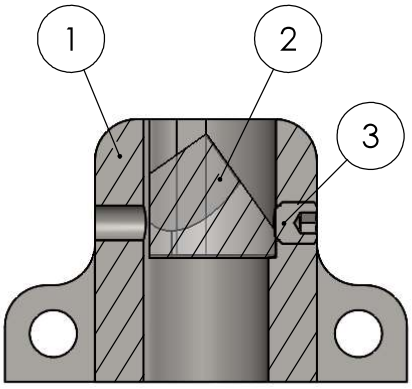

SECTION A-A

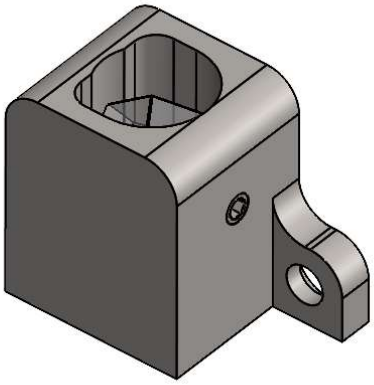

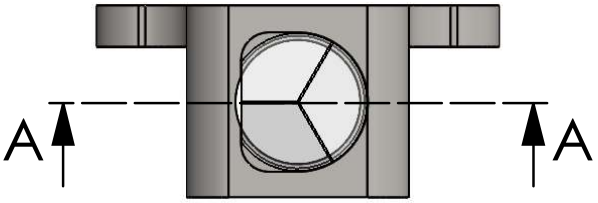

UNLESS OTHERWISE SPECIFIED: DIMENSIONS ARE IN MILLIMETERS SURFACE FINISH: TOLERANCES: LINEAR: ANGULAR:		FINISH:		DEBURR AND BREAK SHARP EDGES		DO NOT SCALE DRAWING	REVISION
	NAME	SIGNATURE	DATE			TITLE:	
DRAWN	L. Amez-Droz		06-04-23				
CHK'D							
APPV'D							
MFG							
Q.A				MATERIAL:		DWG NO. 2.2.1.4 Reflector	A4
				WEIGHT:		SCALE:2:1	SHEET 1 OF 1

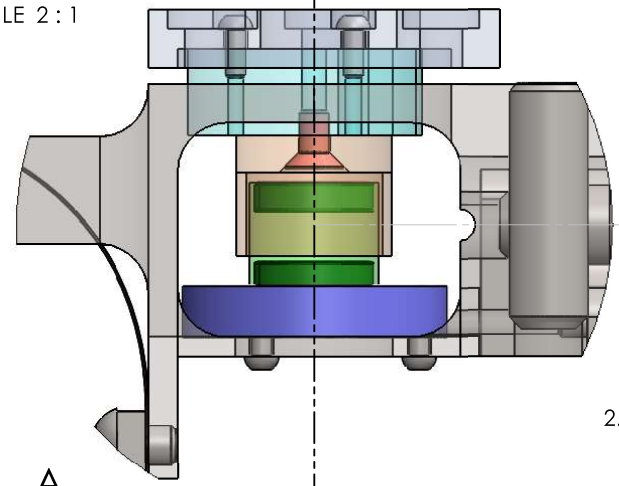

DETAIL A
SCALE 2 : 1

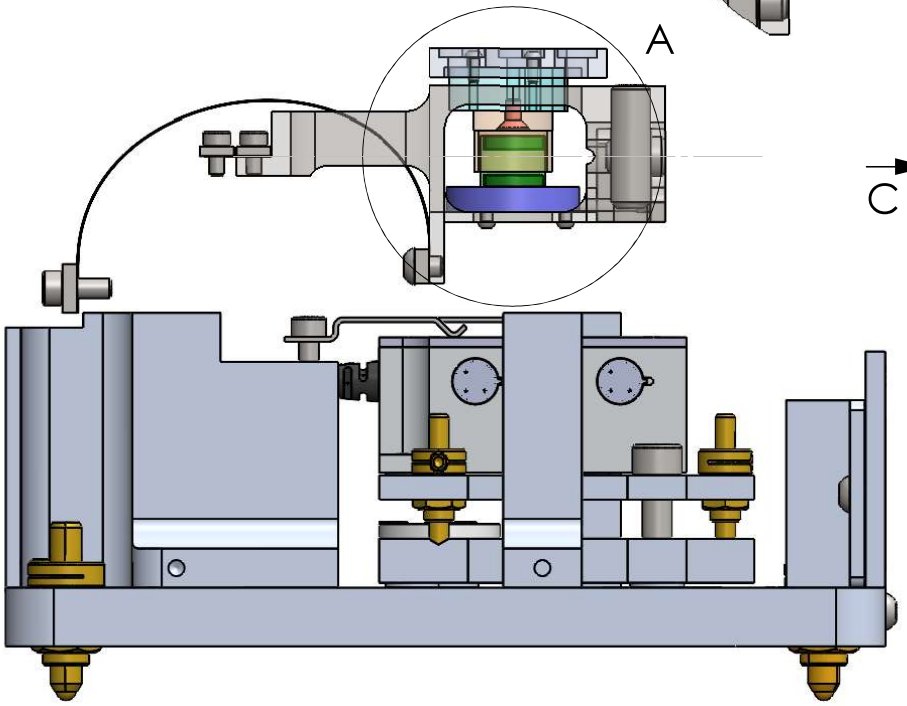

SECTION C-C
SCALE 2 : 1

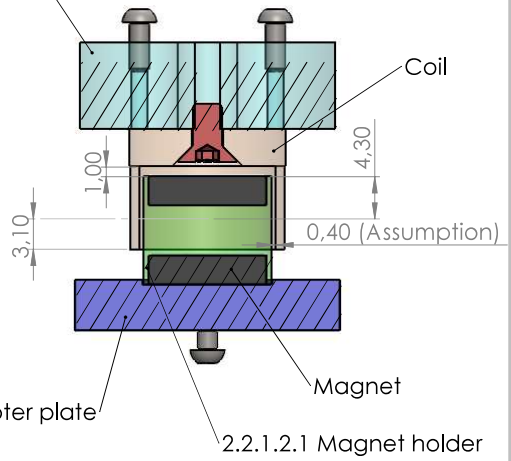

UNLESS OTHERWISE SPECIFIED: DIMENSIONS ARE IN MILLIMETERS SURFACE FINISH: TOLERANCES: LINEAR: ANGULAR:		FINISH:		DEBURR AND BREAK SHARP EDGES	DO NOT SCALE DRAWING / REVISION
	NAME	SIGNATURE	DATE		TITLE: E-VINS part of ETEST project
DRAWN	L. Amez-Droz		03-07-23		
CHK'D					
APPV'D					
MFG					
Q.A				MATERIAL:	DWG NO. 2 E-VINS Voice Coil Actuator assembly — A3
				WEIGHT:	SCALE:1:1 — SHEET 1 OF 1

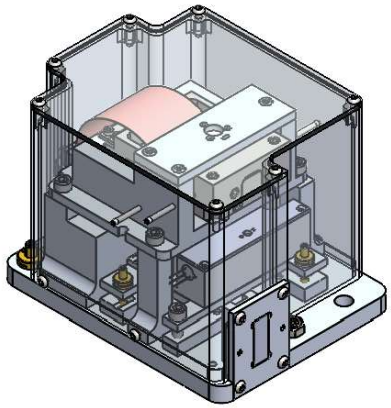

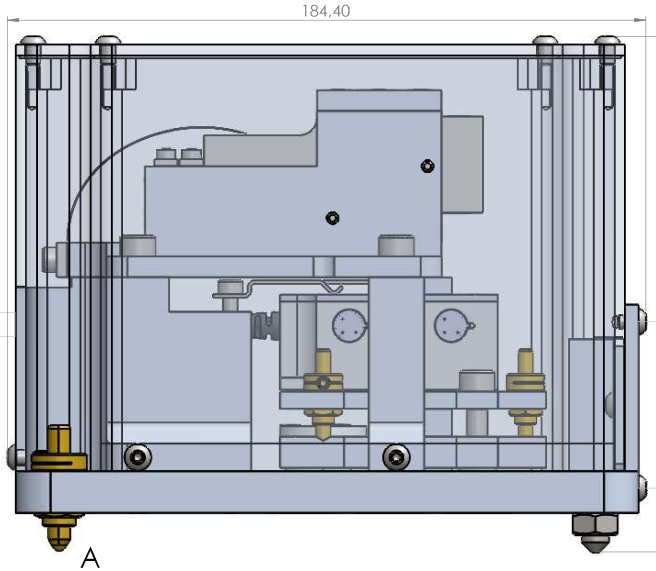

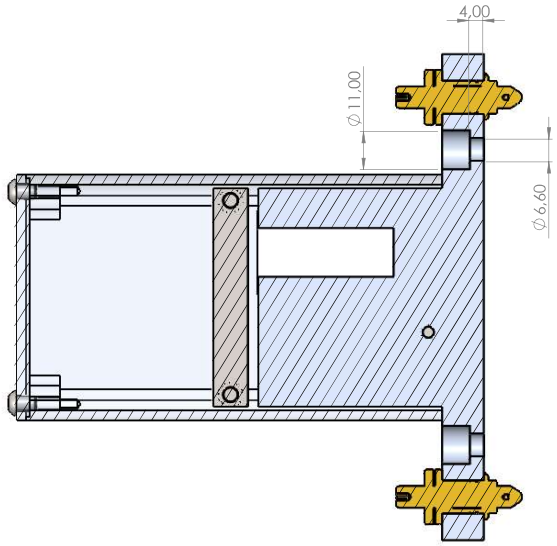

SECTION A-A
SCALE 1 : 1

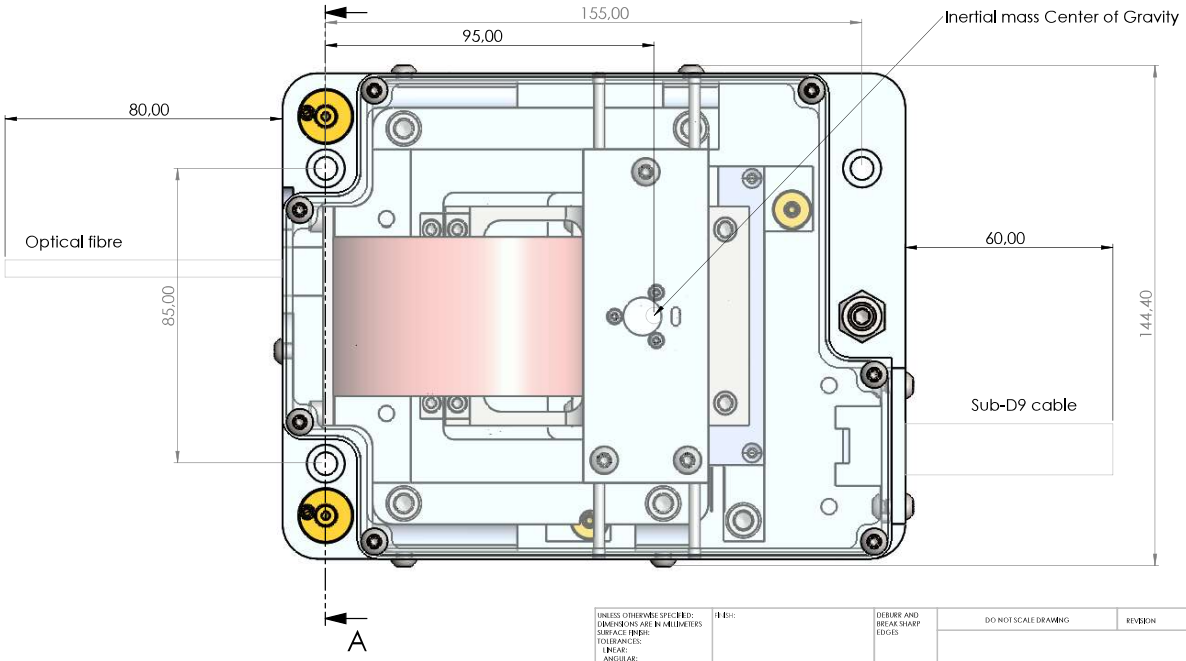

UNLESS OTHERWISE SPECIFIED: DIMENSIONS ARE IN MILLIMETERS SURFACE FINISH: TOLERANCES: LINEAR: ANGULAR:	FINISH:		DEBURR AND BREAK SHARP EDGES	DO NOT SCALE DRAWING	REVISION
	NAME	SIGNATURE	DATE	TITLE:	
DRAWN					
CHK'D					
APPV'D					
MFG					
Q.A					
				MATERIAL:	DWG NO. A2
				WEIGHT:	SCALE:1:2 SHEET 1 OF 1

2 E-VINS - mechanical footpri